

9 2 0 9 0 8 0 6 2

NRL Memorandum Report 4019

12

A072359

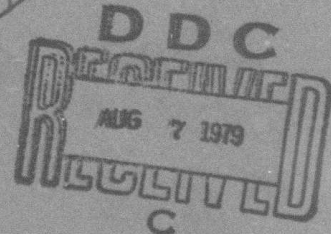
**DARPA-NRL Laser Program
Annual Technical Report to
Defense Advanced Research Projects Agency
1 October 1977 - 30 September 1978**

*Laser Physics Branch
Optical Sciences Division*

LEVEL III

A055912

June 28, 1979



DDC FILE COPY



NAVAL RESEARCH LABORATORY
Washington, D.C.

Approved for public release; distribution unlimited.

79 08 06 02 6

SECURITY CLASSIFICATION OF THIS PAGE (When Data Entered)

REPORT DOCUMENTATION PAGE		READ INSTRUCTIONS BEFORE COMPLETING FORM	
1. REPORT NUMBER NRL Memorandum Report 4019	2. GOVT ACCESSION NO. (9)	3. RECIPIENT'S CATALOG NUMBER Rept. for	
4. TITLE (and Subtitle) DARPA-NRL LASER PROGRAM - ANNUAL TECHNICAL REPORT TO DEFENSE ADVANCED RESEARCH PROJECTS AGENCY - 1 OCTOBER 1977 - 30 SEPTEMBER 1978,	5. TYPE OF REPORT & PLATON COVERED Annual technical report / FY 78		
7. AUTHOR(s) Laser Physics Branch (S.K. Searles) coordinator) Optical Sciences Division		8. CONTRACT OR GRANT NUMBER(s)	
9. PERFORMING ORGANIZATION NAME AND ADDRESS Naval Research Laboratory Washington, D.C. 20375		10. PROGRAM ELEMENT, PROJECT, TASK AREA & WORK UNIT NUMBERS NRL Problem K03-53 DARPA Order-2062; Project 7E20	
11. CONTROLLING OFFICE NAME AND ADDRESS Defense Advanced Research Projects Agency Arlington, VA 22209		12. REPORT DATE June 28, 1979	
14. MONITORING AGENCY NAME & ADDRESS (if different from Controlling Office) (13) 170p.		13. NUMBER OF PAGES 168	
		15. SECURITY CLASS. (of this report) UNCLASSIFIED	
		15a. DECLASSIFICATION/DOWNGRADING SCHEDULE	
16. DISTRIBUTION STATEMENT (of this Report) Approved for public release; distribution unlimited.			
17. DISTRIBUTION STATEMENT (of the abstract entered in Block 20, if different from Report)			
18. SUPPLEMENTARY NOTES			
19. KEY WORDS (Continue on reverse side if necessary and identify by block number) Lasers Electrical lasers Laser diagnostics Electronic state lasers Chemical kinetics Electronic state lifetimes Energy transfer Chemiluminescence			
20. ABSTRACT (Continue on reverse side if necessary and identify by block number) The DARPA-NRL Program is concerned with the development of laser technology. New concepts in photolytic pumping and wavelength conversion have been investigated. Limitations of the mercury halide lasers have been studied. The basic physics of the XeF laser has been examined theoretically and experimentally.			

DD FORM 1 JAN 73 1473

EDITION OF 1 NOV 65 IS OBSOLETE
S/N 0102-014-6601

i

SECURITY CLASSIFICATION OF THIS PAGE (When Data Entered)

251 950

1/3

CONTENTS

FOREWORD	iv
SHORT PULSE KINETICS EXPERIMENTS	1
LONG PULSE KINETICS EXPERIMENTS	43
COMPUTER CODE DEVELOPMENT AND APPLICATIONS	57
ELECTRON BEAM CONTROLLED XeF LASER	107
ABSORPTION EXPERIMENTS RELEVANT TO THE XeF (B-X) LASER	115
E-BEAM SUSTAINED MERCURY HALIDE LASERS	123
PHOTOLYTIC PUMPING OF RARE GAS AND MERCURY HALIDE LASERS	131
THE POSSIBILITY OF A RgOH* LASER	153
WAVELENGTH CONVERSION STUDIES	164

Accession For	
NTIS GRA&I	<input checked="checked" type="checkbox"/>
DDC TAB	<input type="checkbox"/>
Unannounced	<input type="checkbox"/>
Justification	
By _____	
Distribution/	
Availability Codes	
Dist	Avail and/or special
A	

FOREWORD

The Laser Physics Branch of the Optical Sciences Division, Naval Research Laboratory, Washington, D. C., prepared this annual report on work sponsored by the Defense Advanced Research Projects Agency, DARPA Order 2062. The projects described are also funded by NRL-ONR research funds. Co-authors of the report were R. Burnham, L. Champagne, N. Djeu, J. G. Eden, R. Waynant, S. K. Searles, L. Palumbo, W. Whitney, R. Chang, T. Finn and W. S. Watt.

FY 78 ANNUAL TECHNICAL REPORT

1. DARPA Order	2062
2. Program Code Number	7E20
3. Name of Contractor	Naval Research Laboratory
4. Effective Date of Contract	1 July 1972
5. Contract Expiration Date	30 September 1980
6. Amount of Contract	\$390,000
7. Contract Number	62301E
8. Principal Investigator	W. S. Watt
9. Telephone Number	(202) 767-3217
10. Project Scientist	S. K. Searles
11. Telephone Number	(202) 767-2255
12. Title of Work	DARPA/NRL Laser Technology Program

SPONSORED BY
DEFENSE ADVANCED RESEARCH PROJECTS AGENCY
DARPA Order No. 2062

SHORT PULSE KINETICS EXPERIMENTS

1. KrF* and HgX* (X = Br, I) Kinetics

Initial fast-photolysis kinetics experiments were reported in April. These experiments covered the measurement of the XeF* (B-X) lifetime and quenching rate constants for the important constituents of XeF laser gas mixtures. Also, lifetime measurements of KrF* (B-X) were reported along with the quenching rate constant for Xe. This report concludes the KrF* quenching, describes measurements of lifetimes and quenching rate constants for the mercury halides (HgBr and HgI), and reports the lifetime of the XeF (C-A) transition.

2. KrF* (B-X) Quenching

The experimental system used to measure the quenching rate constants was shown in the previous report. The technique utilized a 2ns pulse of 600 keV electrons from a Febetron 706 to excite an Ar/F₂ mixture and produce a short burst of ArF* radiation at 193 nm. This 193 nm pulse entered a quartz cell containing KrF₂ vapor and photolyzed the KrF₂ producing KrF*(B) + F. The KrF*(B) decay is monitored with a fast photodiode and found to decay with a single exponential lifetime of 6.8 ns. Since the vapor pressure of KrF₂ is kept low and since only a small amount of KrF₂ is photodissociated, quenching by the dissociation products or the parent molecule can be kept to a negligible level.

The rate constants are obtained by using a least squares fit to the

Note: Manuscript submitted April 5, 1979.

measured rate versus quenching gas density data.

Table I presents the measured rate constants for KrF*. All of the gases used for these quenching studies play an important role in either electron-beam-pumped or discharge-pumped KrF lasers. The interpretation of these rate constants are discussed more fully in the accompanying manuscripts published in Applied Physics Letters and the Journal of Applied Physics.

3. HgX* Lifetime and Quenching (X = Br, I)

Because of the recent success in obtaining lasing from the mercury halide molecules, it was deemed important to investigate the kinetics of these molecules. All of the mercury dihalide molecules are stable and commercially available. Reasonable vapor pressures are obtained by raising the dihalide temperature to the 90 - 150°C range. To measure the lifetime of these molecules the experiment was modified to the configuration shown in Fig. 1. The photolyzing light pulse is generated in a coaxial diode where the gas mixture is contained within a thin aluminum cylinder and radially excited by the fast Febetron pulse of electrons. Gas mixtures of Ne:Ar:F₂ (2000:400:100 torr) were used to produce ArF radiation (193 nm) for photodissociation of HgBr₂ and Ar:Kr:Cl₂ (2000:200:10 torr) mixtures were used to produce KrCl radiation (222 nm) for photodissociation of HgI₂. With both mixtures the pulse width was ~ 2.5 ns FWHM. The pulses were directed into a Suprasil tube filled with a small amount of HgX₂ and enclosed in an oven. Photodissociation of the HgX₂ produced HgX*(B) + X. The fluorescence from HgX (B-X) decay passed through a narrowband filter and was

monitored by a fast response photomultiplier coupled to a digitizer. These signals were plotted on a semilog scale and were found to fit a single exponential decay line. By varying the HgX_2 pressure via oven temperature, HgX lifetimes and the quenching of $\text{HgX}^*(\text{B})$ by HgX_2 were determined. These lifetimes and rates are given in Table II. Table II gives values of lifetime of HgCl and quenching of HgCl by HgCl_2 which were performed in an analogous manner on another electron beam machine having a somewhat longer pulsewidth. Lifetimes and quenching of HgCl have not yet been done with the fast Febetron system since the wavelength needed to photolyze HgCl_2 will not propagate through air.

Quenching rate constants for a number of important laser gas constituents were measured by fixing the HgX_2 pressure and adding a wide range of quenching gas pressures. From a least squares fit to the decay rate versus pressure data, two body quenching rate constants have been determined for HgBr^* and HgI^* . These rate constants are given in Tables III and IV. Of particular concern is the rather large rate constant determined for quenching of $\text{HgBr}(\text{B})$ by Hg ($1.3 \times 10^{-10} \text{ cm}^3 \text{ sec}^{-1}$). Since Hg is a constituent for laser gas mixtures, considerable quenching losses can result. Further discussions of the mercury halide kinetics is contained in the reprint from Applied Physics Letters and in the manuscript submitted to Applied Physics Letters which follow.

4. Lifetime of the C-A Band of XeF

Considerable interest in the C-A transition in XeF has developed recently because of both the possibility that gain might be produced on the transition and the interest that the C level might play in the

kinetics of the B-X laser transition. Fig. 2 shows the potential energy diagram¹ of XeF and the close proximity of the B and C levels. This close proximity raises the possibility of energy transfer from C to B at elevated temperatures. Modeling of such possibilities requires accurate knowledge of the C state lifetime.

To measure the C state lifetime a somewhat different experimental approach was taken than the previous fast photolysis which yielded too few C state molecules. In this case XeF₂ vapor was placed in the cylindrical center tube of the coaxial diode and dissociated by electron impact. By using a 460 nm filter ($T_{\text{max}} = 35\%$ at $\lambda_0 = 462$ nm; $\Delta\lambda = 50$ nm) to pass only the C-A emission, the fluorescence was detected, displayed on an oscilloscope, recorded, digitized and plotted on a semilog plot from which a decay time was determined. By monitoring the change in decay time as XeF₂ pressure was varied from 0.1 - 0.5 Torr, both a measure of the C-A lifetime, 93 ± 5 ns, and the quenching rate constant for XeF (C) due to XeF₂, $(1.8 \pm 0.5) \cdot 10^{-10}$ cm³-sec⁻¹, were determined. Using this measured lifetime it was possible to correct Kligler's² estimated B-C energy defect. The B-C separation is now estimated to be 610 ± 60 cm⁻¹ or .076 eV which agrees with the separation of 0.08 eV measured by Brashears and Setser³. Further details can be found in the manuscript to be published in the Journal of Quantum Electronics which follows.

In summary, fast pulse dissociation of the dihalide molecules to nearly instantaneously produce the excited state halide laser molecule provides a clear measurement of excited state lifetimes and collisional quenching rate constants. These measured numbers should allow

realistic modeling of the rare gas and mercury halide lasers.

References

1. T. H. Dunning, Jr. and P. J. Hay, J. Chem. Phys. 69, 134 (1978).
2. D. Kligler, H. H. Nakano, D. L. Huestis, W. K. Bischel, R. M. Hill and C. K. Rhodes, Appl. Phys. Lett. 33, 39 (1978).
3. H. C. Brashears and D. W. Setser, Appl. Phys. Lett. 33, 821 (1978).

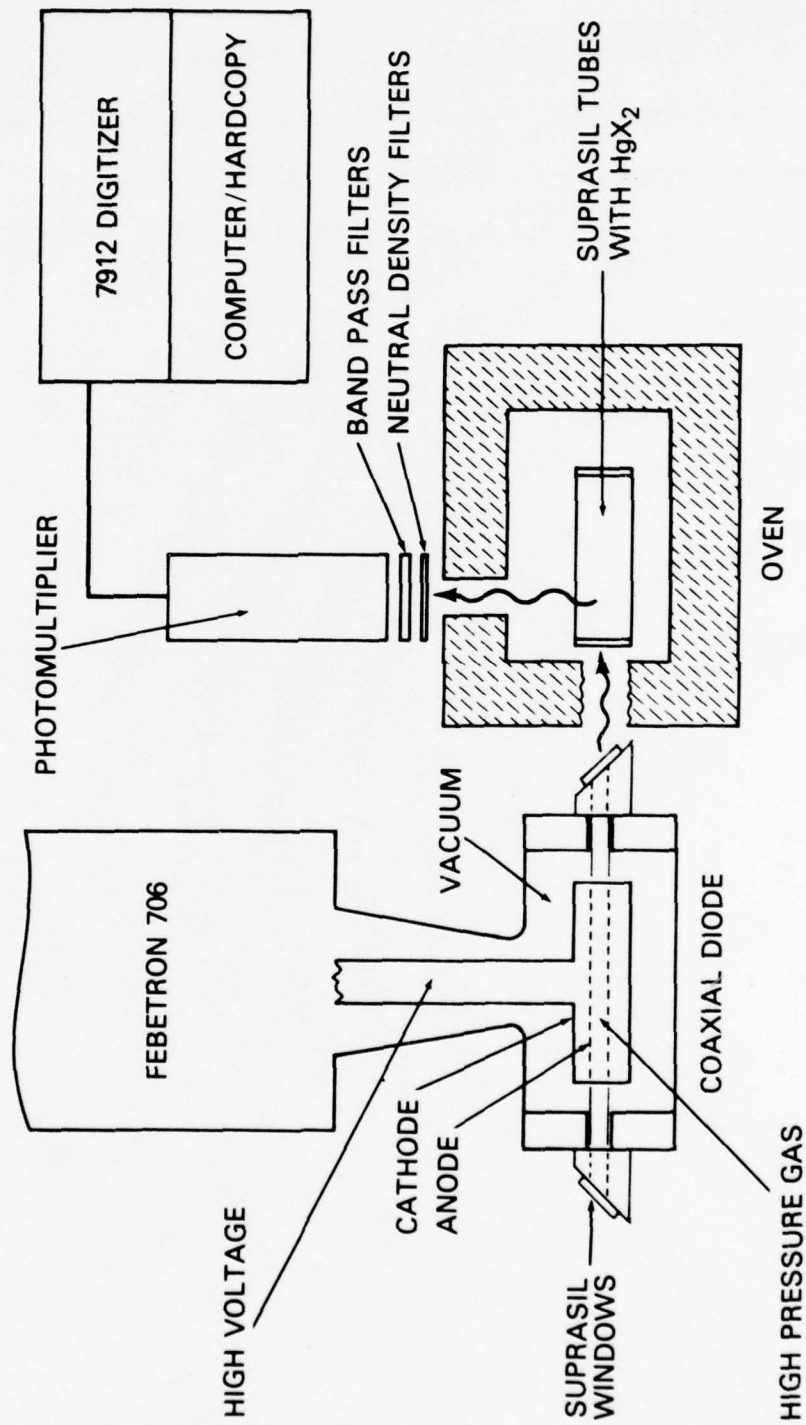


Fig. 1. Apparatus for fast photolysis kinetics experiments.

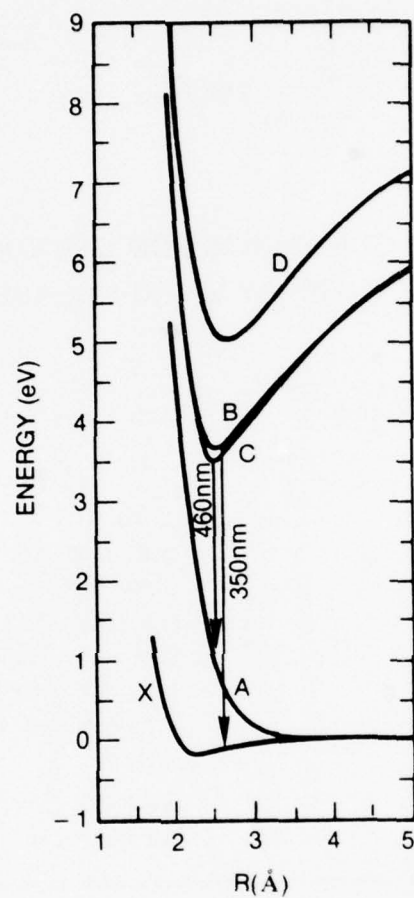


Fig. 2. Potential energy levels of XeF (after Dunning and Hay - ref 1)

TABLE I.

RATE CONSTANTS FOR QUENCHING
OF KrF(B) BY VARIOUS GASES

Quencher	Rate Constant ^a
He	$(3.3 \pm 1.1) \times 10^{-13}$
2He	$\leq 10^{-33}$ b
Ne	$(1.6 \pm 0.4) \times 10^{-12}$
2Ne	$< 10^{-32}$ b
Ar	$(1.8 \pm 0.6) \times 10^{-12}$
2Ar	$(1.1 \pm 0.4) \times 10^{-31}$ b
Kr	$(8.6 \pm 0.7) \times 10^{-12}$
2Kr	$9.7 \pm 0.8) \times 10^{-31}$ b
Xe	$> 10^{-9}$
F ₂	$(4.8 \pm 0.3) \times 10^{-10}$
NF ₃	$(5.2 \pm 0.5) \times 10^{-11}$

^a Units = cm³sec⁻¹.^b Units = cm⁶sec⁻¹.

TABLE II.

Radiative lifetimes and di-halide
quenching rate constants for the
mercury halide (B→X) transitions.

MOLECULE	$\tau_R(\text{NS})$	$K_Q(\text{CM}^3\text{-SEC}^{-1})$
HgCl(B)	22.2 ± 1.5	$9.2 \cdot 10^{11}$
HgBr(B)	23.7 ± 1.5	$1.7 \cdot 10^{10}$
HgI(B)	27.3 ± 2.0	$3.6 \cdot 10^{10}$

TABLE III.

HgBr(B) QUENCHING RATE CONSTANTS

QUENCHER	RATE CONSTANT (CM ³ -SEC ⁻¹)
He	$(5.2 \pm 2.0) \cdot 10^{-13}$
Ne	$(5.3 \pm 1.8) \cdot 10^{-13}$
Ar	$(7.4 \pm 1.5) \cdot 10^{-13}$
Xe	$(3.7 \pm 0.3) \cdot 10^{-12}$
Hg	$(1.3 \pm 0.8) \cdot 10^{-10}$
N ₂	$(4.4 \pm 0.5) \cdot 10^{-12}$
Br ₂	$(5.5 \pm 0.3) \cdot 10^{-10}$
HBr	$(2.0 \pm 0.4) \cdot 10^{-10}$
CH ₃ Br	$(3.9 \pm 0.4) \cdot 10^{-10}$
CCl ₂ Br ₂	$(4.3 \pm 0.4) \cdot 10^{-10}$

TABLE IV.

HgI(B) QUENCHING RATE CONSTANTS

QUENCHER	RATE CONSTANTS (CM ² -SEC ⁻¹)
Ar	$(3.3 \pm 1.5) \cdot 10^{-13}$
Xe	$(7.1 \pm 0.8) \cdot 10^{-13}$
Hg	$< 3 \cdot 10^{-11}$
N ₂	$(1.1 \pm 0.2) \cdot 10^{-12}$
HI	$(1.0 \pm 0.2) \cdot 10^{-10}$
CF ₃ I	$(2.9 \pm 0.3) \cdot 10^{-10}$

New quenching rates applicable to the KrF laser^{a)}

J. G. Eden, R. W. Waynant, S. K. Searles, and R. Burnham

Laser Physics Branch, Optical Sciences Division, Naval Research Laboratory, Washington, D.C. 20375
(Received 30 January 1978, accepted for publication 23 March 1978)

Photolysis of KrF_2 has been used to measure the rates of collisional quenching of $\text{KrF}(B)$ excimers in two- and three-body collisions with Ar, Kr, and F_2 . In addition, the $\text{KrF}(B \rightarrow X)$ band radiative lifetime was determined to be 6.8 ± 0.2 ns. The results are in good agreement with existing theory and demonstrate the importance of quenching to KrF laser performance.

PACS numbers: 42.55.Hq, 34.50.-s, 31.50.+w, 82.50.Et

Recent progress in the development of the KrF uv laser has included improvements in its output power,¹ efficiency,² linewidth, and spatial quality of the beam.³ Since quenching of the laser's upper state imposes limitations on saturation intensity and gas mixture composition, knowledge of fundamental collisional rate constants for the $\text{KrF}(B)$ excimer will be required to fully exploit the properties of this molecule as a source of uv stimulated emission.

The rates of quenching of the $\text{KrF}(B)$ state by Ar, Kr, and F_2 and the radiative lifetime of the $\text{KrF}(B \rightarrow X)$ band reported here were determined utilizing pulsed uv photolysis of KrF_2 at 193 nm. Absorption of a 193-nm ($\text{ArF}[B \rightarrow X]$)^{4,5} photon by KrF_2 results in the immediate collisionless dissociation of the molecule, yielding a $\text{KrF}^*(B)$ excimer. Therefore, monitoring the exponential decay of the B -state population (in the presence of the desired diluent gas) affords a direct and accurate method of measuring the KrF excimer's rates of quenching by Ar, Kr, and F_2 .

The experimental apparatus used to photolyze KrF_2 is shown schematically in Fig. 1. A 3-ns FWHM beam of 600-keV electrons from a Febetron 706 generator penetrated a 25- μm -thick Ti foil and irradiated a 99.5% $\text{Ar}/0.5\% \text{F}_2$ (total pressure ≈ 2000 Torr) gas mixture. The fluorescence from this electron-beam-excited plasma, viewed longitudinally through a sapphire window (cutoff ≈ 145 nm) by a Seya-Namioka vacuum spectrograph in first order and Kodak vuv 101-01 film, was found to consist solely of the $\text{ArF}(B \rightarrow X)$ band, centered at 193 nm and of ≈ 1.4 nm FWHM. No F_2^* (158 nm)⁶ or Ar_2F^* (290 nm)⁶ emission was observed. Photodiode studies revealed that the ArF^* emission pulse was characterized by a ≈ 3 -ns FWHM and an exponential decay time of 2.5 ns.

After entering the fused silica absorption tube, the 193-nm radiation photolyzed a fraction of the KrF_2 molecules in the KrF_2 -diluent flow, forming $\text{KrF}(B)$ excimers. The subsequent radiative decay of the KrF^* population at 249 nm was monitored axially by a nar-

row-bandpass filter ($T_{\text{max}} = 21\%$ at 249 nm; FWHM = 4.5 nm) and a fast-rise-time (~ 0.5 ns) S-5 biplanar photodiode. Emission waveforms were recorded using a Tektronix 7904 oscilloscope and later digitized by computer for data analysis.

The KrF_2 used in these experiments was synthesized according to the technique described by Slivnik and co-workers.⁷ Control of the KrF_2 vapor pressure was achieved using a dry ice-ethanol bath. Roughly 0.5 Torr KrF_2 pressure was maintained in the absorption tube by keeping the bath-cooled KrF_2 reservoir at $T \approx -44^\circ\text{C}$. During the experiments, a capacitance manometer recorded the pressure of the KrF_2 -diluent mixture flowing through the photolytic cell. The rare gases and fluorine used in this work were of research and technical (97%) grades, respectively, and passivation of both the absorption tube and Ar/F_2 cell was found to be essential for repeatable results.

Strong photolytic $B \rightarrow X$ fluorescence at 249 nm was obtained with a few tenths of a Torr KrF_2 in the system. Signals (1) were observed to decay exponentially over several e-foldings and (2) occurred only when both Ar and F_2 were present in the excitation cell and KrF_2 was flowing through the quartz tube. (The rapid dissociation of KrF_2 prevented the use of static gas mixtures as was possible with XeF_2 .⁸) These observations indicate that the photolytic process was indeed the

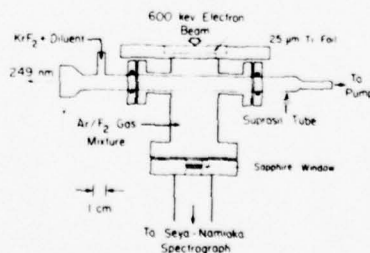


FIG. 1. Schematic diagram of the photolytic apparatus. The Suprasil tube is sealed to the stainless-steel Ar/F_2 cell using O-rings and copper gaskets as shown.

^{a)}Work supported in part by DARPA.

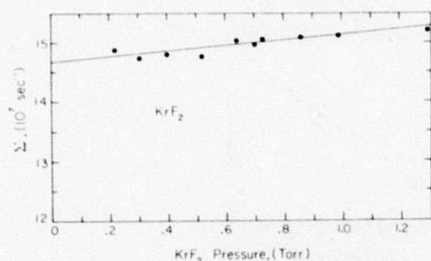


FIG. 2. Graph of decay constant, Σ , as a function of KrF_2 flow pressure. The zero pressure intercept of the least-squares fit to the data (solid line) gives the $\text{KrF}(B \rightarrow X)$ radiative lifetime of 6.8 ns.

pumping mechanism for the $\text{KrF}(B)$ state and the band-pass filter described earlier ensured that $\text{KrF}(B \rightarrow X)$ emission was being monitored.

The analysis and interpretation of the KrF^* waveforms is analogous to that used previously for XeF^* .^{8,9} Briefly, the decaying B -state population is described by a single exponential:

$$[\text{KrF}(B)] = [\text{KrF}(B)]_{t=0} \exp(-\Sigma t), \quad (1)$$

where

$$\Sigma = \tau_r^{-1} + k_1[Q] + k_2[Q]^2, \quad (2)$$

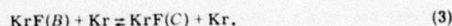
[] indicates particle densities, τ_r is the $\text{KrF}(B \rightarrow X)$ radiative lifetime, and k_1 and k_2 are the two- and three-body rates of quenching of $\text{KrF}(B)$ by the atomic or molecular species Q . The single exponential arises from the rapid formation of $\text{KrF}(B)$ excimers through the collisionless photodissociation process. By varying the partial pressure of the various diluent gases added to the KrF_2 flow, emission waveforms were obtained over a wide range of diluent gas pressures. The falling portion of each waveform was then fit to a single exponential to determine Σ .

The variation of Σ with KrF_2 pressure is shown in Fig. 2 where the least-squares fitting of the data to the linear terms of Eq. (2) is represented by the solid line. The zero KrF_2 pressure intercept of this line gives the radiative lifetime of the $\text{KrF}(B \rightarrow X)$ band as 6.8 ± 0.2 ns where the standard deviation and experimental uncertainty of the data in Fig. 2 are represented by the 0.2-ns error. Although this value is lower than that obtained recently using an ArF laser to photodissociate KrF_2 ,¹⁰ the $\approx 20\%$ difference between the two results is not understood and uncertainties due to the detection system have been eliminated. The present value is in excellent agreement with the theoretical lifetime of 7.0 ns calculated by Hay and Dunning.^{11,12} Two-body destruction of KrF^* by KrF_2 was found to proceed at the rate of $(1.4 \pm 0.4) \times 10^{-10} \text{ cm}^3 \text{ s}^{-1}$.

Figure 3 shows the dependence of Σ on diluent pressure for $\text{KrF}(B)$ quenching by Kr where the quadratic component, representing three-body quenching of the excimer by 2 Kr, becomes clearly evident. The two- and three-body quenching rates for Kr obtained from Fig. 3 are $k_1 = (8.6 \pm 0.7) \times 10^{-12} \text{ cm}^3 \text{ s}^{-1}$ and $k_2 = (9.7$

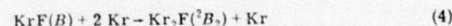
$\pm 0.8) \times 10^{-31} \text{ cm}^6 \text{ s}^{-1}$, respectively, where again the uncertainty in the rate constants shown in parentheses reflects the standard deviation of the data coupled with an estimated experimental error of $\leq 10\%$ per data point. By analyzing e-beam-pumped Ar/Kr/ F_2 mixtures, Rokni, Jacob, and Mangano¹³ inferred a two-body rate almost an order of magnitude smaller ($k_1 < 1.6 \times 10^{-12} \text{ cm}^3 \text{ s}^{-1}$ for $\tau_r = 6.9$ ns) than that reported here. In contrast, the rate given above for three-body quenching of $\text{KrF}(B)$ by krypton is in good agreement with the theoretical prediction of Shui¹⁴ ($5 \times 10^{-31} \text{ cm}^6 \text{ s}^{-1}$) and the result of Rokni *et al.* ($6.4 \times 10^{-31} \text{ cm}^6 \text{ s}^{-1}$).

The absence of a curve crossing between the X (or A) ground state and B excited level of KrF^{12} suggests that the Kr two-body quenching rate is due to mixing collisions between the B and C states:



Such a mechanism is consistent with the proximity of the two states in energy¹¹ and may partially account for the discrepancy in reported Kr two-body rates. For the gas mixtures used in Ref. 13, the $\text{KrF } C$ and B states are likely to be equilibrated due to thermal collisions [Eq. (3)]. Thus, a smaller *net* quenching rate than that presented above may be expected since the C and B levels act essentially as one state. However, the low Kr pressures (≤ 200 Torr) and short pulse lengths employed here make equilibrium unlikely, favoring a larger loss rate for $\text{KrF}(B)$.

The physical interpretation of three-body quenching of $\text{KrF}(B)$ by Kr has been convincingly shown to be the process of Kr_2F^* trimer formation¹⁵:



and culminates in the emission of a $\text{Kr}_2\text{F}(^2B_2 \rightarrow A_1)$ photon at ~ 415 nm. Shui's calculations invoke this mechanism and the good agreement between theory and experiment seems to further support this conclusion.

Similar data for Ar and F_2 are shown in Figs. 4 and 5. From these curves, the rate constants were determined to be $k_1(\text{Ar}) = (1.8 \pm 0.6) \times 10^{-12} \text{ cm}^3 \text{ s}^{-1}$, $k_2(\text{Ar}) = (1.1 \pm 0.4) \times 10^{-31} \text{ cm}^6 \text{ s}^{-1}$, and $k_1(\text{F}_2) = (4.8 \pm 0.3) \times 10^{-10} \text{ cm}^3 \text{ s}^{-1}$. Again, the argon three-body rate is in excellent agreement with theory ($0.9 \times 10^{-31} \text{ cm}^6 \text{ s}^{-1}$)¹⁴ suggesting the formation of stable ArKrF^* trimers. To our knowledge, the two-body quenching rate for Ar has

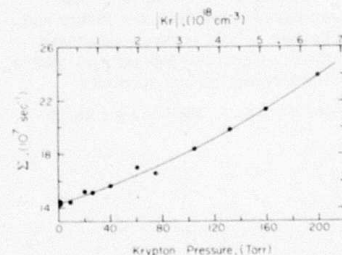


FIG. 3. Dependence of Σ on Kr pressure where, again, the solid line represents the least-squares fit of the data to Eq. (2).

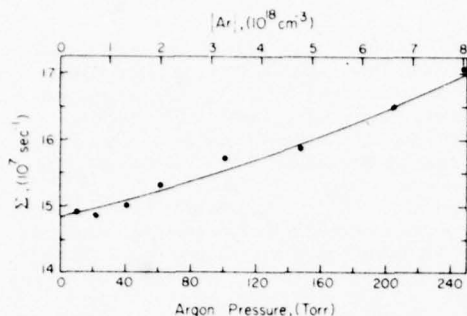


FIG. 4. Variation of Σ with $[\text{Ar}]$. Experimental difficulties in mixing KrF_2 with Ar prevented the study of higher Ar pressures.

not been previously measured and yet is one of the main sources of KrF^* quenching in electron-beam-pumped Ar/Kr/F_2 gas mixtures. For example, for a typical mixture composition of 95% Ar/4.8% Kr/0.2% F_2 (total pressure ≈ 2100 Torr), collisional deactivation of $\text{KrF}(B)$ by two-body collisions with Ar accounts for 17% of the total quenching loss, three-body Ar collisions are responsible for 66%, F_2 for 11%, and all Kr collisions for 6%. Thus, collisional quenching of KrF excimers by Ar greatly exceeds that of the other gas constituents and it is quite possible that replacing argon by neon will result in a significant improvement in laser performance as it has for the XeF laser.^{8,15} From the measured quenching rates and letting $\sigma_{\text{KrF}} = 1.75 \times 10^{-24} \text{ cm}^2 \text{ s}^{-1}$ (Ref. 16), the saturation intensity of the KrF laser, given the gas mixture mentioned above, is 2.6 MW cm^{-2} . In the absence of stimulated emission, a $\text{KrF}(B)$ excimer has an effective lifetime of 1.5 ns.

Finally, preliminary measurements of the quenching rate of $\text{KrF}(B)$ by He give a two-body rate of $\approx 3 \times 10^{-13} \text{ cm}^3 \text{ s}^{-1}$, indicating that the rate constants reported in this paper are not products of vibrational quenching of the B -state manifold. That is, ArF^* photolytic dissociation of KrF_2 appears to produce only low vibrational levels of the $\text{KrF}(B)$ state.

In summary, the $\text{KrF}(B-X)$ radiative lifetime and the two- and three-body collisional quenching rates of $\text{KrF}(B)$ by Kr, Ar, and F_2 have been measured by photolyzing KrF_2 in the presence of the desired diluent and monitoring the resulting $B-X$ radiation at 249 nm. The results are in good agreement with theory and demonstrate the important role of excimer quenching in determining the laser's saturation intensity and power loading of the mirrors forming the optical cavity.

The authors wish to thank L.J. Palumbo for aid in

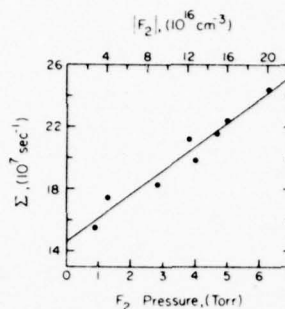


FIG. 5. Plot of decay constant versus F_2 pressure. The slope of the solid line yields the rate of two-body quenching of KrF^* by F_2 .

digitizing the data and C. Mullins and D. Epp for technical assistance.

- ¹G.C. Tisone, A.K. Hays, and J.M. Hoffman, *Opt. Commun.*, **15**, 188 (1975); J.M. Hoffman, A.K. Hays, and G.C. Tisone, *Appl. Phys. Lett.*, **28**, 538 (1976).
- ²L.F. Champagne, 30th Gaseous Electronics Conference, Palo Alto, Calif., 1975, Paper CA-5 (unpublished); R. Burnham and N. Djeu, *Appl. Phys. Lett.*, **29**, 707 (1976).
- ³J. Goldhar and J.R. Murray, *Opt. Lett.*, **1**, 199 (1977).
- ⁴C.A. Brau and J.J. Ewing, *J. Chem. Phys.*, **63**, 4640 (1975); vacuum ultraviolet radiation from $\text{ArCl}(B-X)$ at 175 nm was originally tried as a photolytic source of $\text{KrF}(B)$ molecules but e-beam excitation of Ar/Cl_2 gas mixtures also produces $\text{Cl}_2(E-B)$ fluorescence at 258 nm. This latter continuum fell within the bandpass of the detection filter, interfering with the desired KrF^* emission at 249 nm. Therefore, although ArF^* was found to produce weaker KrF^* emission than did ArCl^* , it was necessary to use the 193-nm radiator to simplify the experiment and data interpretation.
- ⁵J.K. Rice, A.K. Hays, and J.R. Woodworth, *Appl. Phys. Lett.*, **31**, 31 (1977).
- ⁶J.A. Mangano, J.H. Jacob, M. Rokni, and A. Hawryluk, *Appl. Phys. Lett.*, **31**, 26 (1977).
- ⁷J. Slivnik, A. Smalc, K. Lutar, B. Zemva, and B. Frlac, *J. Fluorine Chem.*, **5**, 273 (1975).
- ⁸J.G. Eden and R.W. Waynant, *Opt. Lett.*, **2**, 13 (1978).
- ⁹J.G. Eden and R.W. Waynant, *J. Chem. Phys.* (to be published).
- ¹⁰R. Burnham and S.K. Searles, *J. Chem. Phys.*, **67**, 5967 (1977).
- ¹¹T.H. Dunning, Jr. and P.J. Hay, *Appl. Phys. Lett.*, **28**, 649 (1976).
- ¹²P.J. Hay and T.H. Dunning, Jr., *J. Chem. Phys.*, **66**, 1306 (1977).
- ¹³M. Rokni, J.H. Jacob, and J.A. Mangano, *Phys. Rev. A*, **16**, 2216 (1977).
- ¹⁴V.H. Shui, *Appl. Phys. Lett.*, **31**, 50 (1977).
- ¹⁵L.F. Champagne and N.W. Harris, *Appl. Phys. Lett.*, **31**, 513 (1977).
- ¹⁶A.M. Hawryluk, J.A. Mangano, and J.H. Jacob, *Appl. Phys. Lett.*, **31**, 164 (1977).

KrF(B) quenching by He, Ne, Xe, and NF₃^{a)}

J. G. Eden, R. W. Waynant, S. K. Searles, and R. Burnham

Laser Physics Branch, Naval Research Laboratory, Washington, D. C. 20375
(Received 3 April 1978; accepted for publication 15 June 1978)

Flash photolysis of KrF₂ at 193 nm has been utilized to directly measure the quenching rate constants of KrF(B) molecules by He, Ne, Xe, and NF₃. Investigation of the large rate constant measured for the KrF(B) + Xe reaction ($\approx 10^{-9}$ cm³sec⁻¹) verified the XeF(B) state to be a product.

PACS numbers: 31.50.+w, 32.50.+d, 82.50.Et, 82.20.Pm

I. INTRODUCTION

Experiments of the past year have confirmed the importance of exciplex quenching on XeF and KrF laser performance.¹⁻⁷ Collisional losses due to formation of rare gas-fluoride trimers (R₃F*, R = Xe, Kr) or R F(C) state molecules have been proposed to account for the reported quenching rates which, in turn, are responsible for laser mixture restrictions and require large circulating powers in the optical cavity. For example, argon was commonly used as the diluent in e-beam-pumped XeF laser mixtures until the discovery of the superior quenching¹ and optical absorption⁸ characteristics of neon. The possibility of a similar situation existing for the KrF laser prompted the experimental work described below.

For KrF*, the rates of quenching of KrF(B) molecules by Ar, Kr, and F₂^{9,10} and the radiative lifetime of the B state^{10,11} have been measured previously. This paper describes the direct measurement of the deactivation rates of KrF(B) molecules by He, Ne, Xe, and NF₃, using pulsed uv photolysis of KrF₂. Two obvious advantages of this experimental technique are (1) quenching of the KrF exciplex population by electron impact can be ignored¹² and (2) the various quenching atoms or molecules of interest may be studied independently of one another.

Most of the rates reported here have been measured for the first time. Additional observations suggest that quenching of KrF(B) by Xe results in the formation of XeF(D) molecules followed by collisional or radiative transfer to the B state of XeF.

Section II discusses the experimental technique and data analysis used in this investigation, while Sec. III presents the results for the quenchers mentioned above. Deactivation of KrF(B) by Xe and KrF(B) → XeF* excitation transfer are discussed in Sec. IV and, finally, Sec. V reviews the conclusions of this study.

II. EXPERIMENTAL TECHNIQUE AND DATA ANALYSIS

A schematic diagram of the experimental apparatus used to photolyze KrF₂¹⁰ is shown in Fig. 1. Briefly, ArF(B → X) emission from electron-beam-irradiated Ar/F₂ gas mixtures (99.5% Ar/0.5% F₂; $p_{\text{total}} \approx 2000$ Torr) photolyzed KrF₂ molecules in a KrF₂-diluent stream flowing through a Suprasil (VUV quality) quartz tube. A Seya-Namioka vacuum spectrograph (in first order) recorded the ArF* emission spectrum shown in Fig. 2 by viewing the flu-

orescence through a sapphire window ($\lambda_{\text{cutoff}} \sim 145$ nm). The spectral FWHM shown in Fig. 2 is ~ 1.2 nm which corresponds to $\Delta E \sim 320$ cm⁻¹. Using a solar blind photodiode, the ArF* emission pulse was found to closely follow the electron-beam current.

As mentioned in Ref. 10, the KrF₂ used in these experiments was synthesized according to the technique described by Slivnik *et al.*¹³ The KrF₂ crystals were contained in a Pyrex vessel which in turn was immersed in a dry-ice-alcohol bath. Mixing of the desired quenching gas with the KrF₂ vapor was accomplished by flowing the gas over the crystals as shown in Fig. 1. The KrF₂ vapor pressure was maintained at ≈ 0.5 Torr in these experiments by keeping the dry-ice-alcohol bath at $T \sim -44^\circ\text{C}$. Diluent was then added to raise the total flow pressure (measured by a capacitance manometer) to the desired value. Although improvements have been made in the flow system,¹⁰ gas mixing difficulties prevented study of diluent pressures in excess of 1000 Torr. All gas-handling lines were 6-mm o.d. Teflon tubing. Also, flowing KrF₂ vapor through the quartz tube for several minutes prior to the experiments was found to be important for obtaining repeatable results. Details of the quartz absorption tube and Ar/F₂ photolytic cell have been published in a recent paper.¹⁰

Subsequent to absorbing a 193-nm photon, a KrF₂ molecule dissociates,^{10,14} creating a KrF(B) exciplex by the collisionless process:

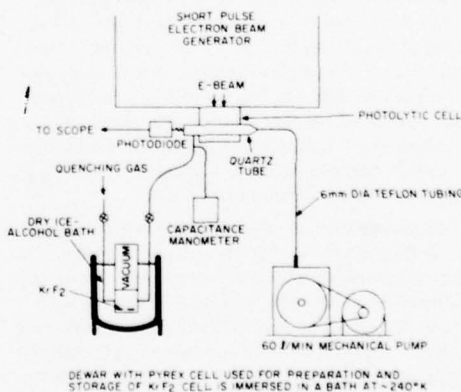


FIG. 1. Partial schematic diagram of the experimental apparatus used to photolyze KrF₂ and measure rates of quenching of KrF(B) by various gases. Details of the construction of the quartz absorption tube and Ar/F₂ photolytic cell are given in Ref. 10.

^{a)}Work supported in part by DARPA.

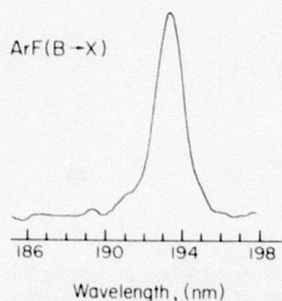
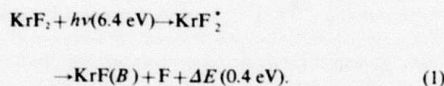


FIG. 2. ArF($B \rightarrow X$) emission spectrum at 193 nm from e-beam-excited Ar/F₂ gas mixtures. The detection system resolution was ~ 0.3 nm and the vertical scale is logarithmic.



The KrF($B \rightarrow X$) 249-nm emission waveforms were monitored by a S-5 surface photodiode (~ 0.5 nsec rise time) and narrow bandpass filter ($T_{\text{max}} = 21\%$ at 249 nm; $\Delta\lambda = 4.5$ nm) and the traces were recorded on film using a Tektronix 7904 oscilloscope. The measured rapid rise in KrF($B \rightarrow X$) fluorescence following the onset of ArF excitation suggested that the dissociation of KrF₂^{*} by Eq. (1) was rapid (< 1 nsec).

Since no collisions are required to form the KrF(B) population, the extraction of quenching rates from the pressure-dependent fluorescence data is straightforward. Simple kinetic rate equations^{1,4,10} predict-decaying waveforms described by a single exponential decay constant Σ :

$$\Sigma \equiv \tau_r^{-1} + k_1 [Q] + k_2 [Q]^2 + k_3 [\text{KrF}_2], \quad (2)$$

where τ_r is the KrF($B \rightarrow X$) radiative lifetime of 6.8 nsec,¹⁰ k_1 and k_2 are the two- and three-body rates of quenching of KrF(B) by the diluent Q , and k_3 is the rate constant for quenching of KrF(B) by KrF₂ (1.4×10^{-10} cm³ sec⁻¹).¹⁰ Experiments confirm the single exponential nature of the fluorescence signals as shown in Fig. 3 which presents typical ArF* and KrF($B \rightarrow X$) emission waveforms. The ArF trace is characterized by a 2.5-ns decay constant, whereas the KrF signal, corresponding to a 0.5 Torr KrF₂ plus 21 Torr Ne gas mixture, has a decay constant of ≤ 6.8 nsec.

To determine the KrF(B) quenching rate for a given diluent, the fluorescence waveforms for various diluent pressures were digitized from the oscillograms and plotted on semilog scales by a CDC 3800 computer. Then, for each pressure, Σ was determined by fitting the falling portion of the signal to a single exponential and correcting for the non-zero decay time of the ArF* excitation pulse by deconvolving the pump and KrF fluorescence waveforms. This correction is $< 20\%$ for signal decay times ≥ 5 nsec. From a graph of Σ versus $[Q]$, determinations of k_1 and k_2 could then be made.

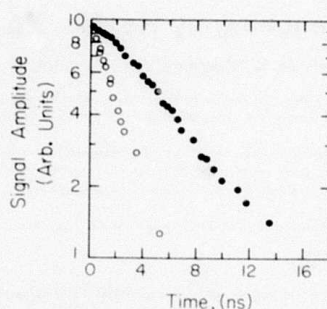


FIG. 3. ArF($B \rightarrow X$) (○) and KrF($B \rightarrow X$) (●) fluorescence waveforms typical of those encountered in these experiments. The ArF* emission was observed from e-beam-excited 2000 Torr Ar/10 Torr F₂ mixtures with a band-pass filter ($T_{\text{max}} = 20\%$ at 198.0 nm; $\Delta\lambda = 20$ nm) and a solar blind photodiode. The KrF radiation was due to a 0.5 Torr KrF₂-21 Torr Ne gas mixture flowing through the reaction cell. $T = 0$ identifies the time of peak e-beam current.

III. RESULTS AND DISCUSSION

The dependence of Σ on helium pressure is shown in Fig. 4 where the least-squares fitting of the data points is represented by the solid line. The slope of this line gives the rate of quenching of KrF(B) by a two-body collision with He as $(3.3 \pm 1.1) \times 10^{-11}$ cm³ sec⁻¹ where the experimental and statistical uncertainty of the rate constant is given in the parentheses. Due to the $\sim 15\%$ per data point uncertainty in Σ , the three-body quenching rate for He was estimated to be $\leq 10^{-13}$ cm³ sec⁻¹. Given 2 atm of He in a discharge-pumped KrF laser mixture, the rate of helium quenching of KrF(B) is 1.6×10^7 sec⁻¹, thus reducing the effective lifetime of a KrF exciplex by 10% to 6.1 nsec.

The contrast between Ne and Ar as KrF quenchers is clearly shown in Fig. 5 where the Ar data was taken from Ref. 10. Again, the solid lines represent the least-squares fitting of the data points. For neon, the two-body KrF(B) quenching rate, $k_1(\text{Ne}) = (1.6 \pm 0.4) \times 10^{-12}$ cm³ sec⁻¹, is simi-

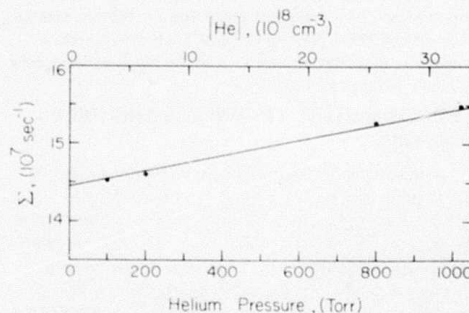


FIG. 4. Graph of Σ versus He pressure. The solid line represents the least-squares fit of the data points to the linear terms of Eq. (2). The experimental uncertainty in Σ per point is $\leq 15\%$ and the error in p_{He} is negligible.

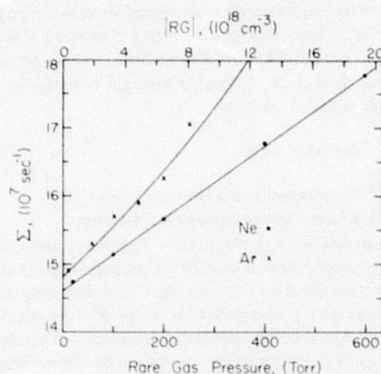


FIG. 5. Comparison of quenching of $\text{KrF}(B)$ by Ne and Ar. The different vertical axis intercepts are due to slightly different KrF_2 flow pressure used in the two experiments.

lar to that measured for Ar, $(1.8 \pm 0.6) \times 10^{-12} \text{ cm}^3 \text{ sec}^{-1}$. The key difference between the two diluents lies in the three-body rate constants which for neon is estimated to be $< 10^{-12} \text{ cm}^3 \text{ sec}^{-1}$ while for argon, $k = (1.1 \pm 0.4) \times 10^{-11} \text{ cm}^3 \text{ sec}^{-1}$.

To compare argon and neon as diluents for e-beam-pumped KrF lasers, consider a typical 95% Ar/4.8% Kr/0.2% F_2 gas mixture with a total pressure of 2100 Torr. From the KrF^* quenching rates for Ar, Kr, and F_2 determined previously,¹⁰ Ar accounts for 83% of the collisional losses, Kr for 6%, and F_2 for 11%. Substituting neon for argon (and doubling the diluent concentration to maintain constant electron energy deposition) reveals that neon accounts for 86% of the B-state quenching losses. Therefore, exchanging argon for neon does not substantially change diluent quenching and so any advantage of neon over argon (as is the case for XeF^{*13}) will depend on KrF formation kinetics in Ne/Kr/ F_2 mixtures.

Figure 6 shows the results for NF_3 where the two-body quenching rate is $(5.2 \pm 0.5) \times 10^{-11} \text{ cm}^3 \text{ sec}^{-1}$. As with XeF^* , NF_3 quenches $\text{KrF}(B)$ molecules roughly an order of magnitude less effectively than does F_2 . However, it is well known that NF_3 does not perform as well as F_2 in KrF laser systems, which is probably due to NF_3 (or its fragments, e.g., NF_2) absorption at 250 nm¹⁴ or to the importance of F_2^+ molecules in the exciplex formation chain.

IV. $\text{KrF}(X)$ QUENCHING BY Xe AND $\text{KrF}(B) \rightarrow \text{XeF}^*$ EXCITATION TRANSFER

Xenon was found to quench $\text{KrF}(B)$ molecules at a surprisingly large rate as shown by Fig. 7. The slight spread of the data points does not accurately reflect the experimental error due to the low xenon pressures (< 1.5 Torr) and large decay constants involved. For this reason, error bars are given in Fig. 7. Each data point has been corrected for uncertainties in the KrF_2 pressure which arose from slight variations in the temperature of the alcohol-dry-ice bath used to control the KrF_2 flow pressure. Fluctuations in the bath

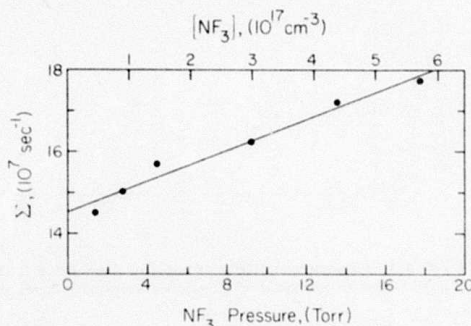


FIG. 6. Variation of decay constant Σ with NF_3 concentration. The slope of the solid line is $5.2 \times 10^{-11} \text{ cm}^3 \text{ sec}^{-1}$ and again the error in the decay constant per data point is $\sim 15\%$.

temperature of as little as 1 °C caused KrF_2 pressure deviations of 0.05 Torr. This, in turn, created an uncertainty of ± 0.05 Torr in the xenon pressure since the capacitance manometer monitored the total flow pressure ($p_{\text{KrF}_2} + p_{\text{Xe}}$).

Including the experimental uncertainties mentioned above and statistical errors arising from the least-squares fit, the data of Fig. 7 give a lower limit for the rate constant for two-body quenching of $\text{KrF}(B)$ by Xe of $\sim 10^{-9} \text{ cm}^3 \text{ sec}^{-1}$. Preliminary studies by other investigators¹⁵ have yielded a half-quenching pressure of ~ 1.8 Torr or $k = 2.5 \times 10^{-9} \text{ cm}^3 \text{ sec}^{-1}$ (setting $\tau_{\text{KrF}(B)} = 6.8 \text{ nsec}$) for this reaction. Our result is also consistent with the findings of Rokni and co-workers⁹ who found the analogous displacement reaction: $\text{ArF}^* + \text{Kr} \rightarrow \text{KrF}^* + \text{Ar}$ to proceed with a rate constant of $1.6 \times 10^{-9} \text{ cm}^3 \text{ sec}^{-1}$.

In an attempt to determine the products of the $\text{KrF}(B) + \text{Xe}$ quenching mechanism, fluorescence at 350 nm

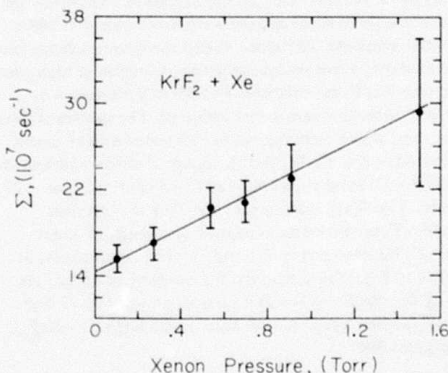


FIG. 7. Quenching data for xenon including corrections for the 2.5-nsec decay time of the ArF^* fluorescence. The error bars indicate the estimated experimental errors for the low pressure measurement. The solid line denotes the linear least-squares fitting of the data points. The lower limit for $k(\text{Xe})$ is $10^{-9} \text{ cm}^3 \text{ sec}^{-1}$.

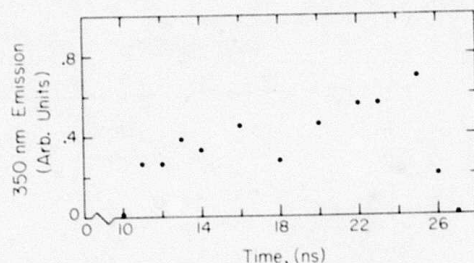


FIG. 8. Time dependence of $\text{XeF}(B \rightarrow X)$ emission observed from 0.5 Torr KrF_2 -14 Torr Xe mixtures. $T=0$ corresponds to peak ArF^* fluorescence.

[emitted by low-lying $\text{XeF}(B)$ vibrational levels] from KrF_2 -Xe photolyzed mixtures was monitored by a narrow band-pass filter ($\lambda_0 = 348 \text{ nm}$, $\Delta\lambda = 9.4 \text{ nm}$) and a S-5 photodiode. $\text{XeF}(B \rightarrow X)$ emission was observed but, as shown in Fig. 8, the onset of the fluorescence was delayed by $\sim 10 \text{ nsec}$ from the peak of the ArF pulse. This effect may be explained by considering the relative energies of the $\text{KrF}(B)$, $\text{XeF}(D)$, and $\text{XeF}(B)$ states. Using the spectroscopic constants given by Tellinghuisen *et al.*¹⁷ for the D level of XeF and those for $\text{KrF}(B)$ calculated by Hay and Dunning,¹⁸ several close energy coincidences ($< 300 \text{ cm}^{-1}$) between the $\text{KrF}(B, v' = 0, 1)$ and $\text{XeF}(D, v'' = 12-14)$ vibrational levels were found. Thus, those near-resonant states allow for $\text{KrF}(B) \rightarrow \text{XeF}(D)$ excitation transfer followed by collisional or radiative cascading to the $\text{XeF}(B)$ state. Since the mixture pressure of Fig. 8 is low ($< 15 \text{ Torr}$), collisional relaxation of the $\text{XeF}(B$ and $D)$ state vibrational manifolds will be slow, in agreement with the observed time delay. Also, the 10-nsec lapse before the $B \rightarrow X$ radiation was detected minimizes the possibility of direct $\text{KrF}(B) \rightarrow \text{XeF}(B, \text{low } v'')$ transfer. Second, the 350-nm radiation is emitted over $\sim 16 \text{ nsec}$, indicating a relatively slow "feeding" of low-lying $\text{XeF}(B)$ vibrational levels.

Although it is desirable to directly observe the $\text{XeF}(D \rightarrow X)$ emission at 260 nm, a filter of sufficiently narrow response to eliminate the $\text{KrF}(B \rightarrow X)$ band at 249 nm was not available. Therefore, to test the kinetic scheme proposed above, experiments involving excitation of high pressure Ar/Kr/F_2 gas mixtures by a 450-kV 50-nsec $\sim 1\text{-kA}$ cm^{-2} electron beam were conducted. The spectra of these mixtures, which were typical of those used as KrF lasers (95% $\text{Ar}/4.8\% \text{ Kr}/0.2\% \text{ F}_2$), consisted of the well-known $\text{KrF}(B \rightarrow X)$ band at 249 nm and $C \rightarrow A$ continuum at $\sim 275 \text{ nm}$ [cf. Fig. 9(a)]. Adding just one Torr of Xe to this Ar/Kr/F_2 mixture produced intense $\text{XeF}(B \rightarrow X)$ and $(D \rightarrow X)$ fluorescence at 351 and 260 nm, respectively, as shown in Fig. 9(b). Certainly, the intensity of neither the $B \rightarrow X$ nor the $D \rightarrow X$ bands is characteristic of $\text{Ar}/1 \text{ Torr Xe}/\text{F}_2$ gas mixtures but is consistent with $\text{KrF}(B) \rightarrow \text{XeF}(D)$ energy transfer.

The large ratios of $[\text{Ar}]/[\text{Xe}]$ and $[\text{Kr}]/[\text{Xe}]$ were chosen so that the kinetic chain forming $\text{KrF}(B)$ would be negligibly perturbed by the addition of 1 Torr Xe to the gas mixture of Fig. 9(a). In electron-beam excited rare gas plasmas,

the bulk of the deposited electron energy produces rare gas atomic ions (in this case, Ar^+). For the gas mixture of Fig. 9(a) (2000 Torr $\text{Ar}/100 \text{ Torr Kr}/5 \text{ Torr F}_2$), these Ar^+ ions rapidly collide with the Ar background gas to form Ar_2^+ . The charge transfer reaction



is known^{19,20} to proceed at a large rate ($k \approx 6 \times 10^{10} \text{ cm}^3 \text{ sec}^{-1}$), whereas the competing mechanism ($\text{Ar}_2^+ + \text{Xe} \rightarrow \text{Xe}^+ + 2\text{Ar}$), due to the 1 Torr Xe added in Fig. 9(b), is expected to have a smaller rate constant due to the $\sim 1\text{-eV}$ exothermicity of the reaction.¹⁹ Also, the competing ion recombination processes $\text{Kr}^+(\text{or Xe}^+) + \text{F} + \text{Ar} \rightarrow \text{KrF}^*(\text{or XeF}^*) + \text{Ar}$ have comparable rate constants.²¹ Therefore, the spectra of Fig. 9 support the conclusion that formation of both the $\text{XeF}(D$ and $B)$ states result from the quenching of $\text{KrF}(B)$ by Xe.

A summary of the experimentally determined rate constants for quenching of the $\text{KrF}(B)$ state by various gases is given in Table I. Some of the rate constants determined by other investigators depend on τ , and so the values presented in Table I assume $\tau = 6.8 \text{ nsec}$.

Since the experimental technique used in the present work measures only the rate at which the $\text{KrF}(B)$ state molecules are destroyed, the products of the various quenching collisions shown in Table I are not known. In a previous paper,¹⁰ the discrepancy between the reported two-body rate constants for Kr was attributed to mixing between the $\text{KrF } B$ and C states:

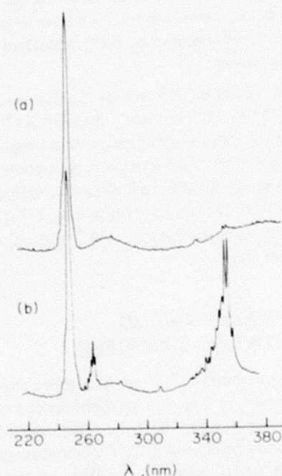
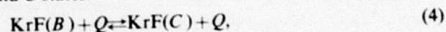


FIG. 9. Spectra recorded from e-beam-excited mixtures: (a) 2000 Torr $\text{Ar}/100 \text{ Torr Kr}/5 \text{ Torr F}_2$ mixture, clearly showing the KrF 249- and 275-nm bands and (b) same mixture as (a) with a Torr of Xe added. Vertical scale for both spectral profiles is logarithmic.

TABLE I. Rate constants for quenching of $\text{KrF}(B)$ by various gases.

Quencher	Rate constant ^a	Reference
He	$(3.3 \pm 1.1) \times 10^{-11}$	This work
2He	$\leq 10^{-12b}$	This work
Ne	$(1.6 \pm 0.4) \times 10^{-12}$	This work
2Ne	$< 10^{-12b}$	This work
Ar	$(1.8 \pm 0.6) \times 10^{-12}$	10
2Ar	$(7.6 \pm 0.7) \times 10^{-12b}$	7, 9
	$(1.1 \pm 0.4) \times 10^{-11}$	10
Kr	$< 1.6 \times 10^{-12}$	9
	$(8.6 \pm 0.7) \times 10^{-12}$	10
Ar + Kr	6.2×10^{-12b}	9
2Kr	6.5×10^{-12b}	9
	2.9×10^{-11}	5
	$(9.7 \pm 0.8) \times 10^{-11}$	10
Xe	$> 10^{-9}$	This work
F ₂	7.4×10^{-10}	9
	5.7×10^{-10}	5
	$(4.8 \pm 0.3) \times 10^{-10}$	10
NF ₃	$(5.2 \pm 0.5) \times 10^{-11}$	This work

^aUnits = $\text{cm}^3 \text{sec}^{-1}$.^bUnits = $\text{cm}^3 \text{sec}^{-1}$.

where, again, Q is the diluent gas of interest. This process may also be important for the quenching reactions studied here and particularly for He and Ne where large diluent concentrations were used to measure the desired rate constants.

V. CONCLUSIONS

The rates of quenching of $\text{KrF}(B)$ by He, Ne, Xe, and NF_3 have been reported in this paper. Simple exponentially decaying waveforms were obtained by photolyzing KrF_2 in the presence of the desired diluent with 193-nm radiation. The results underscore the significance of quenching studies to an understanding of basic decay processes of the exciplex population.

ACKNOWLEDGMENTS

The authors wish to express their thanks to C. Mullins and D. Epp for excellent technical assistance.

- ¹H. C. Brashears, Jr., D. W. Setser, and D. DesMarteau, *Chem. Phys. Lett.* **48**, 84 (1977).
²M. Rokni, J. H. Jacob, J. A. Mangano, and R. Brochu, *Appl. Phys. Lett.* **30**, 458 (1977).
³J. G. Eden and R. W. Waynant, *Opt. Lett.* **2**, 13 (1978).
⁴J. G. Eden and R. W. Waynant, *J. Chem. Phys.* **68**, 2850 (1978).
⁵G. P. Quigley and W. M. Hughes, *Appl. Phys. Lett.* **32**, 627 (1978).
⁶C. H. Fisher and R. E. Center, *Bull. Am. Phys. Soc.* **23**, 132 (1978).
⁷J. A. Mangano, J. H. Jacob, M. Rokni, and A. Hawryluk, *Appl. Phys. Lett.* **31**, 26 (1977).
⁸L. F. Champagne and N. W. Harris, *Appl. Phys. Lett.* **31**, 513 (1977).
⁹M. Rokni, J. H. Jacob, and J. A. Mangano, *Phys. Rev. A* **16**, 2216 (1977); J. H. Jacob, M. Rokni, J. A. Mangano, and R. Brochu, *Appl. Phys. Lett.* **32**, 109 (1978).
¹⁰J. G. Eden, R. W. Waynant, S. K. Searles, and R. Burnham, *Appl. Phys. Lett.* **32**, 733 (1978).
¹¹R. Burnham and S. K. Searles, *J. Chem. Phys.* **67**, 5967 (1977).
¹²J. G. Eden and S. K. Searles, *Appl. Phys. Lett.* **29**, 356 (1976).
¹³J. Shvnik, A. Smalc, K. Lutar, B. Zemva, and B. Frlc, *J. Fluorine Chem.* **5**, 273 (1975).
¹⁴G. N. Makeev, V. F. Sinyanskii, and B. M. Smirnov, *Dokl. Akad. Nauk. SSSR* **222**, 151 (1975).
¹⁵M. Rokni, J. H. Jacob, J. A. Mangano, and R. Brouchu, *Appl. Phys. Lett.* **32**, 223 (1978).
¹⁶D. W. Setser, Quarterly Progress Report, ERDA Contract No. EY-76-S-02-289-A001, 1977 (unpublished).
¹⁷P. C. Tellinghuisen, J. Tellinghuisen, J. E. Velazco, J. A. Coxon, and D. W. Setser (unpublished).
¹⁸P. J. Hay and T. H. Dunning Jr., *J. Chem. Phys.* **66**, 1306 (1977). Their notation designates the $\text{KrF}(B)$ state as III₁.
¹⁹D. K. Bohme, N. G. Adams, M. Mosesman, D. B. Dunkin, and E. E. Ferguson, *J. Chem. Phys.* **52**, 5094 (1970).
²⁰R. Johnsen, J. Macdonald, and M. A. Biondi, *J. Chem. Phys.* **68**, 2991 (1978).
²¹M. R. Flannery and T. P. Yang, *Appl. Phys. Lett.* **32**, 327 (1978).

HgX(B) radiative lifetime by fast photolysis of HgX₂ (X = Br, I)^{a)}

R. W. Waynant and J. G. Eden

Naval Research Laboratory, Washington D.C. 20375
(Received 19 June 1978; accepted for publication 31 July 1978)

The radiative lifetimes of the HgBr(B) and HgI(B) states have been determined to be 23.7 ± 1.5 and 27.3 ± 2.0 ns, respectively, by fast photolysis of HgBr₂ and HgI₂ using e-beam-excited ArF and KrCl fluorescence. This experimental approach generated simple exponential decay curves which facilitated measurement of the lifetimes and the rate of quenching of the excited HgX(B) states by HgX₂ (X = Br or I) molecules. Although the lifetimes reported here are in agreement with previous experimental measurements, they contradict a recently published theoretical calculation.

PACS numbers: 82.50.Et, 33.50.-j, 31.70.Hq, 42.55.Hq

Laser emission on the HgBr(B → X) transition has been produced by electron-beam pumping of mixtures of Ar, Xe, Hg, and HBr¹; by electron beam sustained discharge pumping of Ar, Hg, and BrCCl₃ mixtures²; by using an ArF laser (193 nm) to photodissociate HgBr₂ to produce HgBr(B)³; and by dissociating HgBr₂ in a fast transverse electric discharge.^{4,5} These latter experiments also were able to dissociate HgI₂ to produce lasing on the HgI(B → X) band.

The technique of producing an HgX (X = Br, I) laser by dissociating the HgX₂ molecule is of practical interest since the HgX molecule in its ground state may recombine with a free halogen atom to form HgX₂, and, therefore, the laser can operate repetitively in a sealed system. Energies of ~7 mJ already have been obtained from these rare-gas/HgX₂ salt vapor discharges,⁵ but optimal design requires knowledge of excited-state lifetimes and quenching rates.

In recent experiments, Eden⁶ has measured the radiative lifetime of the HgCl(B → X) transition as 22.2 ± 1.5 ns and the quenching rate of HgCl(B) by HgCl₂ as 9×10^{-11} cm³ s⁻¹. In this paper, the lifetimes of HgX(B) (X = Br, I) and the rate constants for quenching of HgX(B) by HgX₂ have been determined by rapidly photodissociating HgX₂. Spontaneous emission from either the ArF or KrCl molecules was used as the photolytic pump source. The results reveal excited-state lifetimes which do not conform to the theoretical calculations of Duzy and Hyman.⁷

The experimental system used to make the lifetime and quenching measurements is shown in Fig. 1. A Febetron 706 is used to deliver a 3-ns 600-kV voltage pulse to an impedance-matched diode of coaxial geometry similar to that reported by Bradley and co-workers.⁸ The 25-μm-thick aluminum cylindrical anode was filled either with Ne:Ar:F₂ (2000:400:10 Torr) to produce ArF radiation (λ = 193 nm)⁹ for photodissociation of HgBr₂ or with Ar:Kr:Cl₂ (2000:200:10 Torr) gas mixtures to produce KrCl radiation¹⁰ (λ = 222 nm) for photodissociation of HgI₂. Although e-beam excitation of Ar/Kr/Cl₂ mixtures also produces ArCl* (175 nm) and Cl₂(E → B) radiation at 258 nm in addition to

KrCl fluorescence, the ArCl* emission is absorbed in air before reaching the heated cell and HgI₂ is transparent to the Cl₂ 258-nm radiation.¹¹ The electron-beam cell was thoroughly passivated with technical purity F₂ or Cl₂, and research-grade rare gases were used for the high-pressure mixtures. Suprasil quartz windows were mounted at each end of the e-beam cell. The rare-gas-halide excimer radiation was monitored at one end of the cell by a fast-rise-time (~0.5 ns) ITT F4018 photodiode with a S-5 surface and a narrow-bandpass filter (λ₀ = 198 or 221 nm; Δλ ~ 20 nm). These filters transmit 19% at 193 nm and 25% at 222 nm, respectively. Both the ArF (193 nm) and KrCl (222 nm) spontaneous emission waveforms were observed to have a FWHM of ~2.5 ns and decay times of ~3–4 ns.

Radiation from the other end of the diode was directed into an oven-heated quartz cell containing a few mg of the desired mercuric halide salt. These optical cells were evacuated to < 10⁻⁵ Torr and baked prior to filling with HgX₂. Also, the HgX₂ was distilled over a hydrogen flame to drive off impurities before being sealed. In some cells, 100 Torr of He also was added to study the effects of vibrational relaxation on the apparent HgX* radiative lifetime. Oven temperature was monitored carefully by a thermometer and the HgX₂ particle density was determined from vapor-pressure curves.¹²

The fluorescent emission from the HgX(B) molecules

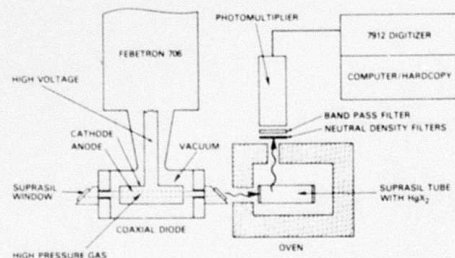
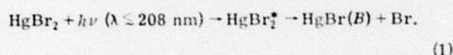


FIG. 1. Partial schematic diagram of the experiment. Details of the experimental technique are given in the text.

^{a)}Work supported in part by DARPA.

was monitored at right angles to the cell by an EMI 9818QB photomultiplier mounted in both a rf- and x-ray-shielded housing. The spectral regions of interest (500 nm for HgI and 440 nm for HgBr) were selected by bandpass filters transmitting over about 15 nm bandwidth and nearly centered about the wavelength of interest. It was necessary to attenuate the $\text{HgX}(B \rightarrow X)$ fluorescence signals with neutral density filters to avoid saturating the photomultiplier. The time response of the photomultiplier system was calibrated by allowing it to view the excitation pulse from the diode through the ultraviolet filters described earlier. The HgBr and HgI $B \rightarrow X$ spontaneous emission signals from the photomultiplier were recorded using a Tektronix 7912 digitizer, Tektronix 1152 computer, and a hard copy printer. The curves were then redigitized and plotted on semilog scales using a CDC 3800 computer.

Maya¹¹ has measured the uv absorption spectra of both HgBr_2 and HgI_2 and found that the threshold wavelengths for photoproduction of the $\text{HgBr}(B)$ and $\text{HgI}(B)$ states are ~ 205 and 235 nm, respectively. For example,



Therefore, since the process pumping the $\text{HgX}(B)$ state is collisionless and the pulse widths of the ArF and KrCl pump radiation are considerably less than the estimated B -state lifetimes,⁷ then to a first approximation the temporal dependence of the desired HgX population density is given by

$$[\text{HgX}(B)] = [\text{HgX}(B)]_{t=0} \exp(-t/\tau), \quad (2)$$

where

$$\tau^{-1} = \tau_r^{-1} + k_Q[\text{HgX}_2], \quad (3)$$

[] indicate particle densities, τ_r is the $\text{HgX}(B \rightarrow X)$ radiative lifetime, and k_Q is the rate constant for quenching of the $\text{HgX}(B)$ state by HgX_2 . This simple kinetic rate equation approach is analogous to that described previously in more detail for the XeF and KrF excimer molecules.¹³

The emission waveforms were clean and decayed exponentially over two orders of magnitude of amplitude and several decay constants. The falling portion of each waveform was fit to a single exponential to determine τ for that particular $[\text{HgX}_2]$. Hence, by simply plotting τ for various HgX_2 vapor pressures, k_Q and τ_r could be determined.

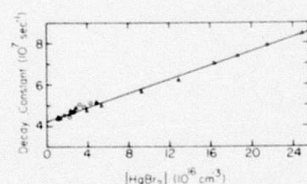


FIG. 2. Dependence of the exponential decay constant τ on $[\text{HgBr}_2]$. Data with (\circ) and without (Δ) 100 Torr of helium in the HgBr_2 cell are shown. The zero-density intercept yields the $\text{HgBr}(B)$ state radiative lifetime of 23.7 ns.

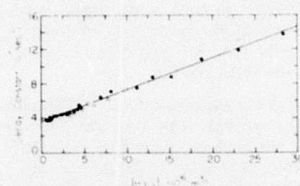


FIG. 3. Variation of τ with $[\text{HgI}_2]$ for photolysis of $\text{HgI}_2 + 100$ Torr He at 222 and 193 nm. The KrCl data (\circ) gives the $\text{HgI}(B)$ state lifetime as 27.3 ns, whereas ArF photodissociation (Δ) shows a longer apparent lifetime due to a higher $\text{HgI}(B)$ vibrational distribution. A representative data point with no helium and using KrCl photolysis (Δ) is also shown.

Figure 2 shows the dependence of τ on $[\text{HgBr}_2]$, where the solid line represents the least-squares fit of Eq. (3) to the data. The triangles shown in Fig. 2 represent data taken with no He in the absorption cell, whereas the open circles represent data with 100 Torr of helium in the tube. Although not shown, the $\text{HgBr}_2 + \text{He}$ data closely followed, for all values of $[\text{HgBr}_2]$, that measured with just HgBr_2 in the tube, indicating that, as expected, only low $\text{HgBr}(B)$ vibrational levels are produced by ArF photolysis of HgBr_2 . The zero-density intercept of the least-squares line gives the $\text{HgBr}(B)$ lifetime as 23.7 ± 1.5 ns, which is in excellent agreement with the results obtained by Djeu and Mazza¹⁴ using a laser-induced fluorescence technique.

As mentioned previously, the HgI_2 wavelength threshold for photodissociation is ~ 230 nm, and thus lower $\text{HgI}(B)$ vibrational levels are created when the salt is photolyzed with KrCl radiation. Data using both KrCl (\bullet) and ArF (\circ) to photodissociate HgI_2 (in the presence of 100 Torr He) are shown in Fig. 3, where the ArF data leads to a lifetime of 36.2 ns and a k_Q of $4.5 \times 10^{-10} \text{ cm}^3 \text{ s}^{-1}$. However, the ArF radiation of 193 nm can excite vibrational levels ~ 1 eV above the $v' = 0$ level of the B state, and vibrational relaxation of the various levels could affect the apparent radiative lifetime. For KrCl excitation, where only low vibrational levels are excited, the data show a radiative lifetime of 27.3 ns and a quenching rate of $3.6 \times 10^{-10} \text{ cm}^3 \text{ s}^{-1}$. Evidently, then, the radiative lifetime of the $\text{HgI}(B)$ state rises slightly with increasing vibrational number. Finally, the fluorescent yield from HgI^* using KrCl photodissociation is much higher than that obtained using ArF,

TABLE I. Summary of radiative lifetimes of the $\text{HgX}(B)$ states ($X = \text{Cl}, \text{Br}, \text{I}$) and rate constant for quenching of $\text{HgX}(B)$ by HgX_2 .

	Experimental lifetime	Theory (Ref. 7)	k_Q ($\text{cm}^3 \text{ s}^{-1}$)
HgCl	22.2 ns (Ref. 6)	20 ns	9.2×10^{-11} (Ref. 6)
HgBr	23.7 ns 23.2 ns (Ref. 14)	16	1.7×10^{-10}
HgI	27.3 ns	12	3.6×10^{-10}

which is also consistent with Maya's absorption measurements. Again, with no He in the HgI₂ tube and using KrCl photolysis, the data (Δ , only one point shown for clarity) follows the solid circles.

Table I summarizes the experimental and theoretical data for HgCl, HgBr, and HgI. The theoretical results of Duzy and Hyman, while close to the experimental value for HgCl, predicted shorter lifetimes for the heavier halides, which contrasts with these observations. Duzy and Hyman's neglect of spin orbit effects, which become increasingly important for Br and I, may contribute to the discrepancy. The increased quenching seen from the heavier salt vapors also may account for the poor performance seen by Burnham⁵ for the HgI₂ dissociation laser.

The lifetimes and quenching rates measured here should be useful for prediction of mercury halide laser performance and design of higher-power systems. Further measurements of mercury halide quenching by other gases important to these lasers are in progress and will be reported later.

The authors gratefully acknowledge the technical

assistance of D. Epp and helpful discussions with R. Burnham.

- ¹J.H. Parks, Appl. Phys. Lett. **31**, 297 (1977).
- ²W.T. Whitney, Appl. Phys. Lett. **32**, 239 (1978).
- ³E.J. Schimitschek, J.F. Celto, and J.A. Trias, Appl. Phys. Lett. **31**, 608 (1977).
- ⁴E.J. Schimitschek and J.F. Celto, Opt. Lett. **2**, 64 (1978).
- ⁵R.L. Burnham, Appl. Phys. Lett. **33**, 156 (1978).
- ⁶J.G. Eden, Appl. Phys. Lett. **33**, 495 (1978).
- ⁷C. Duzy and H.A. Hyman, Chem. Phys. Lett. **52**, 345 (1977).
- ⁸D.J. Bradley, D.R. Hull, M.H.R. Hutchinson, and M.W. McGeoch, Opt. Commun. **11**, 335 (1974).
- ⁹J.R. Murray and H.T. Powell, in *Electronic Transition Lasers II*, edited by L.E. Wilson, S.N. Suchard, and J.I. Steinfeld (MIT, Cambridge, Mass., 1977), pp. 23-29.
- ¹⁰J.R. Murray and H.T. Powell, Appl. Phys. Lett. **29**, 252 (1976).
- ¹¹J. Maya, J. Chem. Phys. **67**, 4976 (1977).
- ¹²*Handbook of Chemistry and Physics*, edited by R. Weast (Chemical Rubber, Cleveland, 1973).
- ¹³J.G. Eden and R.W. Waynant, Opt. Lett. **2**, 13 (1978); J. Chem. Phys. **68**, 2850 (1978); J.G. Eden, R.W. Waynant, S.K. Searles, and R. Burnham, Appl. Phys. Lett. **32**, 733 (1978).
- ¹⁴N. Djeu and C. Mazza, Chem. Phys. Lett. **46**, 172 (1977).

Quantum Electronics Letters

Spontaneous Emission Lifetime of the $C \rightarrow A$ Band of the XeF Molecule

R. W. WAYNANT AND J. G. EDEN

Abstract—The radiative lifetime of the blue $C \rightarrow A$ transition of XeF has been measured to be 93 ± 5 ns by monitoring the exponentially decaying 460 nm emission following rapid electron impact dissociation of XeF₂. By varying the XeF₂ partial pressure, the rate constant for quenching of XeF (C) by XeF₂ was determined to be $(1.8 \pm 0.5) \cdot 10^{-10} \text{ cm}^3 \text{ s}^{-1}$. Finally, knowledge of the XeF B and C state lifetimes yields a revised value of $610 \pm 60 \text{ cm}^{-1}$ for the B to C state energy defect.

THE existence of a "broad, smooth continuum in XeF centered near 450 nm," [1] first reported in 1975, has received little attention due to the band's low intensity and to the uncertainty of its identity. Recently, however, this continuum was shown to originate from the C state [2] of XeF [3] and, although theoretical calculations suggest that the B and C states are adjacent to one another in energy and intersect at small internuclear radii [4], the experimental results of Kligler and co-workers [5] and Brashears and Setser [6] show that the C state (presumably at its equilibrium radius R_e) lies $\sim 700 \text{ cm}^{-1}$ below the B level.

Several XeF laser experiments conducted in the last year have suggested that the proximity of the B and C states in energy may have a profound effect on the laser's efficiency due to coupling of the molecular levels by thermal gas collisions. The pronounced improvement of the XeF (350 nm) laser output energy that has been observed [7] when the laser gas medium was heated to 150–200°C ($kT \sim 300 \text{ cm}^{-1}$) raises the interesting possibility that the XeF (C) state may be acting as an energy reservoir to feed the lasing $B \rightarrow X$ transition. The imperative then, as several investigators have noted [5], [6], of including the C state in future modeling calculations underscores the necessity of determining the C state lifetime. Since only estimates were previously available, this letter will describe the measurement of the XeF ($C \rightarrow A$) radiative lifetime which has been found to be 93 ± 5 ns.

A partial energy level diagram for the XeF molecule is shown in Fig. 1. Although the potential curves are basically those given by Dunning and Hay [4]: 1) the X state has been

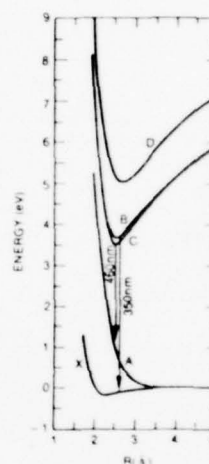


Fig. 1. Partial energy level diagram of XeF schematically showing the $C \rightarrow A$ (blue) and $B \rightarrow X$ (ultraviolet) bands (after Dunning and Hay; see [4] and text).

modified to reflect the $\sim 1200 \text{ cm}^{-1}$ binding and the equilibrium radius ($R_e \approx 2.2 \text{ Å}$) experimentally determined by Smith and Kobrinsky [8]; 2) the energy defect between the B and C states has been adjusted to conform to [5], [6]; and 3) R_e for the B state has been set at 2.5 Å [8]. As shown in the figure, the $B \rightarrow X$ transition of XeF is responsible for the well-known structured band in the ultraviolet at 350 nm. The importance of this band as a high energy laser transition prompted the recent measurements [9]–[11] of the XeF ($B \rightarrow X$) radiative lifetime.

For the experiments described below, dissociative excitation of XeF₂ by electron impact was used to populate the XeF (C) state and subsequently determine the $C \rightarrow A$ lifetime. Pulsed ultraviolet photolysis [11] of XeF₂ creates too few C state molecules for reliable spontaneous emission measurements to be made. Also, the narrow [~ 3 ns full width at half maximum (FWHM)] electron beam excitation pulse used in these experiments allows the C state lifetime to be accurately determined.

Manuscript received August 30, 1978; revised October 11, 1978. This work was supported by the Defense Advanced Research Projects Agency (DARPA).

The authors are with the Naval Research Laboratory, Washington, DC 20375.

U.S. Government work not protected by U.S. copyright

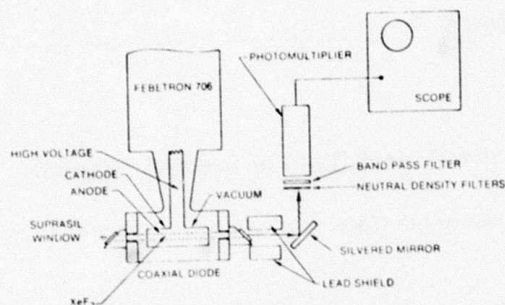
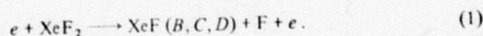
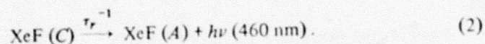


Fig. 2. Schematic diagram of the experimental apparatus used in measuring the XeF ($C \rightarrow A$) radiative lifetime.

The experimental apparatus is shown schematically in Fig. 2. A 600 kV, 3 ns FWHM voltage pulse was applied to a coaxial diode by a Febetron 706 generator. Electrons emitted from the cathode penetrated the cylindrical anode (aluminum tubing: 25 μ m wall thickness, 9 mm diameter, and ~25 cm length) which contained ~0.1–0.5 torr of XeF₂. Upon entering the interior of the anode, the electrons dissociatively excited the XeF₂, forming a variety of XeF excited molecules:



Limiting our attention to the C state, XeF (C) molecules subsequently radiate in the vicinity of 460 nm. Therefore



Since the C state is populated in a period of time that is short compared to its estimated lifetime, then τ_r may be determined by simply observing the exponential decay of the C state molecular population. This decay is, of course, reflected in the temporal behavior of the $C \rightarrow A$ emission which was detected by an EMI 9818 QB photomultiplier. To minimize the background noise reaching the detector, a silvered mirror was used to deflect the XeF* fluorescence into the phototube. Also, lead shielding was situated around the electron diode and detector. A blue bandpass filter ($T_{\text{max}} = 35$ percent at $\lambda_0 = 462$ nm, $\Delta\lambda = 50$ nm) selected the desired spectral region and neutral density filters attenuated the signal to avoid saturation of the photomultiplier. The XeF ($C \rightarrow A$) spontaneous emission waveforms were displayed on an oscilloscope, manually digitized, and then plotted on semi-log scales by a computer. Since each fluorescence waveform decayed exponentially over roughly two orders of magnitude, the exponential decay constant τ could be accurately measured for a particular XeF₂ concentration. By determining τ for several XeF₂ pressures in the range 0.1–0.5 torr, Fig. 3 was obtained which presents the dependence of τ on XeF₂ vapor pressure.

A simple rate equation analysis of processes by which C state molecules are destroyed reveals that

$$\tau^{-1} = \tau_r^{-1} + k_Q [\text{XeF}_2] \quad (3)$$

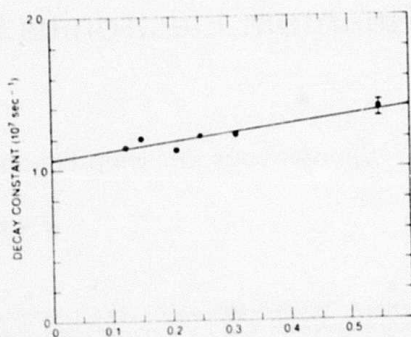


Fig. 3. Dependence of the exponential decay constant, τ , on the XeF₂ vapor pressure. The zero pressure intercept of the least squares fitting to the data (—) gives the XeF ($C \rightarrow A$) lifetime as 93 ns. Also, the slope of the solid line yields $k_Q = 1.8 \cdot 10^{-10} \text{ cm}^3 \cdot \text{s}^{-1}$. The one error bar shown typifies the estimated uncertainty of ~3 percent per data point.

where τ_r is the $C \rightarrow A$ radiative lifetime, $[\]$ denote particle densities (in units of cm^{-3}) and k_Q is the rate constant for quenching of XeF (C) state molecules by XeF₂. From the least squares fitting of the data of Fig. 3 (denoted by the solid line), $\tau_r = 93 \pm 5$ ns and $k_Q = (1.8 \pm 0.5) \cdot 10^{-10} \text{ cm}^3 \cdot \text{s}^{-1}$. This value for the radiative lifetime is in good agreement with that measured recently by Center (80 ns) [12] and the theoretical value of 113 ns given by Dunning and Hay [4].

As mentioned previously, low XeF₂ pressures were used in these experiments and buffer gas was avoided to minimize collisional coupling of the XeF B and C states. As a result, however, the XeF (C) state is not vibrationally equilibrated and therefore the radiative lifetime of 93 ns likely represents contributions from several C state vibrational levels.

Kligler and co-workers [5] have recently estimated the energy separation between the XeF C and B levels by comparing the relative intensities of the e -beam excited $B \rightarrow X$ and $C \rightarrow A$ transitions at high pressure. The defect that they calculate, $700 \pm 70 \text{ cm}^{-1}$, assumes 1) collisional equilibrium between the C and B states and 2) $(\tau_{B \rightarrow X}/\tau_{C \rightarrow A}) \approx (1/10)$. Using the $B \rightarrow X$ lifetime of 14.2 ns [11] and the $C \rightarrow A$ value presented above, then $(\tau_{B \rightarrow X}/\tau_{C \rightarrow A}) \approx (1/6.5)$ and so $\Delta E (B - C) = 610 \pm 60 \text{ cm}^{-1} = 0.076 \pm 0.007 \text{ eV}$ which is in excellent agreement with the separation of 0.08 eV measured by Brashears and Setser [6].

As mentioned earlier, the ~600 cm^{-1} defect between the C and B states may make the relatively long lived (~90 ns) C state ideal as an energy storage level. If the XeF laser gas mixture is heated to ~200°C, then during lasing the close collisional coupling between the C and B states will drive the mixing reactions toward the depleted B state (example: $\text{XeF} (B) + \text{Xe} \rightleftharpoons \text{XeF} (C) + \text{Xe} + 600 \text{ cm}^{-1}$), thus feeding the lasing $B \rightarrow X$ transition. More complete studies of the collisional properties of the C state will be required to assess the role of this level as an energy reservoir for the XeF UV laser and possibly other rare-gas halide molecules.

ACKNOWLEDGMENT

The authors are grateful for the technical assistance of D. Epp and interesting discussions with R. Burnham, L. Champagne, and J. Hsia.

REFERENCES

- [1] C. A. Brau and J. J. Ewing, "Emission spectra of XeBr, XeCl, XeF and KrF," *J. Chem. Phys.*, vol. 63, pp. 4640-4647, 1975.
- [2] Throughout this letter, the conventional X, A, B, ... etc., molecular nomenclature will be used (rather than the Roman numeral notation suggested in [4]) to denote the electronic states XeF. Although the B and C state labels probably should be interchanged due to their relative energies (see [5] and [6]) to avoid confusion we adopt the usual practice of referring to the upper level of the 350 nm laser band as the B state and the level from which the 460 nm continuum originates as the C state.
- [3] C. H. Fisher and R. E. Center, "Radiative lifetime and quenching kinetics for the XeF (B $\frac{1}{2}$) state," presented at the 30th Gaseous Electronics Conf., Palo Alto, CA, Oct. 1977, Paper AA 6.
- [4] T. H. Dunning, Jr., and P. J. Hay, "The covalent and ionic states of the rare gas monofluorides," *J. Chem. Phys.*, vol. 69, pp. 134-149, 1978.
- [5] D. Khgler, H. H. Nakano, D. L. Huestis, W. K. Bischel, R. M. Hill, and C. K. Rhodes, "Energy ordering of the excited states of XeF," *Appl. Phys. Lett.*, vol. 33, pp. 39-41, 1978.
- [6] H. C. Brashears, Jr., and D. W. Setser, "Transfer and quenching rate constants for XeF (III, 1/2) and XeF (II, 3/2)," *Appl. Phys. Lett.*, vol. 33, pp. 821-823, 1978.
- [7] J. Hsia, J. Mangano, J. H. Jacob, and M. Rokni, "Improvement in XeF laser efficiency at elevated temperatures," *Appl. Phys. Lett.*, to be published; L. F. Champagne, private communication.
- [8] A. L. Smith and P. C. Koblinsky, "Flash photolysis absorption spectroscopy of xenon fluoride," *J. Mol. Spectrosc.*, vol. 69, pp. 1-10, 1978.
- [9] J. G. Eden and S. K. Searles, "XeF* (C $\frac{1}{2}$) radiative lifetime measurement," *Appl. Phys. Lett.*, vol. 30, pp. 287-290, 1977. Early in the development of the XeF laser, the upper level for the 350 nm band was referred to as the C state. See also [10].
- [10] R. Burnham and N. W. Harris, "Radiative lifetime of the C state of XeF," *J. Chem. Phys.*, vol. 66, pp. 2742-2743, 1977.
- [11] J. G. Eden and R. W. Waynant, "Lifetime and collisional quenching measurements of XeF* (B) by photolysis of XeF₂," *Opt. Lett.*, vol. 2, pp. 13-15, 1978.
- [12] R. E. Center, private communication.

HgBr and HgI B STATE
QUENCHING RATE CONSTANTS[†]

J. G. Eden and R. W. Waynant
Naval Research Laboratory
Washington, D. C. 20375

ABSTRACT

The rate constants for quenching of the B states of HgBr and HgI by the rare gases and simple halogenated molecules have been measured. The experimental approach consisted of photodissociating either HgBr₂ or HgI₂ (in the presence of the desired quenching gas) and recording the subsequent radiative decay of the HgX (X=Br or I) excited state population. The large rate constant determined for two body destruction of HgBr (B) by Hg ($1.3 \cdot 10^{-10} \text{ cm}^3 \text{-sec}^{-1}$) and bromine donors (Br₂: $5.5 \cdot 10^{-10} \text{ cm}^3 \text{-sec}^{-1}$) enhances the attractiveness of HgBr lasers pumped by dissociative excitation of HgBr₂.

[†]Supported in part by the Defense Advanced Research Projects Agency (DARPA).

Due to the analogous chemical and optical properties of the mercury-halide and rare-gas halide molecules, visible lasing from the HgX ($\text{X}=\text{Cl}$, Br and I) B state molecules has been sought and demonstrated for a variety of excitation schemes.¹⁻⁴ However, several problems encountered with chemical HgX lasers (i.e., pumping of Hg /rare gas/halogen donor mixtures), such as pre-reaction of the mercury and halogen donor, thus far have severely restricted the performance of these systems. As a result, the closed cycle operation of these lasers, which has been shown to be feasible by electrical dissociation³ or photodissociation⁴ of the HgX_2 salts, is particularly attractive from the standpoint of long term laser reliability.

Although the radiative lifetimes of the HgCl ,^{4b,5} HgBr ⁶ and HgI ⁶ B \rightarrow X bands have been determined, few collisional quenching rates for gases of interest to mercury-halide laser designers are known. This paper summarizes the rate constants for quenching of the B states of HgBr and HgI (by the rare gases and simple halogenated molecules) that have been measured using rapid (~ 3 ns) photodissociation of HgBr_2 or HgI_2 . A prominent aspect of this experimental technique is that the desired excited state molecular population is created in a period of time that is short compared to the radiative lifetime. Therefore, the collisional destruction rates can be measured (without interference from competing collisional processes) by simply recording the exponential, radiative decay of the B state population in the

presence of the desired quenching gas. Such an experiment greatly simplifies the data interpretation and has been used previously to determine radiative lifetimes and collisional rate constants for the XeF (B) and KrF (B) excited complexes.⁷

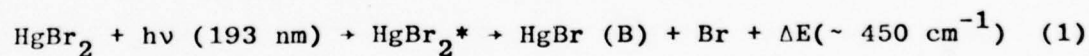
Several investigators⁸ have shown, through UV absorption and photolysis experiments, that the wavelength thresholds for photodissociative production of HgBr (B) and HgI (B) molecules from HgBr₂ and HgI₂ are $\lambda \sim 195\text{--}200$ and 230 nm, respectively. For this reason, the experimental approach of photolyzing HgBr₂ with pulsed ArF (193 nm) spontaneous emission and HgI₂ with KrCl (222 nm) fluorescence was employed in these experiments to optically produce the desired HgX (B) state population. The ArF and KrCl spontaneous emission, were generated by exciting rare gas halogen mixtures (Ne/Ar/F₂, 200:40:1, $p_{\text{TOTAL}} \sim 2000$ Torr for ArF⁹ or Ar/Kr/Cl₂, 200:20:1, same total pressure for KrCl) with an intense beam of 600 keV electrons from a Febetron 706 generator terminated in a coaxial diode of $\sim 60 \Omega$ impedance. Radial pumping of the gas mixtures produced intense rare gas-halide exciplex emission which could be monitored at one end of the cylindrical diode by a photodiode or photomultiplier. Emission from the other end of the diode was directed into a heated

quartz absorption tube. Separate cells were constructed for the HgBr and HgI experiments and into each was distilled several mg of the appropriate mercury-halide salt. The quartz cell, which was of 15 cm length and ~ 2 cm .

diameter, was connected to a vacuum and gas handling system by 6.3 mm diameter Teflon tubing. A Teflon valve was inserted in the vacuum line to facilitate changing the quenching gas pressure in the absorption cell. A thermometer monitored the temperature of the cell and the HgX_2 concentration was inferred from the vapor pressure equations.¹⁰

All of the rare gases used in the experiments were of research purity. The halogen-bearing gases F_2 , Cl_2 , CH_3Br , HBr , HI and CF_3I were all of technical grade and were used directly from the cylinder without further purification. The liquids CCl_2Br_2 and Br_2 were contained in a quartz reservoir and degassed by dry ice cooling and continuous pumping.

Upon absorbing a 193 nm photon, a HgBr_2 molecule is excited to an unstable electronic state, HgBr_2^* , which dissociates in ≤ 1 ns,^{4b} leaving a HgBr (B) molecule and a bromine atom as fragments:^{4a,8}



where $kT \sim 230 \text{ cm}^{-1}$ at 388°K and ω_e for the HgBr (B) state is 135 cm^{-1} (see ref. 11). Since the pump pulse width (3-5 ns) is considerably shorter than the HgBr (B+X) radiative lifetime, (24 ns)⁶, then the HgBr B state population decays exponentially with a decay constant, τ , given by:

$$\tau^{-1} = \tau_r^{-1} + k_Q[\text{Q}] \quad (2)$$

where τ_r is the HgBr radiative lifetime and k_Q is the rate constant for destruction of HgBr (B) in two body collisions with the

background gas, Q. So measuring τ^{-1} for various values of $[Q]$ allows τ_r and k_Q to be determined. A similar analysis holds for photolysis of HgI_2 by KrCl 222 nm emission.

For all the quenchers studied except Hg, the HgX_2 concentration was held at $[\text{HgBr}_2] \approx 6 \cdot 10^{14} \text{ cm}^{-3}$ and $[\text{HgI}_2] \approx 2 \cdot 10^{15} \text{ cm}^{-3}$ by maintaining the temperature of the quartz tubes at 351°K and 388°K, respectively. Keeping $[\text{HgX}_2] < 10^{16} \text{ cm}^{-3}$ allowed the quenching of $\text{HgX}(\text{B})$ molecules by the HgX_2 salt to be neglected in eqn. (2). The exponential decay rate τ was then measured for various quencher pressures in the absorption cell.

In order to measure the rate constants for quenching of HgBr^* and HgI^* by Hg, two additional quartz cells that were sealed-off and contained several mg of HgBr_2 or HgI_2 and ~ 30 mg of Hg were prepared. Each tube was evacuated to $< 10^{-5}$ Torr and baked thoroughly before being filled and sealed. For these experiments, the cell temperature was varied which, of course, changed both the Hg and HgX_2 vapor pressures. Therefore, an additional quenching term, $k_{\text{HgX}_2} [\text{HgX}_2]$ must be added to the right hand side of eqn. (2) where k_{HgX_2} has been measured previously.⁶ So, after measuring τ at various temperatures and correcting for quenching by HgX_2 , k_{Hg} could be determined. As a result of this technique, the Hg quenching rates could be measured only if k_{Hg} was larger than or comparable to k_{HgX_2} . Otherwise, an upper limit for k_{Hg} was inferred from the data.

Data acquisition consisted of recording HgX (B+X) sidelight waveforms on an oscilloscope. No fluorescence was observed either when the oven containing the quartz cell was at room temperature or when the coaxial diode was evacuated. The spectral regions of interest were isolated by bandpass filters ($\lambda_0 = 517$ nm, $\Delta\lambda = 17.5$ nm for HgBr; $\lambda_0 = 450$ nm, $\Delta\lambda = 16$ nm for HgI) and neutral density filters prevented saturation of the detector.

Examples of the exponentially decaying waveforms obtained in these experiments are shown in Fig. 1. Part (a) is an illustration of a typical HgI (B+X) signal observed after photodissociation of HgI₂. The emission waveforms were manually digitized and then plotted by a computer. Some visual averaging of the waveform occurred during the digitization process as shown in Fig. 1(b) which compares the KrCl (222 nm) excitation pulse (viewed by a photomultiplier and 221 ± 24 nm bandpass

filter) with the relatively long-lived HgI^* fluorescence. From the falling portion of the waveform, τ was determined and subsequently corrected for the non-zero optical pump pulse width and for the response of the detection system.

The dependence of τ on mercury concentration for HgBr is shown in Fig. 2 where the solid line represents the linear least-squares fitting to the data. The data have already been corrected for quenching of the B state by HgBr_2 and so the slope of the line represents the rate constant for quenching of HgBr (B) by Hg which was found to be $(1.3 \pm 0.5) \cdot 10^{-10} \text{ cm}^3\text{-sec}^{-1}$. Further details of the experimental technique and data analysis are to be found in previous papers.^{4b,6}

Table I summarizes the HgBr (B) state quenching rate constants that have been measured. The quenchers selected for study were chosen due to their present or contemplated future use in electron beam or discharge pumped HgBr lasers. For example, N_2 was investigated due to its dramatic effect on the pulse energy of HgBr self-sustained discharges.^{3a} The results of Table I reveal that, for even 100 Torr of N_2 in the discharge (the highest pressure reported by Burnham^{3a}), the nitrogen quenching rate is $\sim 1.4 \cdot 10^7 \text{ sec}^{-1}$ or roughly 1/3 of the radiative rate. Thus, although N_2 is apparently effective in depopulating the lower laser level, it quenches the upper state slowly. Similarly, CCl_2Br_2 was studied since it has been found^{2a} to

be the best donor for c-beam sustained discharge operation of the HgBr laser. Despite the size of the molecule, its quenching rate constant is only roughly twice that measured for HBr.

Little data is available in the literature with which the results of Table I may be compared. Recently, however, Tang and co-workers⁵ measured the quenching rates of HgCl (B) by Cl₂ and Ar. Comparing their Ar rate constant with the rare gas rates reported here, it is evident that the HgX molecules are not rapidly quenched by the rare gases. This is not surprising since, unlike the rare gas halide molecules, no spectroscopic evidence exists for a HgX excited state lying beneath the B level. The large energy defect between the B and X (ground) states discourages quenching of HgX (B) by atoms. Also, attempts were made at finding second-order least squares solutions to the τ versus [Q] data. However, for most of the quenchers studied, the quadratic coefficients were found to be negative and are, therefore, physically unacceptable. The only three-body quenching rate determined in these experiments was for HgBr (B) destroyed by two Ar atoms and the rate constant was found to be $1.8 \cdot 10^{-32}$ cm⁶-sec⁻¹. This is also consistent with the large B to X energy separation and the relatively small two-body rate constants.

In this regard, the rate constant for HgBr quenching by Hg is unusually large and not consistent with its electronic polarizability or physical size as compared to the rare gases.

In fact, the Hg rate constant is similar to those measured for the polyatomic molecules. Considering this along with the precipitous decrease in HgBr (B+X) fluorescence observed by Whitney¹² in e-beam sustained Ar/Hg/CCl₂Br₂ mixtures for [Hg] > 4 · 10¹⁶ cm⁻³ suggests the possible existence of a mercury halide triatomic complex:



where the excess energy may be absorbed by internal modes of freedom of the molecule. Although no emission from this molecule has been reported, this trimer may be partially responsible for the aerosol that has been observed following discharge excitation of Hg/Ar/CCl₂Br₂ or Cl₂ gas mixtures.^{2a} Since the large Hg quenching rate constant and the aerosol phenomenon are avoided in the HgX₂ dissociation lasers, then several engineering design problems are ameliorated. So, for many applications and particularly those where sealed-off operation and non-corrosive laser fuels are desirable, the HgX₂ dissociation lasers are preferable to the chemical systems.

The quenching rate constants that have been measured for the HgI (B) state are given in Table II. It was only possible to determine an upper limit for k_{HgI} of 3 · 10⁻¹¹ cm³-sec⁻¹ due to the dominance of HgI₂ quenching. One significant aspect of these rate constants is that the HgI (B) values are significantly smaller than the analogous constants for the bromide. This may simply be due to the larger B-X energy gap for HgI as opposed to that for HgBr.

In summary, the rate constants for quenching of the B states of HgBr and HgI by various gases have been measured by photodissociating HgBr₂ and HgI₂ and monitoring the real time decay of the B state population. These constants fill a void in our knowledge of the collisional behavior of the HgX (B) species and are essential to computer modelling of the mercury halide lasers, regardless of the excitation mechanism used.

The authors are grateful to Dan Epp for excellent technical assistance.

REFERENCES

1. Electron beam pumping: a) J. H. Parks, Appl. Phys. Lett. 31, 192 (1977); 31, 297 (1977); b) J. G. Eden, Appl. Phys. Lett. 31, 448 (1977).
2. E-beam sustained discharge excitation: a) W. T. Whitney, Appl. Phys. Lett. 32, 239 (1978); b) K. Y. Tang, R. O. Hunter, Jr., J. Oldenettel, C. Howton, D. Huestis, D. Eckstrom, B. Perry and M. McCusker, Appl. Phys. Lett. 32, 226 (1978).
3. Self-sustained discharge excitation: a) R. Burnham, Appl. Phys. Lett. 33, 156 (1978); b) E. J. Schimitschek and J. E. Celto, Opt. Lett. 2, 64 (1978).
4. Optical pumping: a) E. J. Schimitschek, J. E. Celto and J. A. Trias, Appl. Phys. Lett. 31, 608 (1977); b) J. G. Eden, Appl. Phys. Lett. 33, 495 (1978).
5. K. Y. Tang, R. O. Hunter, Jr., J. Oldenettel and D. L. Huestis, J. Chem. Phys. (accepted for publication).
6. R. W. Waynant and J. G. Eden, Appl. Phys. Lett. 33, 708 (1978).
7. J. G. Eden and R. W. Waynant, J. Chem. Phys. 68, 2850 (1978); J. G. Eden, R. W. Waynant, S. K. Searles and R. Burnham, Appl. Phys. Lett. 32, 733 (1978).
8. J. Maya, J. Chem. Phys. 67, 4976 (1977) and references quoted therein.
9. J. R. Murray and H. T. Powell in Electronic Transition Lasers II, L. E. Wilson, S. N. Suchard and J. I. Steinfeld, eds., MIT Press, Cambridge, MA (1977).

10. Handbook of Chemistry and Physics, R. Weast, ed.,
Chemical Rubber Co. Press, Cleveland, OH (1973).
11. G. Herzberg, Molecular Spectra and Molecular Structure:
I. Spectra of Diatomic Molecules, Van Nostrand Reinhold
Co., New York, NY (1950), p. 537.
12. W. T. Whitney, paper U.9, 10th Int. Quantum Elect. Conf.,
Atlanta, GA (June, 1978).
13. E. J. Schimitschek and J. E. Celto, Opt. Lett. 2, 64 (1978).

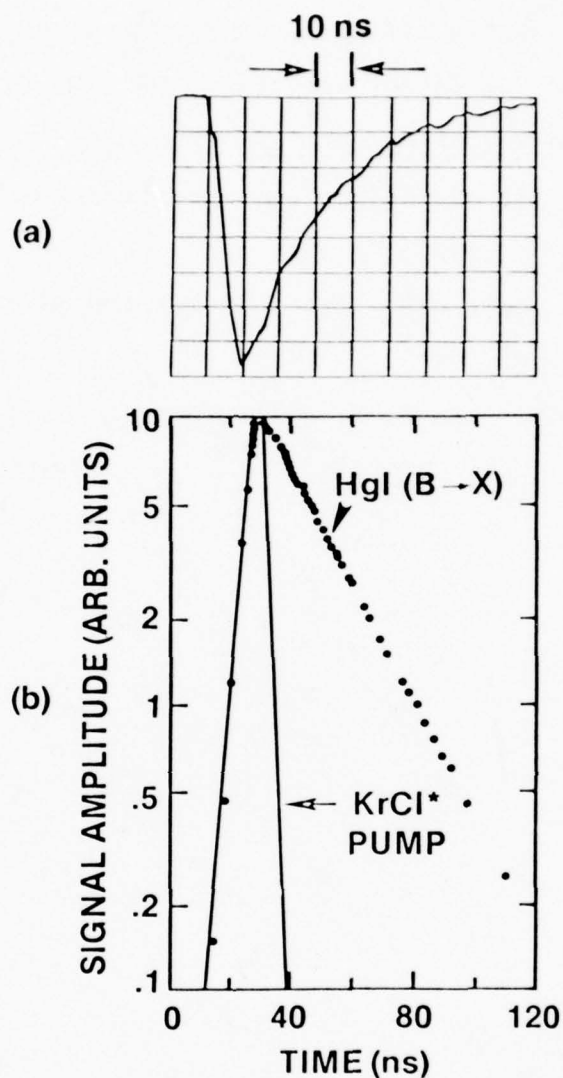


Figure 1. Typical waveforms obtained during HgX_2 photolysis experiments: a) oscillogram of $\text{HgI (B} \rightarrow \text{X)}$ spontaneous emission from $^a\text{HgI}_2$ and N_2 mixture in the quartz cell and b) semi-log plot of the KrCl (222 nm) pump and HgI^* fluorescence waveforms - $[\text{HgI}_2] = 2.3 \cdot 10^{15} \text{ cm}^{-3}$, $\text{N}_2 \approx 1.5 \cdot 10^{19} \text{ cm}^{-3}$ and $T = 388^\circ\text{K}$.

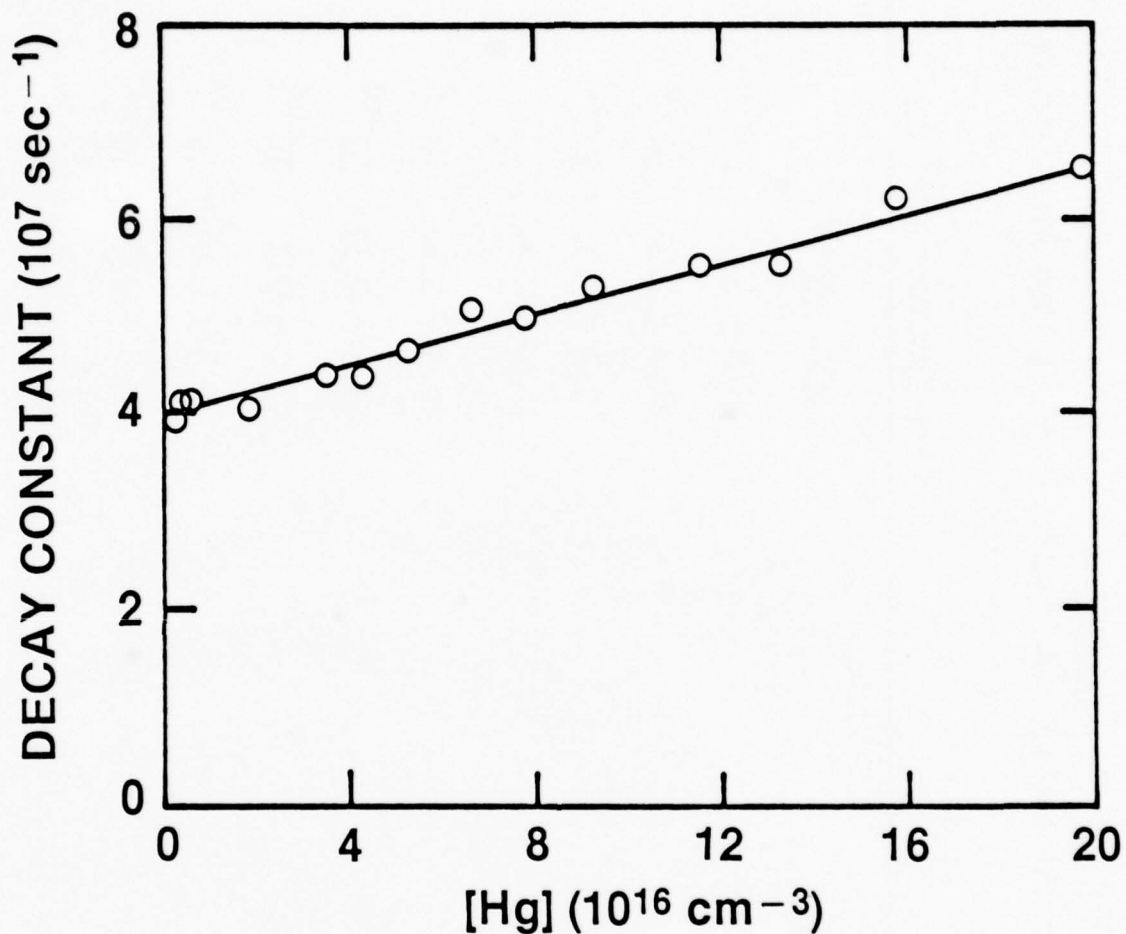


Figure 2. Dependence of the exponential decay constant on the mercury concentration for HgBr. The slope of the linear least squares fit to the data (represented by the solid line) defines the rate constant for quenching of HgBr, (B) by Hg as $1.3 \cdot 10^{-10} \text{ cm}^3\text{-sec}^{-1}$. The data shown have already been corrected for HgBr₂ quenching.

TABLE I
RATE CONSTANTS FOR QUENCHING OF HgBr (B) MOLECULES BY VARIOUS ATOMS AND MOLECULES

QUENCHER	RATE CONSTANT ($\text{CM}^3\text{-SEC}^{-1}$)
HE	$< 5 \cdot 10^{-13}$
NE	$(5.3 \pm 1.8) \cdot 10^{-13}$
AR	$(7.4 \pm 1.5) \cdot 10^{-13}$
XE	$(3.7 \pm 0.3) \cdot 10^{-12}$
HG	$(1.3 \pm 0.5) \cdot 10^{-10}$
N ₂	$(4.4 \pm 0.5) \cdot 10^{-12}$
BR ₂	$(5.5 \pm 0.3) \cdot 10^{-10}$
HBR	$(2.0 \pm 0.4) \cdot 10^{-10}$
CH ₃ BR	$(3.9 \pm 0.4) \cdot 10^{-10}$
CCl ₂ BR ₂	$(4.3 \pm 0.4) \cdot 10^{-10}$
HGBR ₂	$(1.7 \pm 0.3) \cdot 10^{-10}$

TABLE II
QUENCHING RATE CONSTANTS FOR THE B STATE OF HgI

QUENCHER	RATE CONSTANTS ($\text{CM}^3\text{-SEC}^{-1}$)
AR	$(3.3 \pm 1.5) \cdot 10^{-13}$
XE	$(7.1 \pm 0.8) \cdot 10^{-13}$
N ₂	$(1.1 \pm 0.2) \cdot 10^{-12}$
HI	$(1.0 \pm 0.2) \cdot 10^{-10}$
CF ₃ I	$(2.9 \pm 0.3) \cdot 10^{-10}$
Hg	$2.3 \cdot 10^{-11}$
HgI ₂	$(3.6 \pm 0.3) \cdot 10^{-10}$

LONG-PULSE KINETICS EXPERIMENTS

1. Apparatus

An apparatus was built to enable the study of energy flow kinetics in typical e-beam-pumped RGH gas mixtures under laser conditions. This device allows the observation of sidelight fluorescence of selected radiating species in the laser plasma. A schematic diagram of the long-pulse kinetics apparatus is shown in Fig. 1. A gas mixture of up to 7 atm pressure is pumped for $\sim 1 \mu\text{sec}$ by a 300 keV, 2 A/cm^2 , 20 cm x 1 cm electron beam. Spectrally resolved side fluorescence is observed with filter-photodiode combinations; beam splitters are used to observe two or more wavelength bands simultaneously. Laser mirrors may be added to observe the effects of laser saturation on side emission.

The apparatus has been used to measure XeF (B) formation efficiency, XeF (B \rightarrow X) fluorescence efficiency for gas mixtures, and e-beam pump currents corresponding to optimum laser performance. Also, the XeF (B \rightarrow X) and XeF (C \rightarrow A) fluorescence emissions were measured under various conditions to assess the effect of C \rightarrow A emission on laser performance.

2. XeF (C) Investigations

An intense 400-500 nm broadband fluorescence in XeF laser mixtures had been seen by several investigators and was attributed to spontaneous C \rightarrow A emission of the XeF exciplex. Since the presence of the C-state with such strong emission could have significant effects on the formation of

the XeF (B) state and on the extraction of B→X laser emission, a program was initiated to assess the role of the XeF (C) state in the e-beam pumped XeF laser. Closely interacting experimental and numerical approaches were applied to the problem and the results were published¹ (see reprint which follows).

The experimental approach used the apparatus pictured in Fig. 2. It basically consisted of simultaneously measuring the relative intensities of B→X (351 nm) line emission and C→A (~ 460 nm) broadband emission from e-beam pumped Ne/Xe/NF₃ gas mixtures as a function of partial pressures of the various mixture components. A steady-state numerical model was developed and was used in conjunction with the time-dependent computer model to perform simulations in which various rates were adjusted to fit the observed variations of B and C fluorescence vs. pressure.

The important result derived from this study is that, for e-beam pumped XeF lasers, the C-state does not impose a major limitation on the B→X laser performance because ~ 80% of the direct excitation of XeF goes into the B state. Also, most of the C-state formation is by collisional mixing with the B state so that the observed excitation-energy loss through C→A fluorescence can be reduced by stimulating radiation on the B→X transition. Thus, the laser performance is most likely limited by incomplete upper-laser-level vibrational relaxation and by bottlenecking due to the weakly bound lower laser level.

Another conclusion derived from this work is that for pumping conditions studied here, electron mixing of the XeF B and C states is not important. This is supported by the data plotted in Fig. 2., which show that the ratio of B to C fluorescence changes very little when the NF₃

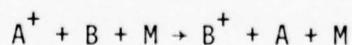
concentration is varied over two orders of magnitude. The equilibrium concentration of electrons is controlled by the density of the attaching species, NF_3 , and thus, it is seen that a large change in electron density has little effect on B-C mixing rates. More detail is discussed in the following reprint of the C-state paper.

3. Rare-gas Halide Laser Issues in Need of Further Study

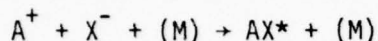
The experimental and numerical efforts at NRL during the past year have been aimed mainly at deriving a complete understanding of the laser/kinetics chain in rare-gas halide lasers. To completely define the operation and scaleup properties of a laser, one must know all of the relevant chemical kinetics rates, lifetimes, and cross sections involved in upper-laser-level formation, interception, quenching, and laser light absorption and extraction. Detailed studies of the energy-flow kinetics in the XeF laser (both e-beam-pumped and e-beam-controlled) have pointed out several important kinetic reactions and species which should be studied further to allow a better understanding of this and other rare-gas-halide lasers. The processes are discussed below.

a. Three-body charge transfer reactions

Most charge transfer collisions between two different rare gases have relatively small cross sections and are thus not important to the energy flow chain in RGH lasers. However, at multiatmosphere operation typical of KrF, XeF and XeCl lasers, three-body processes become important. Such reactions are of the type



where A and B are rare gases and M is any third body. Three-body charge transfer may compete with ion-ion recombination,



and could have significant effects on the upper-laser-level formation chain and on absorber concentrations. Since little is known about rate constants for three-body charge transfer reactions, it is recommended that experiments be performed to measure them for rare gas combinations used in RGH lasers.

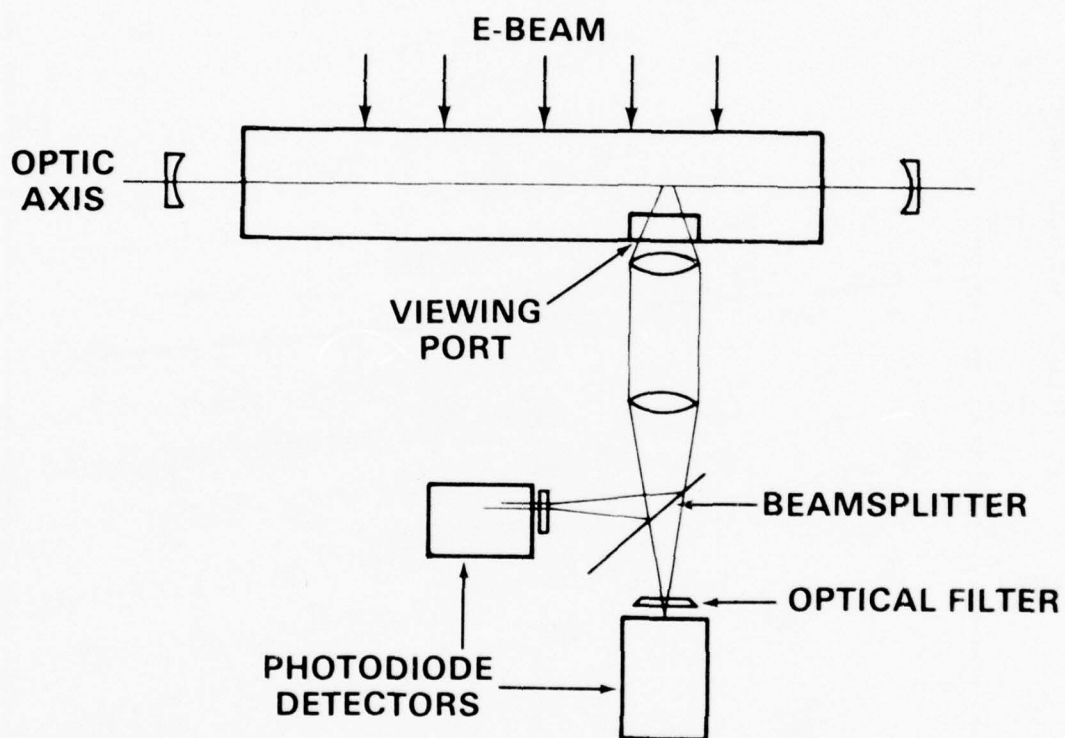
b. Complex ion properties

Heteronuclear rare gas excimers and ions can be important species especially in RGH laser mixtures in which the mole fraction of the diluent gas is greater than 99% as is the case for the XeF laser in Ne diluent. In this laser, the complex ion, NeXe^+ , may be an important species in the XeF formation chain depending on its rates of formation, recombination with F^- , and binding energy. A knowledge of relevant rates and molecular properties of NeXe^+ would be highly beneficial to understanding the XeF laser especially at high pumping currents where the ion channel dominates the formation chain. Hence, it is recommended that experimental and/or theoretical studies be directed at deriving the properties of this ion and of other heteronuclear rare-gas ions.

Reference

1. T. G. Finn, L. J. Palumbo, and L. F. Champagne, "The Role of the C State in the XeF Laser," Appl. Phys. Lett. 34(1) (1 January 1979).

KINETICS EXPERIMENT



ACTIVE VOLUME: $20\text{ cm} \times 1\text{ cm} \times 1\text{ cm}$

Figure 1. Schematic of long-pulse kinetics apparatus

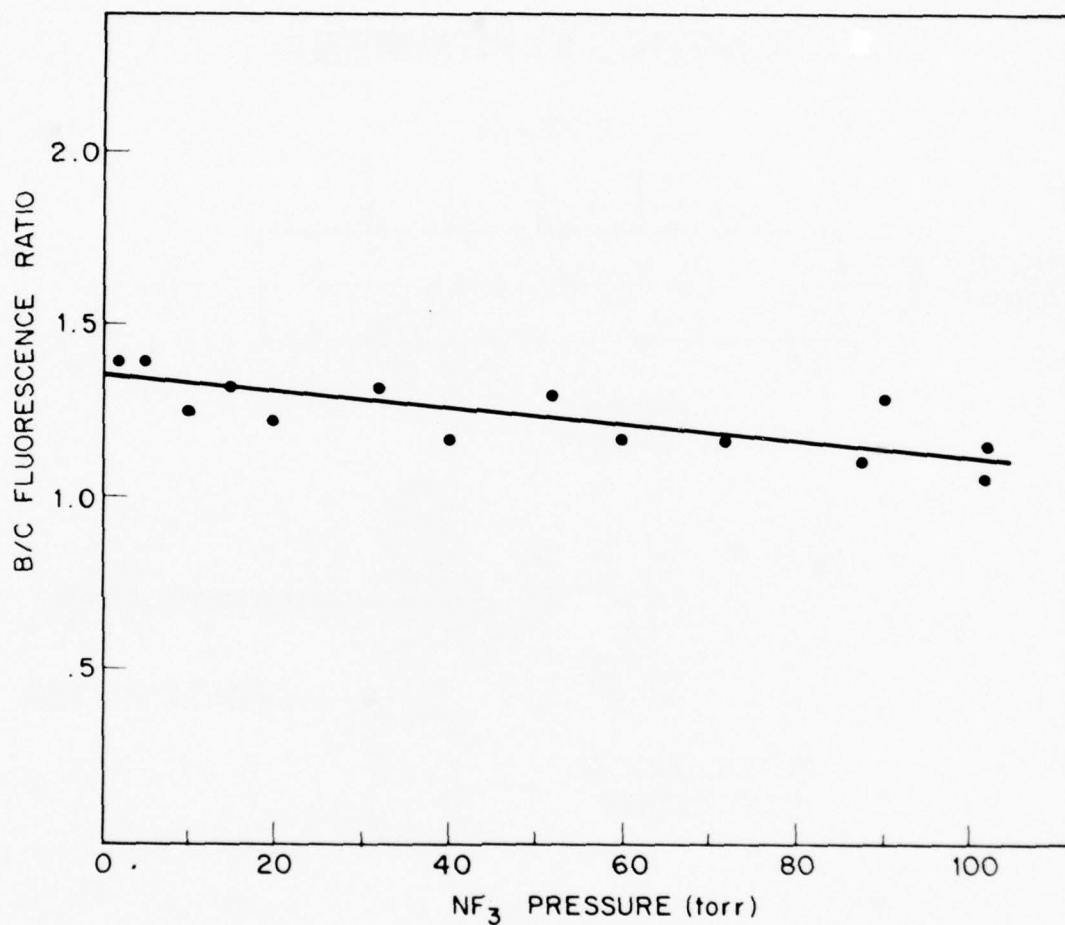


Figure 2. Ratio of XeF (B \rightarrow X) fluorescence to XeF (C \rightarrow A) fluorescence vs. NF_3 pressure.

The role of the C state in the XeF laser

T. G. Finn,^{a)} L. J. Palumbo, and L. F. Champagne

Laser Physics Branch, Optical Sciences Division, Naval Research Laboratory, Washington, D.C. 20375
(Received 12 October 1978; accepted for publication 31 October 1978)

Ne/Xe/NF₃ mixtures were irradiated by a cold-cathode e-beam, and the fluorescence yields of the *B* and *C* states of XeF were measured as a function of neon pressure from 200 to 5300 Torr. At low neon pressures, the fluorescence yield of the *B* state corresponds to one photon emitted for each neon ion formed. As the neon pressure is increased the fluorescence yield of the *B* state decreases, but the ratio of the *C* emission to *B* emission approaches unity. If the *C* is formed through a channel which is independent of the *B* state, then the ultimate efficiency of the XeF laser is severely limited. However, analysis of the data with a XeF kinetics model indicates that the enhanced *C* emission results from two-body quenching of the *B* state by neon. We conclude that the XeF laser performance has been limited by other processes, namely, incomplete vibrational relaxation and ground-state bottlenecking.

PACS numbers: 42.55.Hq, 82.20.Wt, 33.50.Dq

XeF is the second rare-gas monohalide laser system (after KrF) to demonstrate high efficiency and output power. Initially, the XeF laser was operated in an argon diluent, but its efficiency was well below 1% because of transient

absorption in the medium. Champagne and Harris found a significant improvement in the output power and efficiency with neon as the diluent.¹ This work showed that the transient absorption present in pure neon, although comparable to that in pure argon, was markedly reduced by the addition of a small amount of xenon. Previously, we developed a com-

^{a)}Science Applications, Inc., Arlington, Va. 22202.

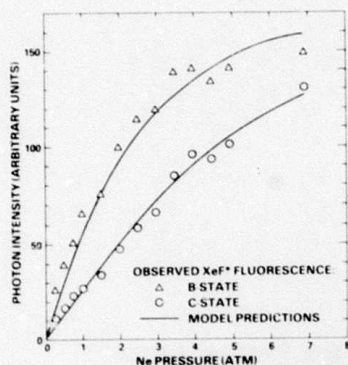


FIG. 1. Observed fluorescence of XeF B and C states with 6 Torr Xe and 2 Torr NF, as a function of neon pressure. The solid lines are the model calculations based on the formation efficiency and quenching rates given in the text.

puter model which simulates the kinetics in an electron beam-pumped XeF laser. Analysis with the model has shown that the addition of a small amount of xenon to pure neon significantly reduces the concentration of neutral species such as Ne^* and Ne_2^+ through the mechanisms of Penning and associative ionization, but only slightly diminishes the concentration of charged species.⁷ Consequently, we have attributed the transient absorption in pure neon to the neutral species.

XeF has two intense emission features, the $B \rightarrow X$ system around 351 nm and the broad $C \rightarrow A$ system centered around 460 nm. Our kinetic model predicts that the formation efficiency of XeF^* is high, but it cannot determine which states (B or C) are populated. Recently, Kligler *et al.*⁸ have shown that the C state of XeF lies 700 cm^{-1} below the B state, and that the emission intensity of both states are equal under pumping conditions similar to those in the laser. The importance of the latter result is the following: if the C state is formed in such a way that its excitation energy is not channeled through the B state, then almost one-half the total excitation is lost. Thus, the maximum efficiency of the XeF laser would be approximately 5%, which is the value recently obtained by heating the mixture.^{4,5} If, on the other hand, the C state is formed through the B state, then all the excitation present in the C state is potentially extractable as laser radiation. To resolve this question and to characterize further the XeF laser, we have investigated the fluorescence from the B and C states and analyzed the results with a computer model.

The apparatus used in these experiments has been described previously and will be reviewed briefly.⁹ The kinetics chamber is made from aluminum and has an active volume of $1.5 \times 1 \times 20 \text{ cm}^3$. The chamber is mounted directly to the electron-gun vacuum chamber with a thin titanium foil separating the two. The cold-cathode electron gun produces a beam of 280-keV electrons with a pulse duration of $\sim 1 \mu\text{sec}$. The peak current density into the laser gas is 2 A/cm^2 . Fluorescence is observed perpendicular or parallel to the elec-

tron-beam direction with calibrated photodiodes and filters. All the kinetics experiments used concentrations of 6 Torr Xe and 2 Torr NF, which are the values corresponding to the optimum laser mixture. The dominant kinetic processes have characteristic times which are much shorter than the pulse duration, thus the excited and ionic species are in quasiequilibrium.

In Fig. 1, the XeF ($B \rightarrow X$) and ($C \rightarrow A$) fluorescence from a mixture of Ne/Xe/NF is given as a function of neon pressure. At low neon pressure the ratio of $B \rightarrow X$ to $C \rightarrow A$ emission intensity is approximately 4 : 1. As the neon pressure increases, the fluorescence from both states increases, but at high pressures the $B \rightarrow X$ fluorescence begins to level off while the C fluorescence continues to rise. At the optimum laser mixture (5 atm) the $C \rightarrow A$ emission is over 70% of the $B \rightarrow X$ emission.

More information about the B and C states can be obtained by calculating their corresponding fluorescence yields. The fluorescence yield is defined here as the ratio of the number of photons emitted from a state divided by the number of ion-electron pairs produced by the electron beam. A fluorescence yield of unity corresponds to one photon emitted for each ion formed. It is possible for the total fluorescence yield to be greater than unity. For each 100 ions that are created, the electron beam also produces about 30 excited neutral atoms which can lead to the upper laser level.⁷

Relative fluorescence yields can be put on an absolute basis by normalizing to the absolute fluorescence yield of the N_2 second positive system produced in mixtures of argon with 5% nitrogen. At a total pressure of 2 atm, Huestis and Tang have determined the fluorescence yield of the second positive system to be approximately 9% over the e-beam current range $1\text{--}10 \text{ A/cm}^2$ incident to the active volume.⁸ Using the argon/nitrogen fluorescence as a secondary stan-

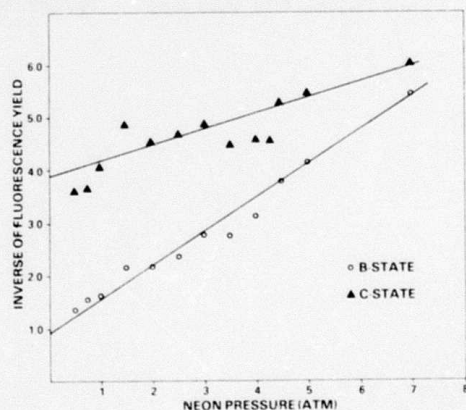


FIG. 2. Inverse of the fluorescence yields of the XeF ($B \rightarrow X$) and ($C \rightarrow A$) emissions as a function of neon pressure. For the B state the zero-pressure intercept of unity indicates that its formation efficiency is approximately one XeF (B) molecule for each neon ion formed.

TABLE I. Quenching rate constants used in model.

Quenching reaction	Rate constant	Branching ratio to XeF (C)	Reference
XeF (B) + Ne	7.7×10^{-11} cm ³ /sec	0.95	11 and 12
+ 2Ne	2.7×10^{-11} cm ³ /sec	0.5 ^a	13
+ Ne + Xe	8.3×10^{-11} cm ³ /sec	0.5 ^a	13
+ Xe	1.1×10^{-10} cm ³ /sec	0.45	12
+ NF ₃	8.4×10^{-11} cm ³ /sec	0.64	11 and 12
XeF (C) + Ne + Xe	4.0×10^{-11} cm ³ /sec	Products	This work

^aAssumed for model calculations.

dard, we obtained the absolute fluorescence yield of the XeF ($B \rightarrow X$) and ($C \rightarrow A$) transitions as a function of neon pressure. Since the thickness of the target gas is small compared to the penetration depth of the e-beam, the number of ions produced is linearly proportional to the gas pressure. Thus, the relative fluorescence yield is equal to the signal intensity divided by the neon pressure.

In Fig. 2 the inverse of the absolute fluorescence yield for the XeF transitions ($B \rightarrow X$) and ($C \rightarrow A$) is plotted versus neon pressure. This method of data analysis is similar to a Stern-Volmer plot and is useful in interpreting the data. Moreover, the fluorescence yields have been corrected to account for quenching by Xe and NF₃. This correction, which is largest in the low-pressure region, is about 10%. As can be seen in Fig. 2, at low neon pressure the fluorescence yield of the $B \rightarrow X$ transition approaches unity, which corresponds to a fluorescence energy efficiency of 10%. However, as the neon pressure is increased the fluorescence yield decreases, so that at the optimum laser mix of 5 atmospheres it is approximately 0.3. Meanwhile, the fluorescence yield of the $C \rightarrow A$ transition varies slowly and approaches 0.25 at zero pressure. There are two likely explanations for the pressure behavior of the fluorescence yields. First, at high pressure the formation efficiency of the B state is close to unity, but the state is quenched to the C state which lies 700 cm⁻¹ below it. Second, at high pressure, the excitation energy is intercepted before it reaches the B state and channeled directly into the C state. In the former case, almost all of the excitation can be considered as potential laser radiation because the energy can be extracted from the B state before it is quenched to the C state. However, in the latter case, the energy is directly pumped into the C state and is virtually inaccessible. Thus, the manner in which the C state is formed at high pressure determines the ultimate efficiency of the laser.

The C state can be formed in three ways: direct excitation, quenching from B to C by neutral species, and quenching from B to C by electrons. Our data indicates that electron mixing of the B and C states is not significant up to a pumping rate of 7 A/cm². This conclusion is based on the following results. First, as the NF₃ concentration in the kinetics chamber was varied from 2 to 100 Torr, we observed only a 10% decrease in the B/C emission ratio. Since the removal rate of the electrons, and thus their equilibrium concentration, is determined by the concentration of the attaching species, NF₃, the electron density varied greatly but the B -to- C

ratio remained approximately constant. Furthermore, other experiments were conducted in the laser mixture (5 atm) with 7-A/cm² e-beam pumping current, and the B -to- C ratio was found to be the same as in the kinetics experiments with 2-A/cm² pumping rate. Finally, if electron mixing were significant the B/C emission ratio should be much higher than is observed. The separation of the B and C states is 700 cm⁻¹, which is about 0.08 eV. If the electron temperature were 1 eV, the states would be approximately equally populated. Since the ratio of transition probabilities for the B and C states is approximately 7, the B -to- C emission ratio would be much greater than unity.⁷ Instead, the observed emission ratio extrapolates at high pressure to a value of 0.6, which corresponds to a temperature of 0.035 eV, close to the temperature of the background gas. Thus, electron mixing is not important in determining the ratio of the B and C states and a model based solely on neutral kinetics may be used.

The neutral kinetics model must include direct pumping to B and C , quenching from B to C and the reverse reactions, and quenching from B and C to products. For direct pumping the absolute fluorescence yields extrapolated to zero pressure were used. The quenching rate constants used in the model are given in Table I. The applicability of the rates will be discussed later. The predictions of the model based on absolute fluorescence yields and quenching by neutrals are given as the solid lines in Fig. 1. As can be seen from Fig. 1, the model is in good agreement with the data. Quenching of the B state, primarily through two-body collisions with neon, accounts for all the observed decrease in the fluorescence yield as the neon pressure is increased. If significant interception of the B state were present, the model values would be much higher than the observed B emission. Moreover, if at high pressure a larger fraction of the excitation were channeled directly into the C state, the model predictions for the C emission would be much less than the observed values. Initially, however, the predicted C emission was higher than the observed value, indicating that some quenching of the C state by the background gas occurs. The C -state quenching rate which fits the data is given in Table I.

Three important conclusions can immediately be drawn from the model analysis. First, almost 80% of the ions and electronically excited neutrals formed channel their excitation directly into the B state. Second, the back reaction, C to B , is small, such that once the energy is in the C state it is virtually lost. Third, the enhanced C emission at high pressure is due to quenching from B to C , primarily

through two-body collisions with neon. In fact, two-thirds of the *C* population results from the *B* state. The last conclusion has been verified experimentally. Since a large fraction of the *C*-state population results from the *B* state, the *C* emission rate will decrease if the steady-state *B* population is decreased as occurs in a saturating laser field. The depression of the *C* emission in a saturating laser field has been observed.¹⁰

The accuracy of the model predictions depends on the reliability of the rate constants used. Over 50% of the *B*-state quenching is due to two-body neon quenching, a process whose rate constant and branching are well characterized.^{11,12} However, 40% of the quenching is due to three-body neon and neon plus xenon reactions. The rate constants for these processes have been derived from electron-beam-pumped mixtures, and, strictly speaking, the rates could correspond to interception rather than quenching processes. That is, these reactions could channel excitation away from the *B* state rather than quench the *B* state. In order to characterize the XeF laser precisely the quenching rate constants and branching ratios for these processes have to be known.

Assuming the reliability of the quenching rate constants, we can summarize the results and conclusions:

(a) The formation efficiency of the *B* state is approximately one XeF (*B*) molecule formed for each ion pair created.

(b) The decrease in the *B*-state fluorescence yield observed at high pressure is due to quenching, primarily through two-body collisions with neon.

(c) The enhanced *C* emission observed at high pressure is due to quenching from *B* to *C* rather than interception of the *B* state.

(d) Since the formation efficiency of XeF (*B*) is high, other processes are limiting the laser performance. Most likely, these processes are incomplete vibrational relaxation and bottlenecking of the state due to finite relaxation rates.

The authors wish to thank W. T. Whitney for lending us his electron-beam apparatus, D. Shores for his technical assistance, and D. Huestis, SRI, and K. Tang, Maxwell Labs. Inc., for making available to us their unpublished data.

- ¹L. F. Champagne and N. W. Harris, *Appl. Phys. Lett.* **31**, 513 (1977).
- ²T. G. Finn, L. J. Palumbo, and L. F. Champagne, *Appl. Phys. Lett.* **33**, 148 (1978).
- ³D. Kligler, H. H. Nakano, D. L. Huestis, W. K. Bischel, R. M. Hill, and C. K. Rhodes, *Appl. Phys. Lett.* **3**, 39 (1978).
- ⁴L. F. Champagne (unpublished).
- ⁵J. Hsia, J. A. Mangano, J. H. Jacob, and M. Rokni, *Appl. Phys. Lett.* (to be published).
- ⁶N. W. Harris, F. O'Neill, and W. T. Whitney, *Appl. Phys. Lett.* **25**, 148 (1974).
- ⁷L. R. Peterson and J. E. Allen, Jr., *J. Chem. Phys.* **56**, 6068 (1972).
- ⁸D. L. Huestis, R. M. Hill, D. J. Eckstrom, M. V. McCusker, D. C. Lorents, H. H. Nakano, B. E. Perry, J. A. Margevicius, and N. E. Schlotter, Stanford Research Institute International Report No. MP 78-07, 1978 (unpublished).
- ⁹R. W. Waynant and J. G. Eden, *J. Quantum Electron.* (to be published).
- ¹⁰L. F. Champagne (unpublished).
- ¹¹J. G. Eden and R. W. Waynant, *Opt. Lett.* **2**, 13 (1978).
- ¹²H. C. Brashears, Jr. and D. W. Setser, *Appl. Phys. Lett.* **33**, 821 (1978).
- ¹³M. Rokni, J. H. Jacob, J. A. Mangano, and R. Brocher, *Appl. Phys. Lett.* **32**, 223 (1978).

A kinetics scheme for the XeF laser

T. G. Finn,^{a)} L. J. Palumbo, and L. F. Champagne

Laser Physics Branch, Optical Sciences Division, Naval Research Laboratory, Washington, D.C. 20375
(Received 20 March 1978; accepted for publication 5 May 1978)

A kinetics scheme is described for electron-beam excitation of the XeF laser in a neon diluent. Both Ne^+ and Ne^* channels contribute significantly to the formation of the upper laser level. In each chain an important Penning ionization process leads to the formation of Xe^+ , which is the major intermediary in forming the upper laser level. Xe_2^+ is found to be the dominant absorber of laser radiation. The effect of the weakly bound XeF ground state is discussed.

PACS numbers: 42.55.Hq, 82.20.Wt, 42.60.By

Since the first demonstration of exciplex fluorescence in rare gas-halide systems,¹ there has been considerable interest in developing these systems into efficient and powerful uv lasers.² Recent work at NRL has demonstrated efficient and powerful XeF laser operation in a neon diluent.³ However, a thorough understanding of the laser kinetics is necessary in order to project the maximum efficiency of this system. This paper

reports a kinetics scheme by which energy deposited by an electron beam is channeled into the upper laser level and is ultimately extracted. The scheme is derived from a computer simulation of an e-beam-pumped XeF laser operating at optimum experimental conditions. Processes which limit laser performance are discussed.

The computer model consists of two parts: first, an e-beam deposition section, in which the kinetic energy of near relativistic electrons is used to ionize and excite the laser gas, and, second, a chemical kinetics section, in which the energy deposited in the gas cas-

^{a)}Science Applications, Inc., Arlington, Va. 22015.

The energy deposited by the e-beam in the laser mixture is calculated using a high-energy electron deposition computer code¹ based on the work of Berger and Seltzer.⁵ Because the target gas is not "thin", the electrons traverse in a zigzag path which results in greater energy deposition. The total deposition for our device has been calculated to be approximately two and one-half times the Berger and Seltzer values, and has been verified experimentally by nitrous oxide dosimetry.

The second part of the computer code deals with kinetics. In this section chemical reactions transport the deposited energy along various competing channels, some of which lead to the upper laser level. The dominant chains are determined by following the excitation which is deposited initially in Ne^* and Ne^+ as it travels from species to species and eventually reaches the upper laser level or some other species. For example, our model indicates that when the excitation reaches Ne_2^+ this ion is five times more likely to recombine with F^- to form NeF^+ than with electrons to form Ne^* . Hence the dominant path leads from Ne_2^+ to NeF^+ and so forth until it reaches the upper laser level or a species which is unlikely to form the upper laser level. The model does not consider the internal structure of the XeF^+ molecules, that is, the role of the $\text{XeF}(\text{C})$ state and vibrational relaxation of the B state. However, these effects are taken into account in estimating the overall efficiency of the system. Many of the chemical reaction rates have been measured but several have only been calculated or at best estimated. For example, recombination reactions of the form $M^+ + \text{F}^-$, where M^+ is a rare gas atomic or molecular ion, have been calculated to reach a maximum of approximately $(2-3) \times 10^{-6} \text{ cm}^3/\text{sec}$ at a few atmospheres of pressure, and then to drop off linearly with increasing pressure.⁸ Consequently, for these reactions, we assumed a reaction rate of $1 \times 10^{-6} \text{ cm}^3/\text{sec}$ at our operating conditions of 5 atm. For electron dissociative attachment of the fluorine donor we assumed a rate of $1 \times 10^{-8} \text{ cm}^3/\text{sec}$.

In the Ne-Xe-NF₃ laser, energy is channeled into the upper laser level primarily through the mechanism of Penning ionization. Both ion and neutral channels contribute significantly. In each chain an important Penning step leads to the formation of Xe⁺, which is the primary intermediary in forming the laser upper level. The major kinetics chains are represented in Fig. 1. Most of the excitation energy results in forming Ne⁺ which, either directly or through complex ion species, reacts with F⁻ to form NeF⁺. The NeF⁺ molecule rapidly predissociates to form F⁺ which ionizes Xe.¹ This Penning reaction is the major source of Xe⁺, which can form the upper laser level through its recombination with F⁻. The major loss mechanism in this chain is quenching of F⁺ by NF₃. Although excited NF₃ has enough internal energy to react with Xe and form the upper laser level, this reaction has yet to be demonstrated. A significant fraction of the energy deposited produces Ne⁺ which directly or through complex molecules forms Xe⁺ by a Penning reaction. Emission from the Ne₂⁺ excimer is an apparent loss process from this chain but this radiation has sufficient energy to ionize Xe and thus constitutes an additional formation channel.

Almost all of the excitation energy which reaches the upper laser level travels through Xe^* which forms XeF^* by recombination with F^* . However, we speculate that at high pressure Xe^* forms the weakly bound complex, NeXe^* . Little is known of NeXe^* except that it has an emission spectrum.⁸ If NeXe^* is formed, it rapidly forms the upper laser level directly through recombination with F^* or indirectly through another species such as Xe_2^* or Xe^* , which is formed from dissociative recombination of NeXe^* or Xe_2^* . In any case once the excitation reaches Xe^* it is rapidly channeled into XeF^* . Under the experimental conditions which the computer model simulated,⁹ and which are given in Fig. 1, 44% of all the excitation which reaches the upper laser level is extracted as laser output, 13% is absorbed (principally by Xe_2^*), 26% is quenched (principally by Ne), and 17% is lost through fluorescence.

Recently Rokni *et al.*⁹ have investigated formation and quenching processes in Ne/Xe/F₂ mixtures and their results are in substantial agreement with the predictions of our model. However, in our model we have used NF₃ rather than F₂ as the fluorine donor because its use significantly increases the laser performance.¹⁰ Moreover, NF₃ quenches XeF* much less rapidly than F₂¹¹ so that the major quenching species of XeF* is neon in our model rather than the fluorine donor as in Rokni's case. As a final point, Rokni *et al.* show as a minor formation channel the reaction of F* with F₂ to produce F₂* which can react with Xe to form XeF*. Unfortunately, the equivalent formation process with NF₃ has yet to be demonstrated, hence in our model we are compelled to treat it as an interception process.

The estimate of the overall energy efficiency is uncertain to the extent that the products of the complex ion recombination reaction with F^+ are unknown as are the fate of these products. It has been generally accepted but not conclusively demonstrated that the upper laser level is formed with near unit efficiency as a pro-

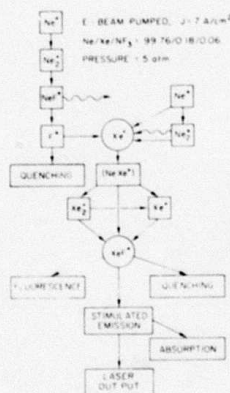


FIG. 1. Kinetics scheme for e-beam-pumped XeF laser in neon diluent. The species NeXe^* is in parentheses to denote that its presence is speculative. The operating pressure is 5 atm.

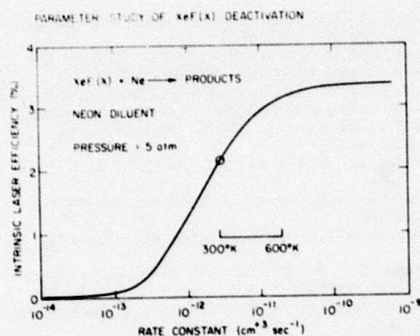


FIG. 2. Laser efficiency as a function of the XeF ground-state dissociation rate. A rate constant of 3×10^{-12} cm³/sec agrees with the experimental efficiency result of 2.0%. Increasing the gas temperature to 600°K should increase the laser efficiency significantly.

duct of the Xe⁺ and F⁺ recombination reaction. In addition, recent experiments on KrF formation in argon diluent indicate that in Kr⁺ recombination reactions, the product yield of KrF⁺ is high.¹² However, not much is known of the reaction products of the complex ions, NeXe⁺ and Xe₂⁺. It is possible that a substantial amount of excitation is channeled into the XeF(C) state which may not rapidly couple to the B state, or the excitation may be channeled into high vibrational levels of the B state which do not relax to the laser level. At this stage much work needs to be done on the excited states of XeF. To account for the uncertainty in the yields of these complex ions, we have calculated the laser efficiency assuming product yields of unity for one case, and one-fifth for the other. Under these conditions, the energy efficiency for formation of XeF⁺ is 9% for the unity case and 5% for the one-fifth case, likewise, the extraction efficiencies are 4 and 2%, respectively.

XeF has a weakly bound ground state which acts to trap the laser radiation and thus decrease the laser output. The ground state has a total well depth of 1100 cm⁻¹ and a depth of approximately 800 cm⁻¹ from the lower laser level.¹³ The laser radiation is absorbed by the ground state and is rapidly restimulated. The result of this "recycling" of the laser radiation is that the net stimulated emission rate is decreased and, consequently, more excitation is lost through fluorescence and quenching. Collision with neon atoms can break apart the XeF ground state and thus increase the laser output. In Fig. 2, the laser efficiency is given as a function of the ground-state removal rate. It is found that a dissociation rate constant of 3×10^{-12} cm³/sec which corresponds to one-half the gas kinetic rate and a well depth of 800 cm⁻¹ fits the observed efficiency of 2.0%.³ Heating the laser gas to 600°K would increase the break apart by an order of magnitude and the laser efficiency by 50% as can be seen in Fig. 2. However, we have not considered the effect of increased temperature on other aspects of the kinetics scheme such as formation, quenching, and absorption.

When neon is substituted for argon as the diluent in the XeF laser, a significant improvement in laser performance is observed which is due to the decrease in the transient absorption.³ Recent theoretical predictions of the absorption spectra of rare gas dimers indicate that Ar₂⁺ absorbs in the 350-nm region, whereas Ne₂⁺ does not.¹¹ In order to determine what species is responsible for the remaining absorption in the XeF laser, we compared to our kinetic model the results of several previous absorption experiments conducted in pure rare gas mixtures and the laser mixture.³ In Fig. 3 the observed absorption as a function of gas composition is compared to the relative densities predicted by the model.

In the first experiment, conducted in pure neon, we observed an absorption of 1.25%/cm which decreased to 0.2%/cm when 0.1% Xe was added to the mixture. Looking at the lower half of Fig. 3, we note that the only species that decreases significantly when Xe is added is Ne₂⁺, hence Ne₂⁺ is most likely the major absorber in pure neon plasmas. When the Xe concentration is increased to 1%, as in experiment three (Fig. 3), the absorption increases to 1.25%/cm. However, we note that the density of the excited neon species has decreased, while the densities of Xe₂⁺ and XeF⁺ have increased as has the absorption. In the final experiment, performed on the laser mixture, we note that the absorption has decreased significantly as have the Xe₂⁺ and XeF⁺ densities. By combining the theoretical estimate¹¹ of the absorption cross section at the laser wavelength of Xe₂⁺ with the model prediction of its density, we can calculate the absorption in the laser mixture due to Xe₂⁺, and this value, given by the X in

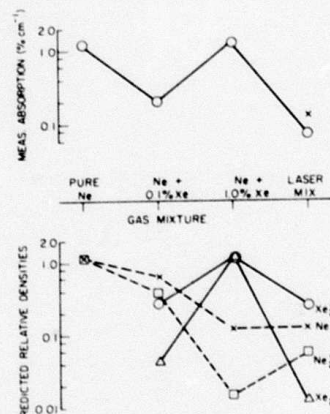


FIG. 3. Top: experimentally observed transient absorption at 351 nm in various gas mixtures; bottom: model calculations of the relative density of various species. The absorption decrease in neon when 0.1% xenon is added correlates with the decrease in the Ne₂⁺ density. The increased absorption in 1% xenon and subsequent decrease in the laser mix correlates with the Xe₂⁺ and XeF⁺ densities. The X in the top figure is the Xe₂⁺ absorption in the laser mixture calculated using the cross section of Ref. 13. Note that this quantity can explain the observed absorption.

Fig. 3, is in good agreement with the observed value. The evidence clearly points to Xe_2^+ as the dominant absorber.

In the XeF laser when neon is the diluent the dominant process for formation of the upper laser level is Penning ionization, a channel which does not exist in argon diluent. Because of the high operating pressure of this laser, a significant role is played by complex and poorly understood species such as NeXe^+ . An increase in the laser output of approximately 50% can be obtained by more effective removal of the XeF ground state. Use of neon as a diluent eliminates the transient absorption at the laser wavelength which exists in an argon diluent; however, under optimum laser conditions the major absorber is Xe_2^+ .

We wish to thank D. L. Huestis, SRI, for making available to us his unpublished data, and for helpful conversations.

- ¹M. F. Golde and B. A. Thrush, *Chem. Phys. Lett.* **29**, 486 (1974); J. E. Velazco and D. W. Setser, *J. Chem. Phys.* **62**, 1990 (1975).
- ²S. K. Searles and G. A. Hart, *Appl. Phys. Lett.* **27**, 243 (1975); J. J. Ewing and C. A. Brau, *Appl. Phys. Lett.* **27**,

350 (1975); F. R. Ault, R. S. Bradford, and M. L. Bhaumik, *Appl. Phys. Lett.* **27**, 413 (1975).

- ³L. F. Champagne, J. G. Eden, N. W. Harris, N. Djeu, and S. K. Searles, *Appl. Phys. Lett.* **30**, 160 (1977); L. F. Champagne and N. W. Harris, *Appl. Phys. Lett.* **31**, 513 (1977); L. F. Champagne, *Electronic Transition Lasers III*, edited by K. L. Kampa and H. Walther (Springer-Verlag, Berlin, 1978), p. 32.
- ⁴D. B. Brown, D. B. Wittry, and D. F. Kyser, *J. Appl. Phys.* **40**, 1627 (1969).
- ⁵M. J. Berger and S. M. Seltzer, NASA Report No. SP-3012, 1964 (unpublished).
- ⁶J. M. Wadehra and J. N. Bardsley, *Appl. Phys. Lett.* **32**, 76 (1978).
- ⁷N. W. Winter, C. F. Bender, and T. N. Rescigno, *J. Chem. Phys.* **67**, 3122 (1977).
- ⁸Y. Tanaka, K. Yoshino, and D. E. Freeman, *J. Chem. Phys.* **62**, 4488 (1975).
- ⁹M. Rokni, J. H. Jacob, J. A. Mangano, and R. Brochu, *Appl. Phys. Lett.* **32**, 223 (1978).
- ¹⁰L. F. Champagne (unpublished).
- ¹¹H. C. Brashears, Jr., D. W. Setser, and D. DesMarteau, *Chem. Phys. Lett.* **48**, 84 (1977).
- ¹²M. Rokni, J. H. Jacob, and J. A. Mangano, *Phys. Rev. A* **16**, 2216 (1977).
- ¹³J. Tellinghuisen, G. C. Tyson, J. M. Hoffman, and A. K. Hays, *J. Chem. Phys.* **64**, 4796 (1976).
- ¹⁴W. Wadt, D. C. Cartwright, and J. S. Cohen, *Appl. Phys. Lett.* **31**, 673 (1977).

COMPUTER CODE DEVELOPMENT AND APPLICATIONS

The versatility of the time-dependent laser kinetics computer code developed at NRL during FY 77 has proven to be invaluable throughout this past fiscal year in which the code was adapted to a variety of systems. Documentation has been accepted for publication¹ and should make the code usable and available to a larger number of researchers interested in the simulation of lasers, discharges, and chemical kinetics.

Both steady-state and time-dependent computer models were constructed to help unfold experimental data aimed at assessing the role of the C state in the XeF laser (see preceding manuscript). Data on important reactions in e-beam sustained discharges in Ne/Xe/NF₃ mixtures have been updated and numerical studies of energy flow and electron kinetics in such mixtures have been carried out and presented.² Additionally, modeling has been used to simulate a rare-gas-halide kinetics experiment which is used to isolate certain parts of the kinetics chain for measurements of important rates. Numerical simulation has helped to unfold the individual rates from experimental observations.

Applications of the modeling are cited in the previous and following sections of this report.

References

1. T. H. Johnson, L. J. Palumbo, and A. M. Hunter, "Kinetics Simulation of High-Power Gas Lasers," to be published in IEEE J. of Quantum Electronics (May 1979).

2. L. J. Palumbo, "The Role of Electron Kinetics in Discharge-Pumped Rare-Gas-Halide Lasers," Paper E-2, 31st Annual Gaseous Electronics Conference, Buffalo, NY (October 1978).

To be published in IEEE Journal
of Quantum Electronics
(May 1979)

ABSTRACT

KINETICS SIMULATION OF HIGH-POWER GAS LASERS*

Thomas H. Johnson, Louis J. Palumbo, and Allen M. Hunter

Numerical simulation of high-power gas lasers requires the integration of a variety of numerical techniques; simultaneous solutions must be obtained to a large set of ordinary differential equations, and several non-linear partial differential equations. A family of codes employing similar methods has been devised and has demonstrated remarkable success in predicting laser performance over a broad range of parameters. We describe here the appropriate techniques for dealing with gas kinetic equations, the steady-state Boltzmann equation, and physical optics. Modeling of both e-beam-pumped and e-beam sustained discharge-pumped lasers is described; complex electron kinetic processes are included. Results are shown for both krypton fluoride and xenon fluoride lasers.

* Work supported in part by DARPA

KINETICS SIMULATION OF HIGH-POWER GAS LASERS*

Thomas H. Johnson, U. S. Military Academy

West Point, New York 10996

Louis J. Palumbo, Laser Physics Branch, Optical Sciences Division,

Naval Research Laboratory, Washington, D. C. 20375

and

Allen M. Hunter, Department of Physics,

Air Force Institute of Technology

Wright-Patterson Air Force Base, Ohio 45433

I. INTRODUCTION

During the past decade, numerical simulation models for gas lasers have been developed to predict, with good reliability, the gross performance of gas lasers operating at infrared wavelengths. In moderately complex kinetic systems such as those of the CO₂ electric discharge laser [1], the CO electric discharge laser [2], and the DF-CO₂ transfer laser [3], it has been possible to predict total power and efficiency with some confidence. More detailed quantities have often eluded accurate prediction, usually because of uncertainties in fundamental kinetic processes. The results from these kinetics codes have been coupled with other techniques -- hydrodynamic models (especially for simulation of the gasdynamic laser) and both geometric and physical optics models -- to produce successful simulations of laser systems.

* Work supported in part by DARPA

With the advent, in the early '70s, of gas lasers operating at much shorter wavelengths -- in the visible and near ultraviolet -- it became necessary to develop new computational models. The kinetic processes of such systems are vastly more complicated than those of, for example, CO_2 lasers. This complication is both quantitative and qualitative. There are a great many more reactions, and kinds of reactions, which must be accounted for and balanced properly before one can simulate a real experiment. And, more significantly, the assumptions of (at least approximate) local thermodynamic equilibrium made by earlier simulations are clearly not valid in the new lasers. (In CO_2 modeling, for example, it is common practice to assume the vibrational modes to be individually equilibrated.) It becomes necessary, then, to update certain elastic and inelastic collision parameters through solution of a Boltzmann equation in concert with the solution of the gas kinetics equations.

The techniques presented here were assembled for the simulation of a particular pair of rare-gas-halide molecular lasers, the excimers krypton fluoride (KrF), operating at 2485\AA , and xenon fluoride (XeF), operating at 3532\AA . Where it is useful to illustrate by example, these systems will be used; and the results presented will involve simulations of laboratory experiments with these lasers. The methods are, however, quite general, and may be used with equal success on a great variety of complex systems. In fact, the techniques have been specialized along quite different lines by two of the authors, using two quite different computers (CDC 7600 and Texas Instruments ASC);

where different methods have been used to model specific aspects of the systems, both will be described here. Over rather a broad realm, one's choice of numerical methods represents, as much as anything else, one's aesthetic perceptions.

Physical Approximations

Energy is generally delivered most efficiently to the gases in these electronic-transition lasers through collisions with energetic electrons, either through direct pumping with electron beams or by application of an electric discharge (usually sustained by an e-beam). The essentials of the geometry for a direct-pumped laser are shown in Figure 1. The arrangement shown is for an unstable confocal resonator as used in the KrF physical optics calculations (see Section II).

For an e-beam sustained discharge, the essentials of Figure 1 remain correct. A discharge voltage is added in the third dimension (into the page), and the resulting current carried by secondary electrons (ionizations caused by the e-beam) pumps energy into the gas collisionally.

Note that, as far as the energetics are concerned, the problem may be treated in levels of approximation varying from zero-dimensional to three-dimensional. One may, for example, attempt to model the spatial and temporal anisotropies of energy deposition by the electron beam, which depend almost entirely upon the characteristics of the particular electron gun being used; or one may presume that the beam energy is deposited uniformly throughout the cavity. Similarly, if the laser is discharge-pumped, one may choose to model the spatial asymmetries of discharge current (which also depend on the e-beam

deposition anisotropies); or, again, one may ignore these. All models presented here make the simplest assumptions in both these cases, reducing the dimensionality to zero. Since both deposition anisotropies and discharge current asymmetries tend to degrade laser performance, the simulations will present a best-case prediction of performance. If energy deposition in a particular experiment is particularly poor because of any combination of these problems, an accurate simulation can be produced by tailoring the code's modeling of e-beam energy deposition to that actually measured, rather than that of a nominal ideal beam at the rated input current.

Temporal variations in the discharge voltage are modeled in these simulations, as discussed in Section III.

Variations along the laser beam axis can arise for a number of reasons, including all the above sources, longitudinal variations in flux level (especially those caused by using an unstable resonator, as in Figure 1), variations in absorption, or other mode-media interactions. The simplest forms of these simulation models also ignore all these variations as well. The resonator is presumed to be a simple Fabray-Perot resonator, so that the optical field is approximated as uniform in amplitude. The chemical concentrations everywhere in the cavity are then identical, and a simple uniform-gain approximation can be made (Section II). This zero-dimensional calculation can produce highly accurate results for overall energy, intensity, and efficiency, as well as reliable performance parameters for various modes of operation. One- and two-dimensional calculations can be performed by dividing the cavity into an appropriate number of cells and applying the kinetics

procedures to the updating of small-signal gain in each cell; intensity must then be calculated by a more detailed modeling of the radiation field. Techniques for doing this are discussed in Section II.

II. KINETICS AND RADIATION

Electronic transition gas lasers generally involve complex, branching chains of energy flow from initial pump excitation of background gas to eventual extraction of laser radiation. These energy chains include processes such as: energy deposition by electron ionization and excitation; energy transfer by various collisional mechanisms, including neutralization, displacement and "harpooning", leading to formation of the upper laser level; and collisional mechanisms which intercept excitation energy before it can reach the upper laser level, or which quench that level before stimulated emission occurs. Also, one must consider extraction of stimulated emission, including absorptions by various process in the gas and resonant reabsorption by the lower laser level (if there is one), laser cavity oscillation and coupling through output mirrors. A time-dependent model of the kinetics of such a system must define and update species densities for a large number -- typically between twenty and sixty -- gas components, including ground states, several excited states and ions of atoms and molecules, plus electrons and photons.

The time evolution of these components is followed by the solution of a set of coupled first-order ordinary differential equations -- one for each gas component. To the set of equations defining species densities are added further differential equations describing the

evolution of the photon field, the gas temperature and (in some models) coupled electrical circuit parameters. The species equations can be generally described as equating the rate of change of species density to a sum of contributing formation terms less a sum of depletion terms, viz,

$$\frac{dN_i}{dt} = \sum_j F_{ji} - \sum_k D_{ik} . \quad (1)$$

Here N_i is a particular species density, the F's are the formation terms and the D's the depletion terms. For example, consider a simple chemical reaction of the form $A + B \rightarrow C + D$, whose forward rate is characterized by a rate constant k ; if the species densities are expressed in cm^{-3} , the units of k are cm^3/sec (a unit of "particles" or molecules being understood in the numerator of the former and the denominator of the latter). For this reaction, the rate equations defining species C and D would contain the formation term

$$F = k [A] [B] ;$$

at the same time, the equations defining species A and B would contain the depletion term

$$D = k [A] [B] .$$

It has been found to be highly useful to code the equations to the greatest extent possible in symbolic format. The equations themselves are specified in an input data list in chemical reaction format, with the appropriate reactants and products expressed as symbolic names. The rate constants are included in this list, along with flags

specifying the conditions of their definition and sequence and source information. Some of the rate constants must be updated during the computation, being functions of gas temperature or electron energy distribution. The differential equations of the form of (1) are then generated internally by the computer code. This method not only makes it much easier to alter the set of equations (by addition or deletion of terms or reactions, or by change of reaction rates), it also greatly reduces errors attendant to such alterations, errors which arise with remarkable, almost spontaneous, ease in the complex tangle of reactions. Further, symbolic manipulation makes the definition and computation of a variety of output and diagnostic quantities much easier. And finally, it makes a single code the easily-adaptable basis for simulation of a wide variety of laser systems and chemical kinetics experiments: The entire composition of the simulated gas may be changed without altering the code itself. Experience has shown that an adequate symbolic system is one which employs names of up to six alphanumeric characters and defines reactions with up to four reactants and five products each.

Integration Schemes

Several different integration schemes for the chemical kinetics equations have been used successfully with these techniques in simulating KrF and XeF lasers. The reaction rates in these systems may vary by ten orders of magnitude or more, as may species concentrations. However, it has not been found to be necessary to employ any of the more sophisticated techniques developed to solve non-linear sets of

"stiff" equations. This is a result of the physical system itself. Most of the species densities rise extremely steeply in the first tenth of the simulation-time, requiring that the fastest rates define timesteps; later in the pulse, species densities tend to flatten out together, permitting quite long timesteps for all species, regardless of rate constant.

Simulations on the ASC computer have used a fourth-order Runge-Kutta-Treanor [4] algorithm, which provides for stiff systems. Both upper and lower limits to timestep size are user-specified through maximum limits on changes in the N_i or dN_i/dt . Limits of 5% change per timestep have been found to be sufficient for accuracy. Integrations requiring a few thousand timesteps (for a 1-2 μ sec laser pulse) for systems of 30 species and 100 reactions take about ten seconds of CP time.

The CDC 7600 versions of these simulations have also been run with a fourth-order predictor-corrector Hamming's method. However, detailed comparisons of simulation of KrF experiments using both Hamming's method and a far simpler modified-Newton's method integrator have shown the latter to be fully as accurate when used with a restrictive flux limiter on N_i and dN_i/dt ; the few extra integrations required for accuracy are more than compensated by the increased speed per timestep. The flux limiter has two steps. Assuming that a standard timestep DT has been set (or calculated as the remaining time in a longer edit interval), first calculate

$$(\Delta T_i)_1 = \text{ABS} \left(\frac{\frac{f_1}{dt} \cdot N_i + 100}{\frac{dN_i}{dt} + 10^{-100}} \right) \quad (2)$$

where f_1 is an arbitrarily chosen fraction (usually .05, as above).

The extra numbers in numerator and denominator are obviously to prevent zeros from fouling the calculation. (Compared to all real N_i , 100 is a very small number.) Then compare DT to $(\Delta T_i)_1 \cdot f_2$ for all species, where f_2 is another user-specified fraction; if DT is smaller than each of these, it remains the timestep. For N_i for which DT is larger, calculate

$$(\Delta T_i)_2 = \text{ABS} \left(\frac{\Delta N_i + 10^{-90}}{\frac{dN_i}{dt} + 10^{-100}} \right) \quad (3)$$

where ΔN_i is the change in N_i over the last timestep, and $\Delta \frac{dN_i}{dt}$ the change in formation/depletion rate over the last timestep. DT is then reset as the smaller of $(\Delta T_i)_1$ and $(\Delta T_i)_2$. Using this flux limiter, the modified-Newton's method integrator performs the benchmark integration just described in about 4 seconds of CDC 7600 time.

Electron-Beam Pumping

In electronic transition lasers, the first step in the kinetics chain leading to extraction of laser energy is the deposition of energy in the diluent gas by either photons or electrons; in high-power lasers, electron-beam pumping is usually chosen in preference to flashlamps. Relativistic electrons deposit energy as ionization and direct excitation; calculation of the rates of these reactions can be done a variety of ways. In one of the applications reported here, the stopping power calculations of Berger and Seltzer [5] were used. It is necessary to modify these calculations by a numerical factor (typically between 2 and 3) to account for the zigzag path the electrons follow through the

gas. Calculations by Hunter [6] have correlated existing experimental data to provide this multiplicative factor as a function of beam energy. The other application used results of a detailed electron transport code [7] , [8] which accounts for the beam's path deviations and allows for losses of incident electrons to backscattering.

Whichever method is used, the ionization and excitation rates are calculated initially (either by hand or in the initial executive portion of the code) to correlate to the specific e-beam energy desired. They are then supplied directly as loss and gain terms in the rate equations for the species gaining or losing in number density -- multiplied by an input-specified constant for the e-beam current density. This multiplier can also be defined as a function of time to allow for real variations in e-beam current. So, for example, the F terms (Eq. (1)) for ionic species would include contributions from the beam, as would the F terms for excited states. About three times more ions than metastables are created directly by the e-beam.

Obviously, this method is also appropriate for optically excited media, with appropriate redefinition of constants.

Lasing, Fluorescence and Absorption

Production of radiation in the laser cavity is treated by a uniform gain approximation. This approximation is generally good when the laser is operating at or near saturation and when there are no major non-uniformities of lasing states in the medium. For situations in which the gain cannot be approximated as uniform throughout the cavity, one- or two-dimensional optics codes (discussed later in this Section) must be coupled into the kinetics solution.

The differential equation defining the rate of change of intra-cavity laser intensity is

$$\frac{dI_L}{dt} = cI_L (\alpha - \alpha_{th}) \quad (4)$$

where I_L is the intensity in watts/cm², α is the net gain, and α_{th} is the threshold gain, the gain needed to overcome round-trip mirror losses. These are defined as

$$\alpha = \sigma_{se} (N_{ul} - N_{ll}) - \sum_n (\sigma_{ab})_n N_n, \quad (5)$$

$$\alpha_{th} = -\frac{1}{2\ell_c} \ell_n (R_1 R_2). \quad (6)$$

The term $\sigma_{se} (N_{ul} - N_{ll})$ is the small signal gain, in which N_{ul} and N_{ll} are the number densities of the upper and lower laser levels, respectively, and σ_{se} is the stimulated emission cross-section, defined

$$\sigma_{se} = \left(\frac{\lambda^2}{8\pi\tau_s} \right) \left(\frac{2}{\pi\Delta\nu} \right), \quad (7)$$

in which λ and ν are the wavelength and frequency at line-center, τ_s is the spontaneous life-time of the upper laser level, and $\Delta\nu$ is the spontaneous linewidth at half maximum. The remaining terms are:

$(\sigma_{ab})_n$ and N_n are the photoabsorption cross-sections and number densities of species n ; ℓ_c is the cavity length (distance between mirrors);

and R_1 and R_2 are the mirror reflectivities.

The spontaneous emission term is calculated as

$$\frac{dI_s}{dt} = \frac{N_{ul}}{\tau_s} (h\nu), \quad (8)$$

where $h\nu$ is the laser photon energy. Most of the spontaneous emission is lost as sidelight fluorescence. The small fraction directed within

the effective laser solid angle is added to the right-hand side of (4) ; this fraction is typically about $10^{-5} - 10^{-6}$. The remainder is discarded in the calculation of the laser flux, but is accounted for in determining energy lost by side fluorescence.

After the intra-cavity intensity has been updated, the instantaneous output intensity is given by

$$I_o = I_L \left(\frac{1 - R_1 R_2}{1 + R_1 R_2} \right) . \quad (9)$$

The denominator in this equation arises from considering both left and right traveling waves. The total laser energy radiated is simply calculated as

$$E_L = \int_0^{t_p} I_o dt \quad (10)$$

where t_p is the total pulse length.

Physical Optics Simulation

Optical resonator computations are performed using a Fourier optics propagation algorithm developed by T. C. Salvi [9]. The details of the optics theory are discussed in [10] and [11]. For computational purposes the laser cavity is represented by a series of discrete optical elements oriented transverse to the optical axis as shown in Figure 2. Two of these, M_1 and M_2 , are the mirrors of a positive branch confocal unstable cylindrical strip resonator. The elements, S_1 , between the mirrors are gain sheets. The amplification and phase transformation that the electric field experiences in propagating through a gain region of thickness Δz is accounted for in one operation

at each gain sheet. The thickness Δz is kept sufficiently small that

the average intensity within a gain region is approximated well by $\frac{I_i}{g\Delta z} [e^{g\Delta z} - 1]$. The intensity entering gain region i from the left is I_i^+ . The corresponding intensity entering from the right is I_i^- .

The electric field is computed for N points at each optical element. These points are equally spaced so that a Fast Fourier Transform (FFT) can be used to perform the required discrete Fourier transforms. The optical coordinate system expands with the geometrical optical rays so that each element is resolved equally well with N points. The electric field is represented as a linear combination of plane waves

$$U_i(x) = \int_{-\infty}^{\infty} A_i(f_x) \exp [i2\pi f_x x] df_x. \quad (11)$$

The Fourier spectrum is propagated analytically from one optical element to the next by the transfer function $H_i(f_x, \Delta z_i)$

$$H_i(f_x) = e^{ikz} e^{-i\pi\lambda\Delta z_i f_x^2} \quad (12)$$

so that the electric field at the next optical element is given by

$$U_{i+1}(x) = \int_{-\infty}^{\infty} A_{i+1}(f_x) \exp [i2\pi f_x x] df_x \quad (13)$$

where $A_{i+1} = A_i H_i(f_x)$. Propagation is done in frequency space; amplification and phase transformation are done (discretely) in configuration space.

The transfer function has a strong oscillatory character compared with the relatively slowly varying Fourier spectrum. Since $H(f_x)$ depends

on the resonator geometry only, H is carefully averaged using a fine mesh for each of the discrete spatial frequencies. This minimizes sampling errors and allows a relatively coarse mesh to be used in computing U .

The number of points used to compute the electric field is large compared with the number of points used to represent the intensities I_1^+ and I_1^- that are used in the kinetics calculations. The laser medium is typically divided into 30 cells, 10 of which are assigned to each of 3 gain sheets. This fluid resolution has been adequate to simulate 1- and 2-meter long cavities in KrF lasers. The electric field is underresolved even with 512 points for each optical element. Values of N in excess of 30,000 are required to resolve each of the resonator Fresnel zones adequately. The larger number of points serves to resolve the small amplitude, high frequency oscillations in the electric field. Since these oscillations are unimportant in power extraction calculations and a relatively small N allows predictions of uniform optical phase in the resonator (as expected for large Fresnel numbers), values of N ranging between 64 and 512 have been used in computations. Plots of intensity and phase distributions of the field for two typical calculations are presented in Section V.

The temporal advancement of kinetics and optics calculations is treated sequentially. The kinetics variables in each of the fluid cells are advanced over a period Δt while holding the cavity intensity constant. The kinetics variables are then held constant while the optical field is propagated. It is necessary that the laser gain does not change significantly during Δt . If Δt is not controlled carefully,

the relaxation oscillations that result from coupling the laser medium to the radiation field can cause undamped numerical instabilities. We have used a Δt corresponding to half of a photon round trip in the resonator, although this approaches the limit of numerical stability for a 2 meter cavity.

III. DISCHARGE MODELING

The remaining source of pump power to the laser medium, the electric discharge, must now be discussed in greater detail. The application of an electric discharge can be a very efficient means of supplying lasing energy, but it introduces a great many difficulties to both the experiment and the simulations.

The problems for simulations stem from the fact that, in the presence of an electric discharge, the electron distribution function is no longer Maxwellian. The rates for all those processes directly involving the secondary electrons accelerated in the discharge -- ionization, excitation, attachment and recombination -- depend upon the precise shape of the electron distribution function. Hence, a solution must be obtained to a Boltzmann equation defining that distribution function, and the relevant processes' cross-sections integrated over that distribution function.

For the lasers discussed here, and indeed for most electronic-transition lasers currently under investigation, it is fortunately adequate to assume that the electron distribution thermalizes on time-scales short compared to other processes of interest. In discharge-pumped KrF mixtures, for example, this time is calculated to be a small fraction of a nanosecond, while typical chemical kinetics timesteps

are several nanoseconds or more. Thus, it is adequate to solve a steady-state Boltzmann formulation at regular intervals in the kinetics calculation, rather than to attempt a complete time-dependent solution of the Boltzmann equation in parallel with the kinetics (which would prove to be a calculation too long to be of practical interest).

Hence, we present here a convenient and fast procedure for solving a steady-state Boltzmann equation to obtain quantities of interest for laser kinetics. Experience with particular gas/discharge systems will teach the user how often the Boltzmann routine need be called during each kinetics simulation. In general, it is adequate to prescribe that the routine be called whenever the electron density (calculated by the kinetics equations), average electron temperature (estimated) or gas temperature (calculated by the heat balance equation) changes by 10%.

Boltzmann Transport Equation

The steady-state Boltzmann equation for the electron energy distribution function (where u is the electron kinetic energy in eV) can be written [12]

$$\begin{aligned} & \frac{1}{3} \left(\frac{E}{N} \right)^2 \frac{d}{du} \left(\frac{u}{Q_1} \frac{df}{du} \right) + \frac{2m}{M} \frac{d}{du} (u^2 Q_2 f) + \frac{2mkT}{Me} \frac{d}{du} \left(u^2 Q_2 \frac{df}{du} \right) \\ & + \sum_j (u + u_j) f(u + u_j) Q_j(u + u_j) - u f(u) \sum_j Q_j(u) \\ & + \sum_j (u - u_j) f(u - u_j) Q_{-j}(u - u_j) - u f(u) \sum_j Q_{-j}(u) = 0 \quad , \quad (14) \end{aligned}$$

where E is the electric field strength, N is the total gas particle density, e and m are the electron charge and mass respectively, k is

Boltzmann's constant, and T is the molecular temperature.

The mean molecular weight, M , is calculated by summing over all the mixture components.

$$M = \sum_n M^n G^n, \quad (15)$$

where M^n is the molecular mass of component n and G^n is its mole fraction.

The mole-weighted momentum transfer cross section, Q_1 , is calculated from

$$Q_1(u) = \sum_n Q_m^n(u) G^n \quad (16)$$

while the reciprocal-mass-weighted momentum transfer cross section, Q_2 , is given by

$$Q_2(u) = \sum_n \frac{M Q_m^n(u) G^n}{M^n}. \quad (17)$$

In these expressions, $Q_m^n(u)$ is the total electron momentum transfer cross section for a collision between an electron of energy u and the n th gas component.

The j th inelastic process involves an electron energy loss of u_j and has a cross section of $Q_j(u)$, while the j th superelastic processes, involving an electron energy gain of u_j , has a cross section of $Q_{-j}(u)$. The superelastic cross section is derived from the inelastic cross section by the principle of detailed balance viz,

$$Q_{-j}(u) = \frac{u + u_j}{u} Q_j(u + u_j). \quad (18)$$

The electron energy distribution function, f , is normalized so that $\int_0^\infty u^{\frac{1}{2}} f(u) du = 1$. Thus $N_e u^{\frac{1}{2}} f(u) du$ (where N_e is the total electron density) is the number density of electrons with energies in the range from u to $u + du$.

Difference Version

Taking straightforward differences of the derivative terms in (14), the equation can be cast easily in one-dimensional tridiagonal form for the independent variable f :

$$(B - A) f_{i-1} = (A + B) f_{i+1} + (C - 2A) f_i + S \quad (19)$$

where the quantities A , B , C , and S are defined

$$(\Delta u)^2 A = \frac{1}{3} \left(\frac{E}{N} \right)^2 \frac{u}{Q_1} + \frac{2mkT}{Me} u^2 Q_2, \quad (20)$$

$$2\Delta u B = \frac{1}{3} \left(\frac{E}{N} \right)^2 \left[\frac{1}{Q_1} - \frac{u}{Q_1^2} \frac{dQ_1}{du} \right] + \frac{2m}{M} u^2 Q_2 \quad (21)$$

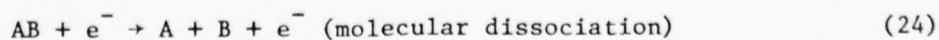
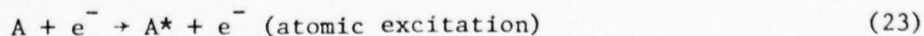
$$+ \frac{2mkT}{Me} \left[2uQ_2 + u^2 \frac{dQ_2}{du} \right],$$

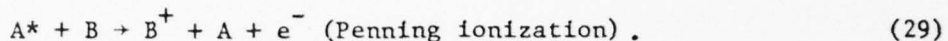
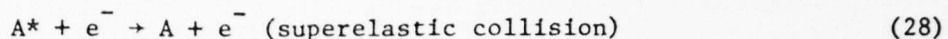
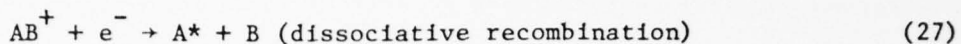
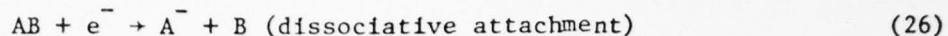
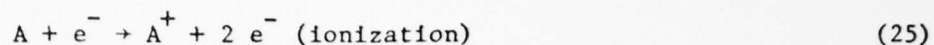
$$C = \frac{2m}{M} \left[2uQ_2 + u^2 \frac{dQ_2}{du} \right], \quad (22)$$

and S represents the last four summations in Eq. (14).

Assumptions, Approximations and Solution

Several types of electron collision processes are considered. Schematically, these are:





Here A and B represent two atoms in the gas mixture and e^- is an electron. The asterisk refers to an electronically excited atom while the superscript plus sign designates an ion. One may also have multiply-excited states, excited from both the ground state and lower-lying metastables; ionization of metastables; molecular ion processes; in short, all possible combinations of such reactions.

Processes (23), (24), and (28) involve no loss or gain of electrons but only a redistribution in energy, and thus the contributions of these processes to the electron energy distribution function are treated exactly by this algorithm. The other processes, (25), (26), (27), and (29) involve either the gain or loss of an electron and certain assumptions are made in the treatment of these processes. For ionization (Reaction (25)), it is assumed that the incident electron loses an amount of energy equal to the ionization potential of A and the secondary electron is created with zero energy. Furthermore, the effect of these newly created zero-energy electrons on the electron energy distribution function is ignored (although their contribution to the total electron density is accounted for by the chemical kinetics equations). Similarly, electrons created by Penning ionization, process (29), are ignored as far as their effect on f is concerned but are accounted for in computing the total electron density in the

kinetics equations. A comparison of the number of electrons produced by electron impact ionization and by Penning ionization with the number produced by e-beam ionization is made after each run to assure the validity of neglecting the effect of the former electrons on f .

Dissociative attachment and dissociative recombination (processes (26) and (27), respectively) involve the loss of electrons from a continuum of energies but no subsequent creation at other energies. These are treated in the Boltzmann code by including an inelastic loss term but no gain term.

The recursion relation (19) is solved by the following method. Suppose that the energy axis has been divided into I bins, each of width Δu . Choose a small number, say 10^{-20} , and set $f(I) - f(I-1) = 10^{-20}$. Then using (19) solve for all $f(u)$ down to $f(1)$. Whenever a particular value of $f(u)$ becomes greater than 10^{20} , multiply all values calculated thus far by 10^{-20} and proceed. When all $f(u)$ have been calculated, normalize the distribution as specified. This process straightforwardly deals with all elastic collision terms and with all inelastic terms -- ionization, excitation, attachment and dissociative recombination -- which remove energy from the electron gas.

Superelastic Collisions

These inelastic collisions, also known as "collisions of the second kind", cause difficulties for a solution technique which moves down the energy axis because they scatter electrons up the energy axis; thus an iterative solution is necessary. The trial solution for $f(u)$ is obtained exactly as before, ignoring the existence of the superelastic

terms.

At this point, approximate values of f exist at all grid points allowing an estimate of the summation involving $f(u-u_j)$ in Eq. (14). Several iterations are then performed to yield successively better approximations for f . The superelastic terms are introduced partially for the first iteration by multiplying their contribution by $\sim 10^{-3} - 10^{-2}$. For each successive iteration, this multiplying factor is increased until it remains at unity for the last few iterations. Typically, from four to six iterations are required for convergence.

Electron-Electron Interactions

Collisional processes within the electron gas can be of great significance in discharge-pumped lasers when the electron density in the gas grows great (in excess, roughly, of $2 \times 10^{14} \text{ cm}^{-3}$) [13]. These densities will occur when the gas is pumped hard with the discharge, or when the discharge is run in a self-sustained mode. Electron-electron interactions change the electron distribution function, tending to drive it toward a Maxwellian distribution at temperature T_e , without adding energy to the electron gas.

In velocity (v) space, the electron-electron collision operator is [14], [15]

$$\left(\frac{df_o^1}{dt} \right)_{ee} = \frac{Y}{v^2} \frac{\partial}{\partial v} \left[f_o^1(v) I_o^o(v) + \frac{mv^2}{3} \left(I_2^o + J_{-1}^o \right) \frac{\partial f_o^1}{\partial \epsilon} \right] \quad (30)$$

where $N_e = \int f_o^1 d^3v$, is the electron number density with f_o^1 in units of $\text{of sec}^3 \text{ cm}^{-6}$

$$\epsilon \equiv mv^2/2$$

$$Y \equiv 4\pi \left(\frac{e^2}{4\pi\epsilon_0 m} \right)^2 \ell n \Lambda$$

$$I_0^o \equiv 4\pi \int_0^v f_o^1 x^2 dx$$

$$I_2^o \equiv \frac{4\pi}{v^2} \int_0^v f_o^1 x^4 dx$$

and

$$J_{-1}^o \equiv 4\pi v \int_v^\infty f_o^1 x dx .$$

Using a normalized distribution function, $\int_0^\infty f_o(u) u^{1/2} du = 1$, this operator can be rewritten in energy (u) space as

$$\begin{aligned} \left(\frac{\partial f_o}{\partial t} \right)_{ee} = N_e (4.84 \times 10^{-5}) \ell n \Lambda u^{1/2} \frac{\partial}{\partial u} \left[f_o(u) I_0^o(u) \right. \\ \left. + \frac{2u}{3} \left(I_2^o + J_{-1}^o \right) \frac{\partial f_o}{\partial u} \right] \end{aligned} \quad (31)$$

where

$$I_0^o \equiv \int_0^u f_o x^{1/2} dx$$

$$I_2^o \equiv u^{-1} \int_0^u f_o x^{3/2} dx$$

and

$$J_{-1}^o \equiv u^{1/2} \int_u^\infty f_o dx .$$

The term Λ above is the ratio of the Debye screening radius to the impact parameter required for a 90° deflection of an electron in a binary collision with another electron. We assume $\ell n \Lambda$ is constant since it varies slowly with N_e and T_e . The constant 4.84×10^{-5} is a unit conversion factor which incorporates Y and allows the electron

mass to be expressed in grams.

Since this operator effectively represents a diffusive process in energy space, it will scatter electrons up the energy axis as well as down; hence, like the superelastic collision term, it must be solved iteratively. Fortunately, the electron-electron operator can be included in the coding along with the superelastic operator, in the same iteration loop: no numerical difficulties arise from their conjunction, and whatever criteria are necessary for gradual introduction of the superelastic term will be more than sufficient for the electron-electron term. Thus, although considerable extra algebra is added by the electron-electron term, additional costly iterations to the solution of f are avoided. To be consistent in cgs units and energy in eV, the correct term to include in the iteration is

$$N^{-1} \left(\frac{3.2 \times 10^{-12}}{m} \right)^{-1/2} \left(\frac{\partial f_o}{\partial t} \right)_{ee} ,$$

where N is the total gas density in cm^{-3} and $\left(\frac{\partial f_o}{\partial t} \right)_{ee}$ is defined by (31); because of the constant factor, the resulting term will have units $\text{cm}^2 \text{ eV}^{-1/2}$.

Rate Coefficients and Transport Properties

Once a normalized electron distribution function has been calculated, it is a simple matter to calculate the rate coefficients for inelastic kinetic processes by integrating (with, for example, Simpson's rule) the appropriate cross-section over the energy range of the distribution function. Since the electron velocity, v , is given by

$$v = \left(\frac{2eu}{m} \right)^{1/2} \quad (32)$$

the rate coefficient, k_j , for process j can be computed from

$$k_j = \langle Q_j v \rangle = \left(\frac{2e}{m} \right)^{1/2} \int_0^\infty Q_j(u) u f(u) du. \quad (33)$$

Here, Q_j is the appropriate cross-section for ionization, excitation, deexcitation (superelastic), attachment or recombination.

Other important transport properties of the discharge gas can be obtained by similar simple integrations. These include:

The electron drift velocity:

$$w = \frac{1}{3} \left(\frac{E}{N} \right) \left(\frac{2e}{m} \right)^{1/2} \int_0^\infty \left(\frac{u}{Q_1} \right) \frac{\partial f}{\partial u} du \quad (34)$$

The transverse diffusion coefficient:

$$D_T = \frac{1}{3N} \left(\frac{2e}{m} \right)^{1/2} \int_0^\infty \frac{uf}{Q_1} du \quad (35)$$

The electron mobility:

$$\mu = \frac{w}{E} \quad (36)$$

The average electron energy:

$$\bar{u} = \int_0^{\infty} u^{3/2} f \, du \quad (37)$$

and the electron characteristic energy:

$$\epsilon_k \equiv \frac{D_T}{u} \quad (38)$$

Power Balance

Once the electron energy distribution function is known, the partitioning of the discharge power (product of discharge voltage and current) into the various energy channels of the laser gas can be computed. The balance of this power provides a numerical check on the Boltzmann equation solver, while partitioning provides insight into the processes responsible for limiting or enhancing laser efficiency.

The electrons gain energy by being accelerated in the applied electric field. The rate of gain of electron energy per unit volume is $EJ_D = EeN_e w$, where J_D is the discharge current density. Some of this energy is transferred to the gas particles through the several types of collisional process. The rate of transfer of energy per unit volume for a particular binary process, p , involving the collision of an electron and a particle designated by subscript j is

$$P_{pj} = N_e N_j \left(\frac{2e}{m} \right)^{1/2} \int_0^{\infty} \Delta E_{pj} Q_{pj} u f \, du \quad (39)$$

where Q_{pj} is the cross section for process p , and ΔE_{pj} is the average electron energy lost in the collision. The energy transfer rates for specific electron collisional processes of particular interest are shown in Table I.

External Circuit Coupling

When simulating an existing laser experiment, the measured temporal waveform of the discharge voltage, $V_D(t)$, is used as an input parameter to the code. However, when the code is operated in a predictive mode, one must be able to compute the time history of V_D by coupling the external circuit parameters to the discharge kinetics.

The method for achieving this coupling is described here by considering, as a particular example, the circuit is shown schematically in Figure 3. This circuit contains three elements with properties (capacitance, inductance, and resistance) which remain constant in time and a fourth element (the laser discharge) having a time-varying impedance which depends on the other three circuit elements, the discharge kinetics, and the external ionization source. The discharge impedance, Z_D , can be expressed as,

$$Z_D = \frac{V_D}{I} = \frac{Ed}{N_e A e w} \quad (40)$$

where V_D is the potential across the discharge, I is the current in the circuit, w is the electron drift velocity (Eq. (34)) and d and A are the discharge gap length and area, respectively.

If one selects three independent variables which describe the LRC circuit of Figure 3 to be the discharge current, I , the discharge

voltage, V_D , and the time derivative of the discharge current, dI/dt (Define $G \equiv dI/dt$), then three differential equations involving these variables may be derived in a straightforward manner by applying Kirchhoff's laws to the LRC circuit:

$$\frac{dV_D}{dt} = \left[\frac{G}{eA} - \frac{dN_e}{dt} w \right] \frac{1}{N_e (dw/dV_D)} , \quad (41)$$

$$\frac{dG}{dt} = \left[\frac{dV_D}{dt} + RG + \frac{I}{C} \right] \frac{1}{L} , \quad (42)$$

$$\frac{dI}{dt} = G . \quad (43)$$

The following relationship between the current and the drift velocity was used in deriving equations (40) and (41):

$$I = J_D A = e w N_e A , \quad (44)$$

where J_D is the discharge current density. The time rate of change, dN_e/dt , of the electron density is determined from the solution chemical kinetics equations.

Since equations (41) through (43) are a set of coupled first order linear differential equations, they may be appended to the set of chemical kinetics equations and solved using the same algorithm. Thus the kinetics integrator keeps track of (and requires starting values of) I , dI/dt , and V_D .

The electron drift velocity and hence its derivative with respect to discharge voltage, dw/dV_D , depend mainly on V_D . They are coupled to the particle kinetics through their weaker dependence on fractional

excitation and ionization but this effect was tested and found to be small enough to ignore for the present purposes. This negligible dependence allows the circuit equations to be merged into the set of chemical kinetics equations and solved on the same time grid along with the latter without frequent calling of the time-consuming Boltzmann equation solver. A table giving the functional dependence of dw/dV_D on V_D is generated initially for an average estimated fractional excited state density and ion density and for the range of V_D expected in a given simulation. This table is then interpolated to obtain the value of dw/dV_D required during the kinetics/circuit integration.

The absolute value of E/N ($= V_D/Nd$) is fed into the Boltzmann transport equation solver when required to compute an updated electron energy distribution function.

The power, P_D , and the energy, E_D , deposited in the laser gas by the discharge are compared with the laser power and energy output to determine intrinsic laser efficiency. These quantities are given by,

$$P_D = V_D I \quad \text{and} \quad E_D = \int V_D I \, dt.$$

Obviously, this procedure can be adapted to accommodate an external circuit of arbitrary topology simply by deriving the appropriate set of differential equations analogous to Eqs. (41) - (43).

IV. OUTPUT AND DIAGNOSTICS

A well-calibrated laser kinetics code may be used, like any other simulation code, as a design aid to predict the performance of various system parameters. The code may actually be more useful, however, for studying experiments that have been performed than for predicting

the results of future experiments. The easy accessibility of virtually every single physical parameter, many of which cannot be measured directly (and are costly and time-consuming to measure inferentially), is what makes such a code an invaluable tool in understanding complexly interactive systems, such as the rare gas-halide lasers. It is important, then, that one's output parameters be carefully designed to provide the most useful information.

Assuming that a standard output interval has been established as a small fraction of the entire pulse length (pump + laser + after-glow), several quantities are of obvious interest: radiation parameters (intensity, energy radiated, fluorescence, net gain, total absorption); plasma properties and power balance (as defined in Section III); and the intrinsic or "local" efficiency of the pump process. This last is defined as the laser energy radiated divided by the total energy deposited in the gas, and can be calculated by summing all the excitations, ionizations, and heating caused by the e-beam and discharge. Three other efficiency quantities are of interest. The creation efficiency (number of upper laser levels formed divided by number of ions made); the radiation efficiency (number of laser photons produced divided by number of upper laser levels formed); and fluorescence yield (product of the previous two).

For e-beam sustained discharge-pumped lasers, several other quantities are of interest. Most frequently used is the discharge "enhancement", which is defined (by convention) as power deposited by the discharge divided by power deposited by the e-beam. Again, this

quantity can be calculated exactly, since the precise number of discharge-induced excitations and ionizations is known; it is useful, for purposes of comparison, to calculate and display the standard approximation to discharge enhancement, viz,

$$\epsilon_{\text{Approx}} = \frac{J_D \cdot E}{\epsilon_A \gamma N_A - \sum_m (\epsilon_I \dot{n}_{I m})} \quad (45)$$

where J_D and E are the discharge current density and field respectively, ϵ_A is the average energy per ion pair, γ is the attachment rate, N_A is the number density of attaching species, and n_I and ϵ_I are the total number density and ionization potential for ions of species m formed by the discharge. The ionization rate ratio (the ratio of instantaneous values of the rates of ionizations driven by the discharge and ionizations driven by the e-beam) can also be of particular interest; when this ratio passes about .3, the discharge is heading for instability. Finally, the metastable loss rate ratio (number of metastable atoms ionized divided by number of metastable atoms forming the upper laser level) can also be a useful measure of discharge performance.

The actual temporal variations of the species number densities and their rates of change -- printed intermittently and plotted on a semi-log scale at the end of the pulse -- are invaluable raw data, only a small fraction of which can actually be measured in any particular experiment.

Also of particular value in analyzing the importance of various kinetic processes is the display of the total contribution to each species' formation and depletion of each of the reactions which affects

that species. With this data, one can decide precisely which of the competing energy paths dominates the laser performance. One can also decide at a glance which reaction rates need to be known precisely and which can be treated with order-of-magnitude estimates.

V. RESULTS

We present in this section representative results of simulations of two different lasers, krypton-fluoride (KrF) and xenon-fluoride (XeF), done with two different codes.

Two KrF simulations are summarized in Table II to demonstrate the high accuracy with which these methods can reproduce experimental results. Some of the excellent agreement between simulation and experiment shown here must be regarded as fortuitous, if only because some of the measured data are inferential. However, these simulation results are not chosen because they are the closest yet obtained: they are in fact representative. Similar accuracy has been obtained in simulating many other KrF laser experiments performed at Maxwell Laboratories, Inc., AVCO Everett Research Laboratories, and Northrop, and in simulating kinetics and absorption experiments at the same places and at Stanford Research Institute.

Some of the general features of KrF lasers run at room temperature can be observed in these results. The total energy density was relatively low -- about 2 joules/liter in experiment 1 and about 1 joule/liter in experiment 2 -- because the e-beam currents were low and because experiment 1 was run at 1 atmosphere total pressure. At total pressures of about 2-2.5 atmospheres and e-beam current densities

10 Amps/cm² or more, one can produce 10 joules/liter reliably; harder pumping can more than double this number, but at severe penalties in local efficiency. The local efficiency of experiment 1 (~ 8%) is representative; values of 10-12% can be obtained with reliability in e-beam pumped lasers. Discharge-pumped efficiencies are in fact typically lower, though by a factor of about 1.2, rather than the factor of 2 illustrated by these experiments.

Typical results of one-dimensional physical optics resonator simulations are shown in Figures 4 and 5. In each figure, the top drawing shows the distribution of intensity across the beam incident on the output mirror of an unstable confocal resonator; the bottom drawing shows the phase distribution across the beam. Figure 4 is from the simulation of an e-beam excited laser at AVCO Everett Research Laboratories. The cavity length was 1 meter, with 71% output coupling; the e-beam current density was 11.5 Amps/cm², and the 1.2 atmosphere gas was partitioned 97.5 Ar/2.3 Kr/.2 F₂. Figure 5 shows results of an optics simulation of experiment 2 in Table II. The flat phase distribution resulting in both calculations is a gratifying result.

More detailed versions of these and other simulation results, with extensive interpretation, may be found in [14].

As an example of XeF modeling, results of a simulation of an e-beam-controlled XeF laser are compared with experiment [16] in Table III. For these calculations, the measured e-beam current and discharge voltage waveforms were used as input to the code.

The predictions of laser performance agree within experimental error. The slightly high values for optical output may be explained from the incomplete treatment by the model of direct formation and mixing (by heavy particles and electrons) of the B and C states of excited XeF. Detailed studies of the role of the C state in XeF lasers have been carried out for e-beam pumping [17] but the effect of discharge electrons (possibly increased mixing) in XeF B- and C-state kinetics is not yet well understood.

Curves showing the computed temporal evolution of selected laser-medium components for the XeF laser model of Table III are plotted in Figure 6. The pump pulses (e-beam and sustainer) for this simulation are switched on at a time corresponding to zero on the abscissa of Figure 6, have a 100 ns risetime and are cut off at 1200 ns.

The curve labeled " $h\nu_L$ " is the number density of intracavity laser photons traveling along the laser axis. The buildup time of ~ 200 ns for the laser flux agrees well with the experiment. Note the drop in XeF* density when the laser flux begins to build up towards saturation. The curve for $NeXe^+$ is shown since for these conditions it is the main precursor of the upper laser level, XeF*.

For long-pulse rare-gas-halide lasers it has been observed that the pulse duration over which one can obtain high efficiency is limited by the onset of discharge instability. Some insight

into the mechanism for the instability onset is apparent from Figure 6. The steady rise in electron (e^-) density during the pulse is shown from the kinetics calculations to be due to a steadily declining electron loss rate caused by depletion of the electron attacher, NF_3 . The dashed curve in the figure indicates an NF_3 , a depletion of about a factor of two for the conditions modeled here.

The increase in ionization rate accompanying the rise in electron density, when coupled with a reduced attachment rate caused by NF_3 depletion, tends to drive the discharge toward instability. Both the experiment and the simulation show that the discharge remains stable for the complete 1200 ns pump pulse at 160 J/l total energy input. However, for an E/N value only $\sim 10\%$ higher than that used for the experiment of Figure 6, the model shows a faster than exponential rise to an unrealistically high electron density before pump cutoff and, in agreement, the experiment shows a discharge arc resulting in a rapid drop in discharge impedance and premature termination of the optical pulse.

VI. CONCLUSION

None of the individual techniques described here is particularly novel. But the careful interworking of them has produced a predictive capacity of unprecedented precision in high-powered lasers, and made significant contributions to the developments of these lasers. These results were obtained not by concentration

on sophisticated numerics, but by close cooperation with experimentalists while both codes and lasers were being developed. In fact, conscientious efforts were made to keep the numerics the simplest that could be made to do, so that experimental uncertainties were always greater than computational ones. In such a hybrid model the chief difficulties one must be conscious of arise not from subtleties in the numerical approximations themselves, but from inconsistencies (qualitative and quantitative) in the fusion of many physical assumptions.

VII. ACKNOWLEDGEMENTS

One of the authors (LJP) extends his gratitude to T. G. Finn and L. F. Champagne for their close cooperation in developing the XeF code and for providing experimental data for comparison with calculations.

REFERENCES

1. D. H. Douglas-Hamilton and R. S. Lowder, "Carbon Dioxide Electric Discharge Laser Kinetics Handbook," AFWL TR-74-24, Air Force Weapons Laboratory, New Mexico, 1978.
2. P. W. Milonni and A. H. Paxton, J. Appl. Phys. 49 (1978), 1012.
3. T. H. Johnson and A. M. Hunter, "DF-CO₂ Transfer Laser Kinetics Code," Laser Digest, Air Force Weapons Laboratory, New Mexico, (Fall, 1975), 174.
4. C. E. Treanor, Mathematics of Computation 20 (1966), 39; also, C. E. Treanor, Cornell Aeronautical Report No. AG-1729-A-4 (January, 1964).
5. M. J. Berger and S. M. Seltzer, NASA Report No. SP-3012, National Aeronautics and Space Administration, Washington, D. C. (1964).
6. R. O. Hunter, Maxwell Laboratories, Inc., private communication.
7. D. B. Brown and R. E. Ogilvie, J. Appl. Phys. 37 (1966) 4429.
8. D. B. Brown, D. B. Wittry and D. F. Kyser, J. Appl. Phys. 40 (1969), 1627.
9. T. C. Salvi, Laser Digest, Air Force Weapons Laboratory, New Mexico (January 1975), 71.
10. D. E. Phelps, R. Baumgardner and G. H. Canavan, AIAA paper (February, 1974) 74-181.
11. E. A. Sziklas and A. E. Siegman, Appl. Opt. 14 (1975), 1874.
12. L. S. Frost and A. V. Phelps, Phys. Rev. 127, (1962), 1621; also J. J. Lowke, A. V. Phelps and B. W. Irwin, J. Appl. Phys. 44 (1973), 4664.

13. W. H. Long, Jr., Appl. Phys. Lett. 31 (1977), 391.
14. T. H. Johnson and A. M. Hunter, "Physics of Krypton Fluoride Lasers," submitted to J. Appl. Phys.
15. I. P. Shkarofsky, T. W. Johnston, and M. P. Bachynski, "The Particle Kinetics of Plasmas," Addison-Wesley, London (1966), 284.
16. L. F. Champagne and N. W. Harris, Appl. Phys. Lett. 33 (1978), 248.
17. T. G. Finn, L. J. Palumbo, and L. F. Champagne, to be published in Appl. Phys. Lett. (Jan. 1, 1979).

TABLE I

DISCHARGE POWER BALANCE

PROCESS	CROSS SECTION	ENERGY TRANSFERRED PER COLLISION	RATE OF ENERGY TRANSFER PER UNIT VOLUME
Momentum transfer	$Q_{m,j}$	$\frac{2m}{M} u^a$	$\frac{2m}{M} N_e N_j \left(\frac{2e}{m}\right)^{\frac{1}{2}} \int Q_{m,j} u^2 f du$
Excitation	$Q_{e,j}$	$\Delta E_{p,j}$	$\Delta E_{p,j} N_e N_j \left(\frac{2e}{m}\right)^{\frac{1}{2}} \int Q_{e,j} u f du$
Ionization	$Q_{i,j}$	$\Delta E_{p,j}$	$\Delta E_{p,j} N_e N_j \left(\frac{2e}{m}\right)^{\frac{1}{2}} \int Q_{i,j} u f du$
Attachment	$Q_{a,j}$	u^b	$N_e N_j \left(\frac{2e}{m}\right)^{\frac{1}{2}} \int Q_{a,j} u^2 f du$
Recombination	$Q_{r,j}$	u^b	$N_e N_j \left(\frac{2e}{m}\right)^{\frac{1}{2}} \int Q_{r,j} u^2 f du$
Superelastic	$Q_{s,j}$	$-\Delta E_{p,j}^c$	$-\Delta E_{p,j} N_e N_j \left(\frac{2e}{m}\right)^{\frac{1}{2}} \int Q_{s,j} u f du$

Power in per unit volume = $EJ_D = E_e N_e w$

^a Average energy transferred per collision

^b All of the electron energy is lost

^c Energy is returned to the electrons

TABLE II: KrF LASER SIMULATIONS
Both experiments were performed at Maxwell Laboratories, Inc. by R. O. Hunter [6]

EXPERIMENTAL PARAMETERS	EXPT 1	EXPT 2
Pumping mechanism	e-beam	e-beam sustained discharge
Total Pressure (atm)	1	2.01
Mix: Ar/Kr/F ₂	93.3/6.6/0.1	95.5/4.3/0.2
e-Beam Average Current Density (Amps/cm ²)	6	2
e-Beam Voltage (kilovolts)	300	400
Electrical Pulselength (nanoseconds)	500	500
Discharge Average Electric Field (KV/cm-atm)	--	2
Volume (liters)	60	30

RESULTS	EXPT	SIMULATION	EXPT	SIMULATION
Optical Output (Joules)	120	124.8	36	39.6
Average Optical Flux (Watts/cm ²)	7x10 ⁵	8.1x10 ⁵	7x10 ⁵	7.8x10 ⁵
Local Efficiency (%)	7.2	8.0	3	3.4
Discharge Enhancement Ratio	--	--	2.4	2.3
Total Absorption (% cm ⁻¹)	?	0.39	?	0.3
g _o /g _a (small signal gain/absorption)	6(?)	9.3	-4	3.31
Ionization Rate Ratio	--	--	?	0.136

TABLE III

EXPERIMENTAL PARAMETERS

Mixture	Ne/Xe/NF ₃ = 99.7/0.225/0.075
Total pressure	3.0 atm @ T = 300°K
Laser cavity length	150 cm
Laser gain length	100 cm
Mirror reflectivity	50%
Pump pulse length	1.1 μsec (e-beam and discharge)
E-beam energy deposited	40 J/ℓ (J _{eb} = 3 A/cm ²)
Discharge energy deposited	120 J/ℓ
Total pump energy	160 J/ℓ

RESULTS

<u>E-beam only</u>	EXPT	MODEL
Optical output	0.88 J/ℓ	0.99 J/ℓ
Local efficiency	2.2%	2.5%
<u>E-beam controlled discharge</u>		
Optical output	2.8 J/ℓ	3.7 J/ℓ
Local efficiency	1.75%	2.3%
Discharge enhancement	3.2:1	3.7:1

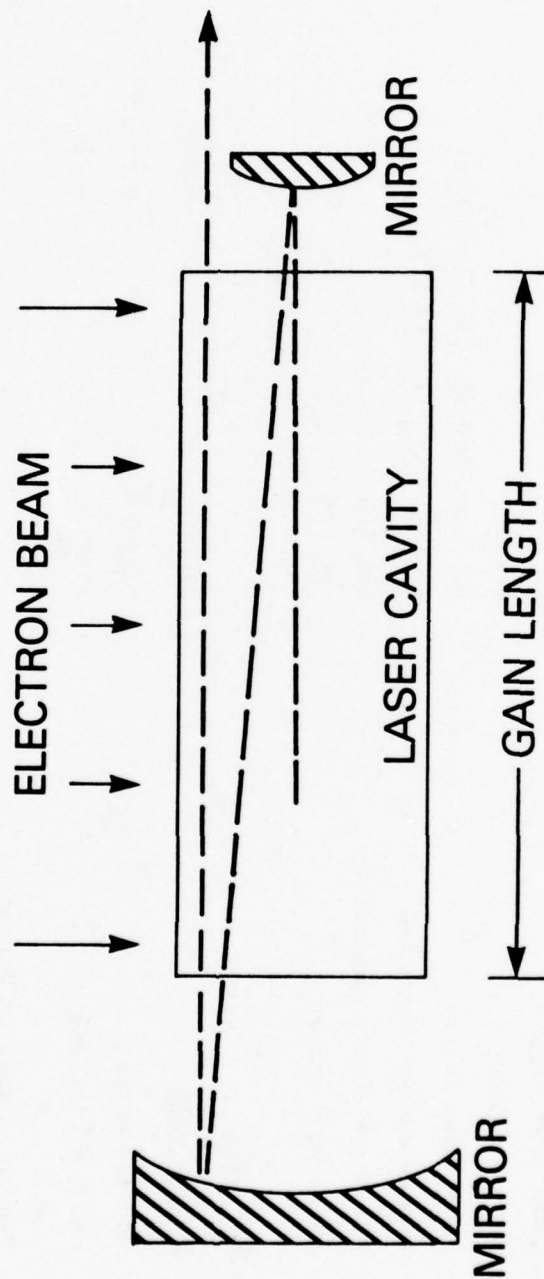


Fig. 1 - Example of direct-pumped laser geometry: The typical apparatus modeled here is simpler in form. Discharge sustainer voltage may be applied, e.g., into the page.

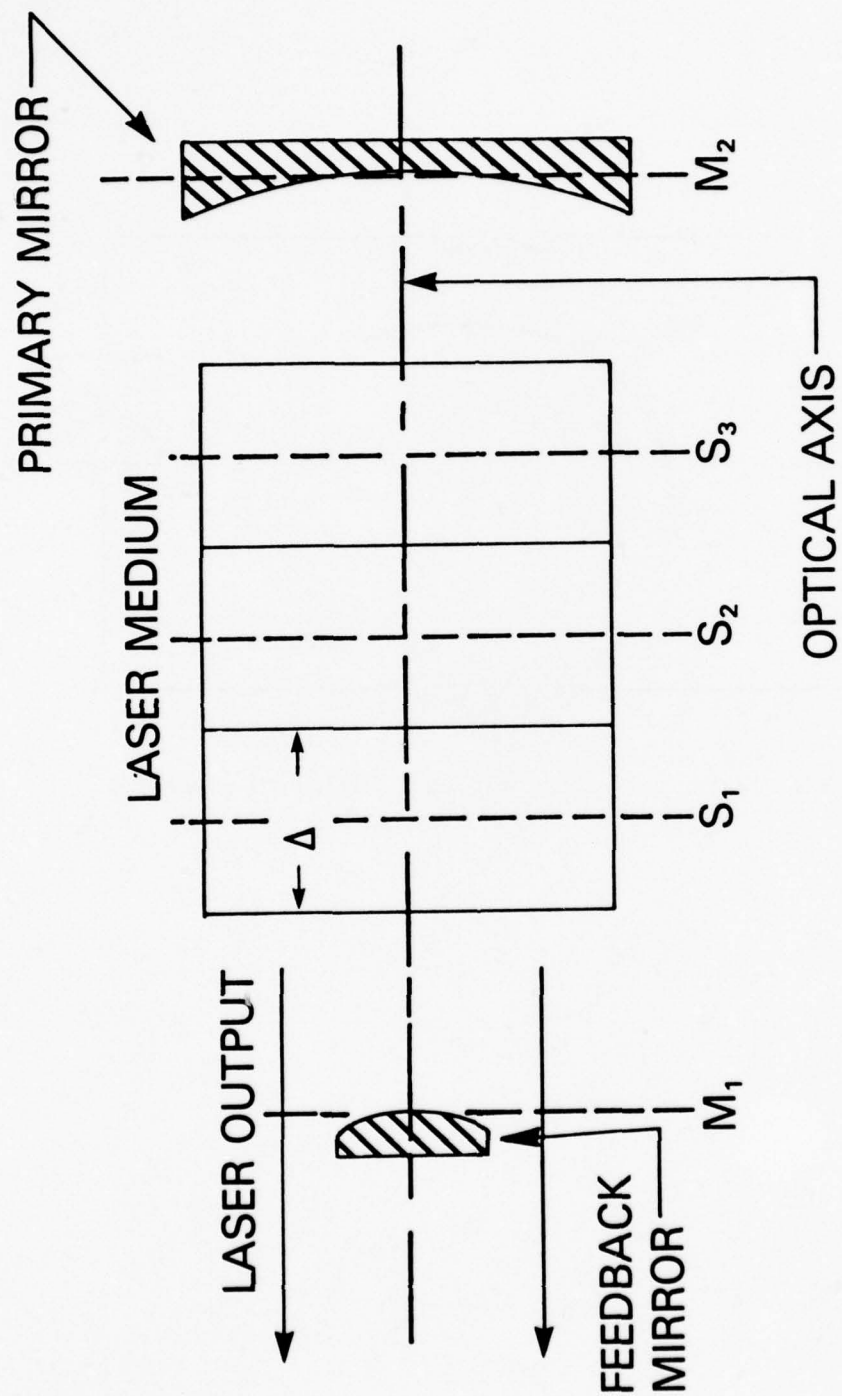


Fig. 2 - Zoning for optical resonator computations

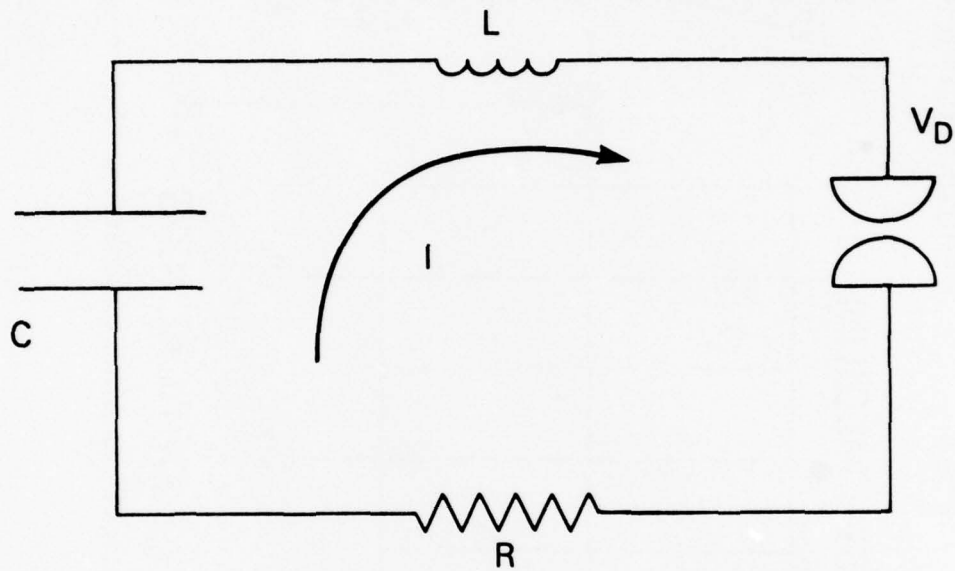


Fig. 3 - Diagram of an LRC circuit coupled to discharge

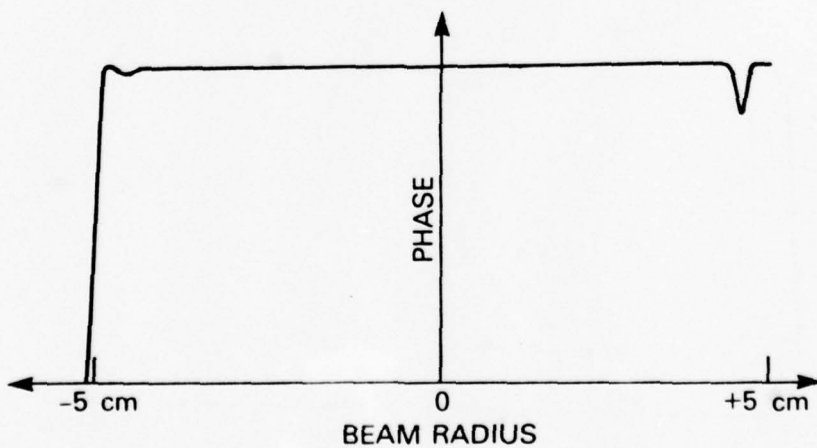
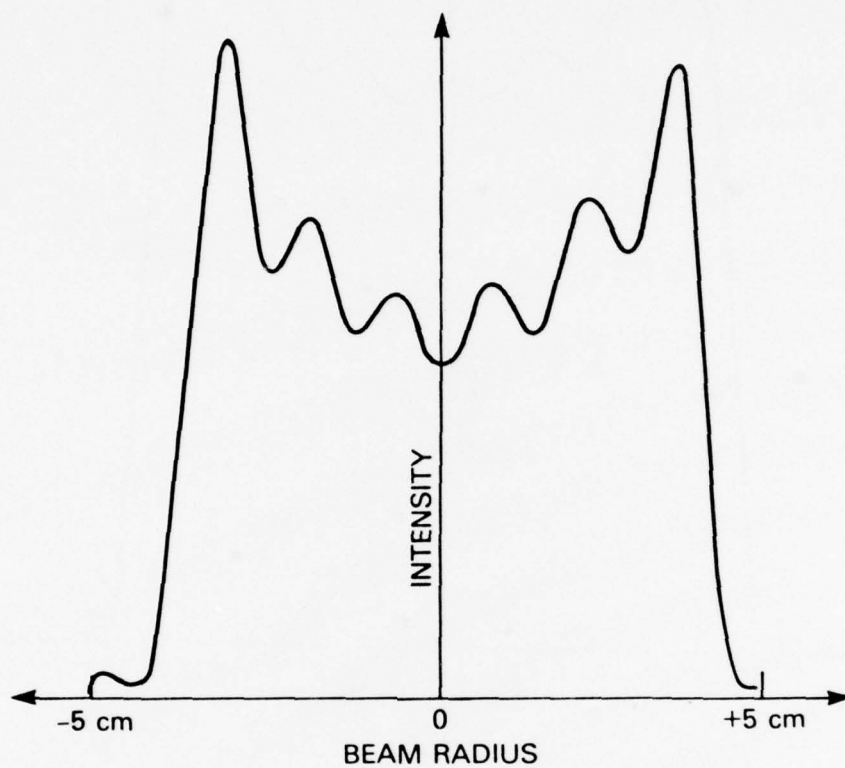


Fig. 4 - Intensity and phase distributions for AVCO e-beam pumped KrF laser

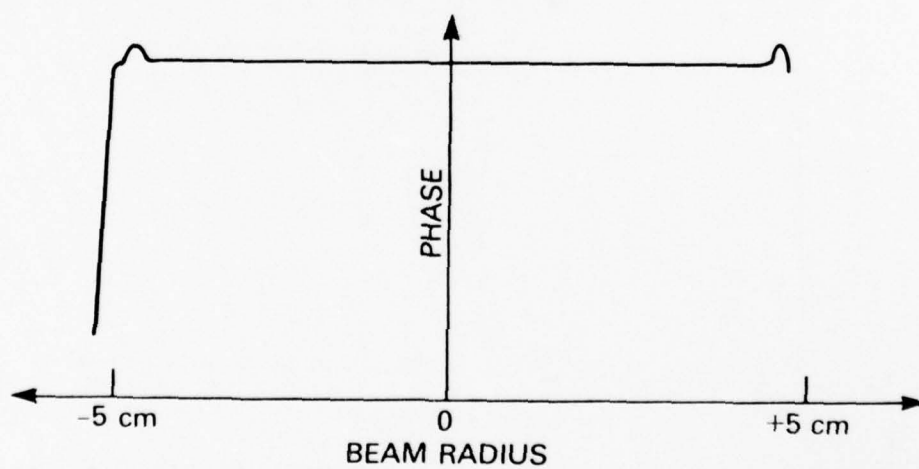
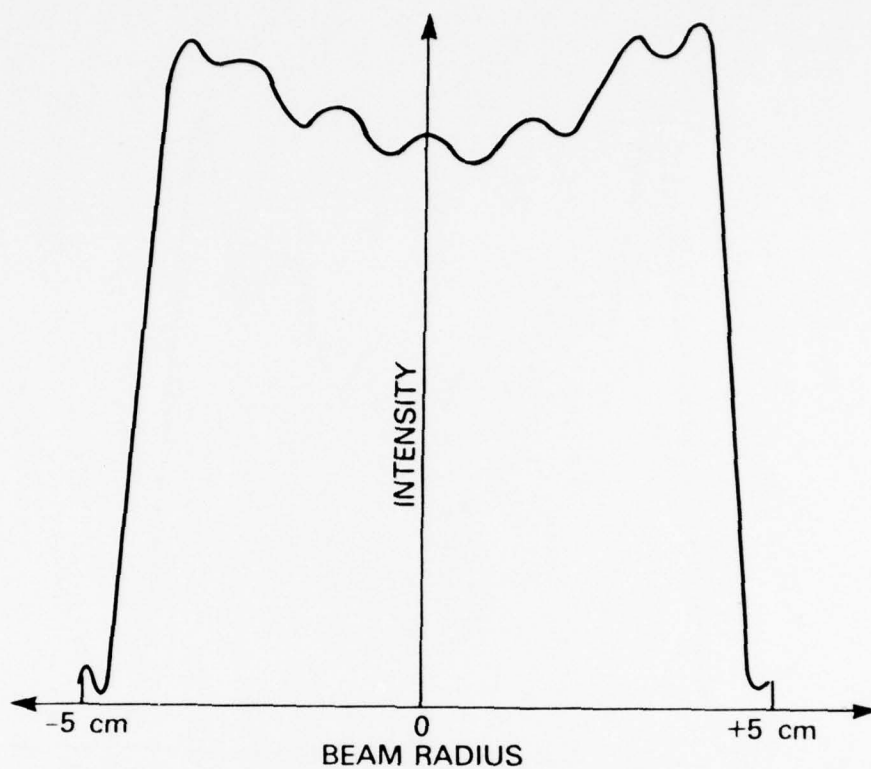


Fig. 5 - Intensity and phase distributions for Maxwell e-beam sustained discharge KrF laser

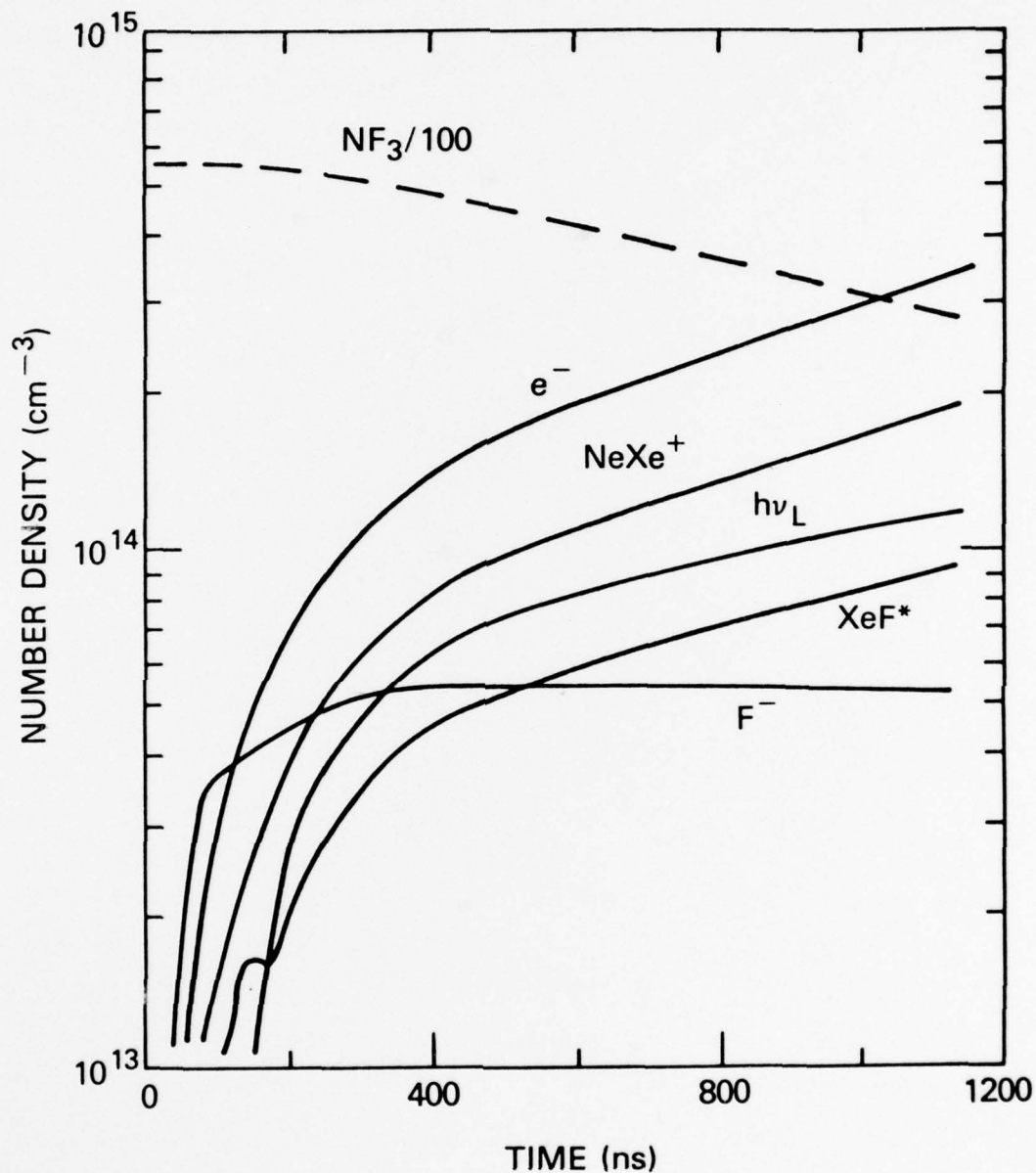


Fig 6 - Time history of number densities of selected species
in e-beam-controlled XeF laser simulation

ELECTRON-BEAM-CONTROLLED XeF LASER

Both experimental¹ and modeling² studies were undertaken during the past year to determine whether an electron-beam-controlled XeF laser would have any advantage over an electron-beam-pumped XeF laser for large-scale systems. We have been able to obtain comparable output powers and efficiencies from both systems experimentally. The significant difference between the two pumping schemes being that the optimum pressure of operation for the e-beam-controlled XeF laser was 3 atmospheres as compared to 5 atm for the e-beam-pumped XeF laser. On the basis of joules per liter-atm extracted energy, this represents an improvement of ~ 70%. Under optimum laser conditions, laser enhancements of 3.2:1 can be achieved in an applied electric field without sacrificing overall efficiency. In this mode of operation, ~ 75% of the input energy to the gas is supplied by the sustainer. These results indicate that, for comparable energy loading of the foil, the electron-beam-controlled XeF laser is capable of generating ~ 4 times the average output power density than is the electron-beam-pumped XeF laser. This can be achieved at comparable efficiency.

The most sensitive parameter for maintaining maximum output power, efficiency, and stable operation is the concentration of NF_3 .

Extensive numerical modeling using a time-dependent computer code has been conducted on the e-beam-controlled XeF laser in conjunction with

the experiments mentioned above. Excellent agreement between calculated results and measurements were obtained for both laser output and discharge stability.

The effect of the concentration of NF_3 on the stability of the discharge in Ne/Xe/NF_3 mixtures was investigated computationally for pump pulses in the microsecond range and it was shown that a significant depletion of NF_3 can occur at high pump-energy loadings for long pulses. Figure 1 shows computed number densities of selected species for an e-beam controlled XeF laser in which 120 J/l pump energy is supplied by the sustainer and 40 J/l is supplied by the e-beam. The gas mixture is $\text{Ne/Xe/NF}_3 = 99.7/0.225/0.075$ with a total pressure of 3 atm and the pump pulse duration is 1.2 μsec . Note that the NF_3 concentration is reduced to one-half its initial value after $\sim 1 \mu\text{sec}$. In this attachment-dominated discharge, the electron density ("e⁻" curve in Fig. 1) continually grows throughout the pulse as the main electron loss process (dissociative attachment to NF_3) diminishes with the depletion of NF_3 . After sufficient depletion of the attaching species, the growth rate of the electron density increases rapidly with time and discharge instability occurs.

Discharge instability has been observed experimentally and has been calculated by the model for slightly ($\sim 10\%$) higher applied electric fields and for slightly longer pulses than the conditions of Fig. 1. For large energy loading, a high electron density is required and thus high discharge enhancement lasers operate near the limit of discharge stability.

References

1. L. F. Champagne and N. W. Harris, "Characteristics of the Electron-Beam-Controlled XeF Laser," Appl. Phys. Lett. 33, 248-250 (1 August 1978).
2. L. J. Palumbo, "The Role of Electron Kinetics in Discharge-Pumped Rare-Gas-Halide Lasers," Paper E-2, 31st Annual Gaseous Electronics Conference, Buffalo, NY (October 1978).

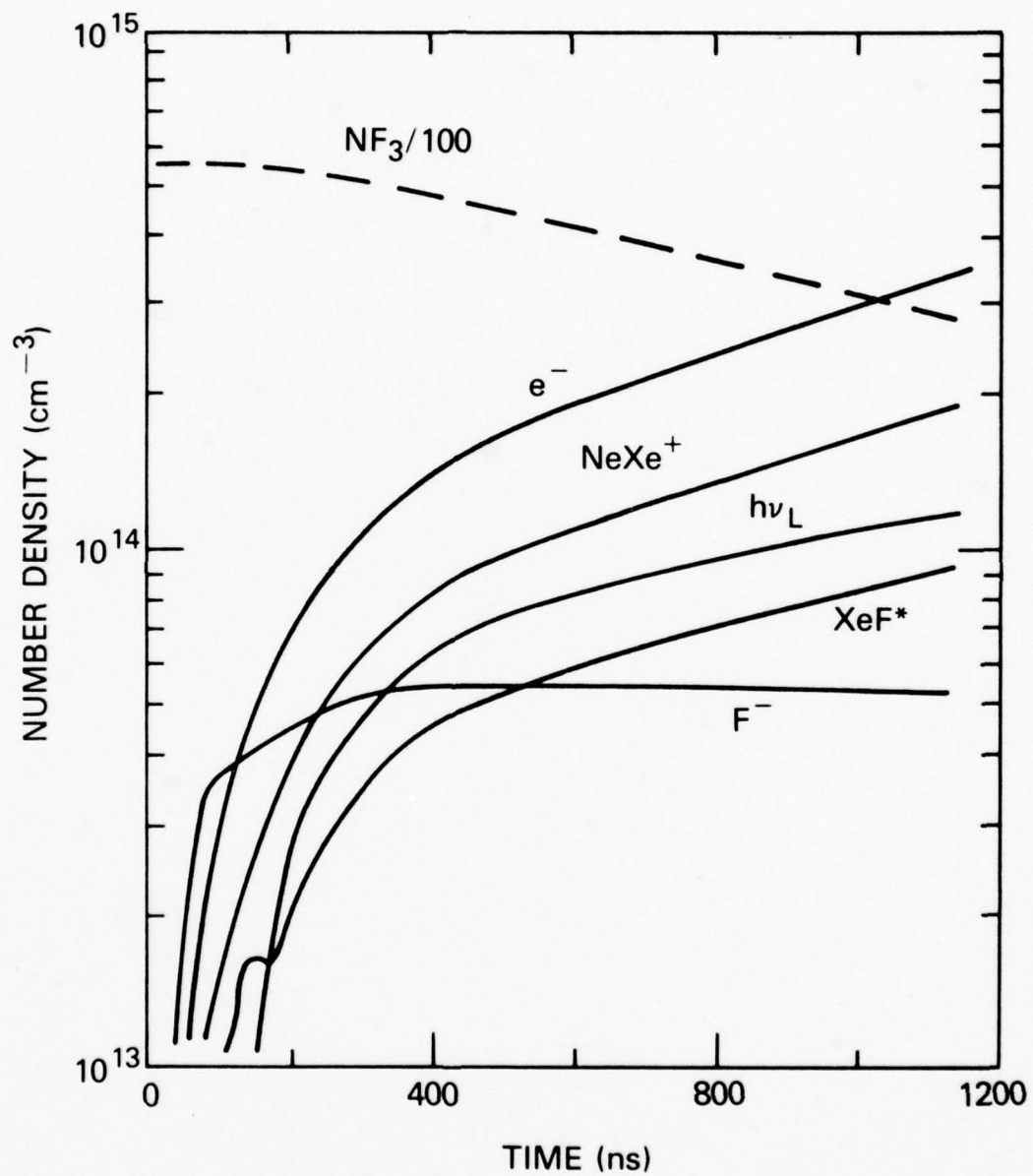


Figure 1. Time history of selected species in an e-beam-controlled XeF laser.

Characteristics of the electron-beam-controlled XeF laser^{a)}

L. F. Champagne and N. W. Harris^{b)}

Naval Research Laboratory, Washington, D.C. 20375

(Received 1 May 1978; accepted for publication 23 May 1978)

Output power and efficiency for e-beam-controlled operation which is comparable to e-beam-pumped operation is reported. Under optimum conditions laser enhancements of 3.2:1 can be achieved in the presence of an applied electric field at an overall efficiency of ~1.8%. In this mode of operation greater than 75% of the input energy to the gas is supplied by the sustainer. The concentration of NF_3 is the most sensitive parameter for maintaining maximum output power, efficiency, and stable operation.

PACS numbers: 42.55.Hq, 42.60.By, 42.60.Da

Efficient long-pulse operation of the e-beam-pumped XeF laser has been demonstrated.¹⁻⁵ The use of neon in place of argon has been shown to reduce significantly the transient optical absorption in the laser medium with consequent increases in efficiency and output power.³

Scaling of e-beam-pumped lasers to high average powers is limited by inefficiencies in e-beam generation, electron energy loss and subsequent heating of the electron-beam window (foil), and nonspecific conversion of the electron energy into desired excited states.

By contrast, e-beam-controlled lasers offer both the promise of converting electron energy directly into preferred excited states where most of the energy is deposited into the gas by the discharge and avoid the inefficiencies of e-beam production and transmission.

In this paper we discuss the operating characteristics of the e-beam-controlled XeF laser. We have been able to compare stable operation of the e-beam-controlled

XeF laser with the e-beam-pumped laser for the generation of 1- μ sec optical pulses. Similar output powers (2.8 J/l) and efficiencies (1.8%) were obtained. However, the optimum pressure was 3 atm rather than 5 atm used in the e-beam-pumped system. Under these conditions 75% of the energy input to the gas was supplied by the sustainer.

The experimental apparatus, which has been described in detail previously,¹ consists of a 1-m active length laser chamber with a 2.2-cm optical aperture. For e-beam-controlled operation a capacitor bank was connected to the laser anode by means of a pressurized gas switch. The switch prevented any electric field from being applied to the laser gas in the absence of an electron beam. In addition, a capacitor was attached to the laser anode to reduce the voltage change caused by the electron beam. These precautions were necessary as even a small electric field applied to the laser gas, in the absence of adequate e-beam pumping, would result in premature breakdown. The current generated in the laser gas by the applied electric field was monitored by a Pearson current transformer and the field itself was measured by a voltage divider connected directly to the laser anode. The optical characteristics of the

^{a)}Sponsored in part by DARPA.

^{b)}Present address: Ion Physics Corporation, Burlington, Mass. 01103.

discharge were measured with probe lasers. On line gain was measured with a discharge pumped XeF laser⁶ and absorption was measured on either side of line center with a rare-gas ion laser⁷ operating at 338 or 364 nm. The optical pulse from each probe laser was monitored with S-5 photodiodes both before and after probing the excited gas mixture. Laser energy coupled out of the resonator was monitored with a Gen-Tec ED-500 pyroelectric detector. In all cases, the laser was operated well above threshold so that it was possible to accurately observe the effect which small variations in the laser constituents (NF_3 and xenon) had on laser enhancement and discharge stability in the presence of an applied electric field.

The e-beam-controlled XeF laser operated in a pressure range 1–5 atm but the largest laser enhancement (ratio of output power in the presence of an applied electric field to output power with no electric field present) occurs at 3 atm. At higher pressures the output power and efficiency increase slightly but the laser enhancement falls from 3.2 to ~1.5 at 5 atm. At lower pressure the laser enhancement remains comparable but the output power and efficiency decrease dramatically.

At the optimum concentration ($\text{Ne}:\text{Xe}:\text{NF}_3$:: 99.7:0.225:0.075) and a 3-atm operating pressure, it was possible for the sustainer to deposit energies up to 3.2 times that deposited by the electron beam alone, which increased the laser output by a factor of ~3.2. These conditions corresponded to an energy deposition of 160 J l^{-1} . Laser enhancements as large as 3.5 to 1 could be achieved at slightly higher applied electric fields but the corresponding rise in sustainer current from 80 to 120 A cm^{-2} , significantly lowered the efficiency. This rapid rise in current was indicative of the onset of an instability. Increasing the applied electric field above $0.5 \text{ kV cm}^{-1} \text{ atm}^{-1}$ resulted in an optical pulse which terminated before the end of the pump pulse. The dependence of laser enhancement on electric field

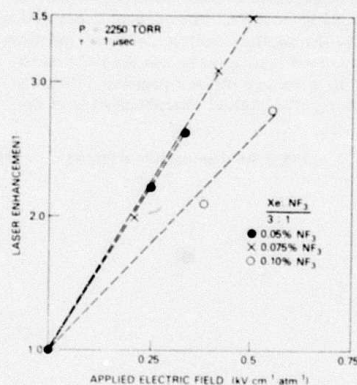


FIG. 1. Measured laser enhancement of a one microsecond optical pulse as a function of the applied electric field at differing percentages of xenon and NF_3 . The ratio of xenon to NF_3 is held constant (3:1).

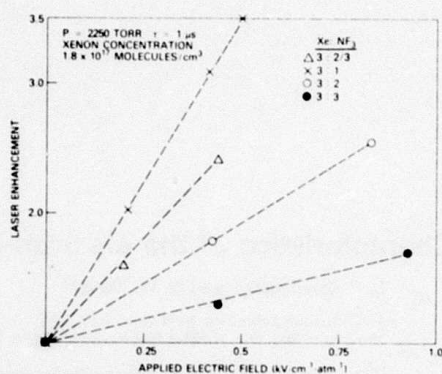


FIG. 2. Measured laser enhancement of a 1- μsec optical pulse as a function of applied electric field at various NF_3 concentrations. Xenon concentration is held constant.

and gas composition is shown in Fig. 1. It should be noted that the concentration which yields the best output power and efficiency for pure e-beam pumping is also best for e-beam-controlled operation. Increasing the xenon plus NF_3 concentration degrades the output power and efficiency. When the xenon plus NF_3 concentration is reduced, the output power for the 1- μsec optical pulse is not degraded. However, stable operation and the extraction of a 1- μsec optical pulse requires a lower applied electric field. Also, the sustainer current rises rapidly at all values of E/N thereby reducing the laser efficiency.

The small-signal gain was measured for conditions yielding the best efficiency. Here, the input energy was 160 J l^{-1} with a laser enhancement of 3.2 yielding a gain of $1.3\% \text{ cm}^{-1}$ and an efficiency of 1.8%. For the highest output power condition (input energy of 200 J l^{-1}), the small-signal gain was $1.85\% \text{ cm}^{-1}$, the laser enhancement 3.5, and the efficiency 1.5%. Background absorption for the optimum laser mixture at both input energies was measured to be $\leq 0.1\% \text{ cm}^{-1}$.

The operation of the e-beam-controlled XeF laser as a function of the minor constituent, NF_3 , is presented in Fig. 2, which shows a plot of laser enhancement as a function of applied electric field for various concentrations of NF_3 , at constant xenon concentration. In all cases the electric field was varied from zero to the onset of breakdown. As the concentration of NF_3 was increased, the maximum value of the applied electric field for which a 1- μsec optical pulse could be maintained also increased. However, the output power and laser enhancement decreased for this nonoptimum mixture. For the production of a fixed optical pulse length there is an optimum concentration of molecular halogen donor. Depletion of the molecular halogen donor species during the discharge, in this case NF_3 , limits the optical pulse length output power and efficiency which can be expected. This depletion also has an adverse effect on the stability of the discharge since the principal loss of electrons in the discharge is through electron

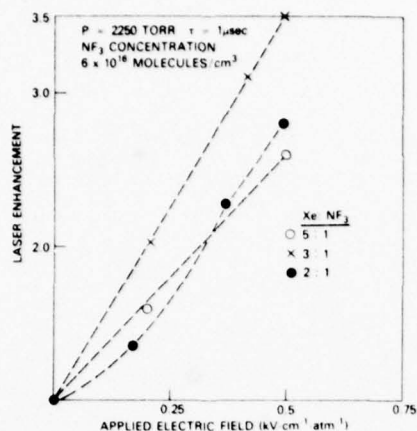


FIG. 3. Measured laser enhancement of a 1- μ sec optical pulse as a function of applied electric field at various xenon concentrations. NF_3 concentration is held constant.

attachment by the halogen donor. If we compensate for the depletion of the NF_3 by adding more NF_3 initially, then the excess of NF_3 leads to lower efficiency at the start of the pulse. That the NF_3 is depleted during the laser pulse is supported by the NRL modeling calculations. For the laser conditions which yield maximum output energy at maximum efficiency, a time-resolved analysis of the various constituents of the laser gas (ions, neutrals, electrons, radiation) indicates that in a 1- μ sec pulse the NF_3 is depleted by 50% from its initial value and the F^+ population is depleted to 33% of its maximum value by the end of the pulse.⁸

In Fig. 3 laser enhancement is plotted as a function of applied electric field for various xenon concentrations and a fixed concentration of NF_3 . Laser enhancement output power and efficiency decreased slightly as the ratio of xenon to NF_3 was increased. At reduced ratios of xenon to NF_3 the laser enhancement remained low for small electric field but rose rapidly at the higher

electric fields. Operation at the higher electric fields caused optical pulse distortion as the gain and output power rose rapidly during the pulse. In extreme cases, the optical pulse was terminated by an arc.

In conclusion, we note that the e-beam-controlled XeF laser is capable of more than three times the average output power density than is the pure e-beam-pumped XeF laser. Efficiencies are comparable. The connection between peak output power and pulse length is more complicated, depending not only upon the known relationship between pulse length and current density of modern electron guns^{9,10} but also upon the additional concentration of halogen donor molecules needed to compensate for their depletion during the pulse.⁸ However, these relationships are known and may be used to design XeF lasers for very high power levels.

The authors gratefully acknowledge the many helpful discussions with T.G. Finn and L.J. Palumbo and the technical assistance of R. DeLoatch, D. Shores, and K. Tayman.

¹L. F. Champagne, J. G. Eden, N. W. Harris, N. Djeu, and S. K. Searles, *Appl. Phys. Lett.*, **30**, 160 (1977).

²L. F. Champagne and N. W. Harris, *Appl. Phys. Lett.*, **31**, 513 (1977).

³L. F. Champagne and N. W. Harris, 1977 IEEE/OSA Conference on Laser Engineering and Application, Washington, D.C., 1977 (unpublished).

⁴J. H. Jacob, J. A. Mangano, and M. Rokni, 30th Annual GEC, Palo Alto, Calif., 1977 (unpublished).

⁵B. Forestier and B. Fontaine, 4th Colloquium on Electronic Transition Lasers, Munich, 1977 (unpublished).

⁶R. Burnham and N. Djeu, *Appl. Phys. Lett.*, **29**, 709 (1976).

⁷W. W. Simmons and R. S. Witte, *IEEE J. Quantum Electron.*, **QE-6**, 648 (1970).

⁸L. J. Palumbo and T. G. Finn (private communication).

⁹R. K. Parker, R. E. Anderson, and C. V. Duncan, *J. Appl. Phys.*, **45**, 2463 (1976).

¹⁰N. W. Harris, F. O'Neill, and W. T. Whitney, *Rev. Sci. Instrum.*, **48**, 1042 (1977).

ABSORPTION EXPERIMENTS RELEVANT TO THE XeF (B-X) LASER

The use of a probe laser whose output wavelength is known exactly has lead to the first observation of a narrow band absorption at one of the XeF (B-X) wavelengths. Ne^* may be the absorbing species.

Previous work¹ showed the presence of a high transient optical absorption in Ar/Xe/NF₃ laser mixtures. The substitution of neon for argon as the diluent gas was found to significantly reduce this absorption.² At the same time, ab initio calculations led Stevens to propose Ar_2^+ as the dominant absorber.³ In Ne/Xe/NF₃ mixtures laser performance was observed to be limited by the amount of xenon which could be added. For xenon concentrations $> \sim .2\%$ transient absorption attributed to Xe_2^+ limited laser performance.⁴ In this work we are once again attempting to improve the XeF laser performance through a better understanding of absorption processes which occur in e-beam irradiated discharges. The scope of the present work covers absorption at 4 amagats Ne at 20⁰, 150⁰C as a function of % Xe, % NF₃, λ near XeF λ , and current density.

The one meter e-beam device¹ used for room temperature work was modified to operate at 150⁰C. A cross sectional view of the modified laser chamber is shown in Fig. 1. Two stainless steel plates were added to thermally insulate the monel laser chamber. Stripline heaters were attached to the upper and lower surfaces of the laser chamber. An argon ion laser was used to probe the discharge. The argon ion laser

provides a line at 3511.13 Å which is close to the room temperature XeF lines, 3510.8 Å, doublet at 3511.5 Å, and 3512.6 Å.⁴ The closeness was demonstrated by a gain measurement of ~ 1.0%/cm (at a current density of 7 A/cm² at room temperature). Thus the unique wavelength of the argon ion laser makes this laser a better probe laser than an XeF laser.

Table I and Figures 2-4 present the data collected with the use of the argon ion laser at 3511.1 Å and other selected wavelengths. In addition, some data was taken with an XeF probe laser. Fig. 2 shows a strong narrow band absorption at 3511.1 Å in pure Ne. Previous work in Ar suggested a broad band absorption and it was assumed that the absorption in Ne would also be broad band. The discovery of this narrow band absorption suggests that laser modelling at 20°C should be performed on individual laser lines rather than lumping the lines together. A candidate absorber is Ne* (3s-4p) at 3510.72 Å.

Other data in this section was obtained to provide a better understanding of the magnitude of absorption as a function of temperature, composition, and pumping current density. The reduced absorption illustrated in Fig. 2 and 3 at 150°C explains at least some of the improved laser efficiency at 150°C. The intrinsic efficiency was measured to increase from 2.0% to 4.5%. Fig. 3 provides data which could be used to extrapolate to higher current densities. Table I gives some data on Ne/NF₃ mixtures. Altogether we have the beginning of an absorption data base to allow better assessment of the XeF (B-X) laser.

References

1. L. F. Champagne, J. G. Eden, N. W. Harris, N. Djeu and S. K. Searles, Appl. Phys. Lett. 30, 160 (1977).

2. W. S. Watt, L. F. Champagne and N. W. Harris, 7th Winter Colloquium on Quantum Electronics, Park City, Utah (1977).
3. W. J. Stevens, 7th Winter Collquium on Quantum Electronics, Park City, Utah (1977).
4. L. F. Champagne and N. W. Harris, Appl. Phys. Lett. 33, 248 (1978).
5. J. Goldhar, J. Dickie, L. P. Bradley, L. D. Pleasance, Appl. Phys. Lett. 31, 677 (1977).

TABLE I. SUMMARY OF ABSORPTION MEASUREMENTS
TAKEN AT 4 AMAGATS

<u>GAS</u>	<u>TEMP.</u>	<u>ABSORPTION</u>		<u>%/cm</u>	
		3511.1	3507.4	3637.8	3378 A ⁰
Ne	20 ⁰ C	2.6	.2	0.6	0.6
	150	0.55		<0.1	
Ne/Xe 99.5/0.5	20	0.35		~0.2	~0.2
	150	<.1			
Ne/NF ₃ 99.935/0.065	20	0.5		.13	

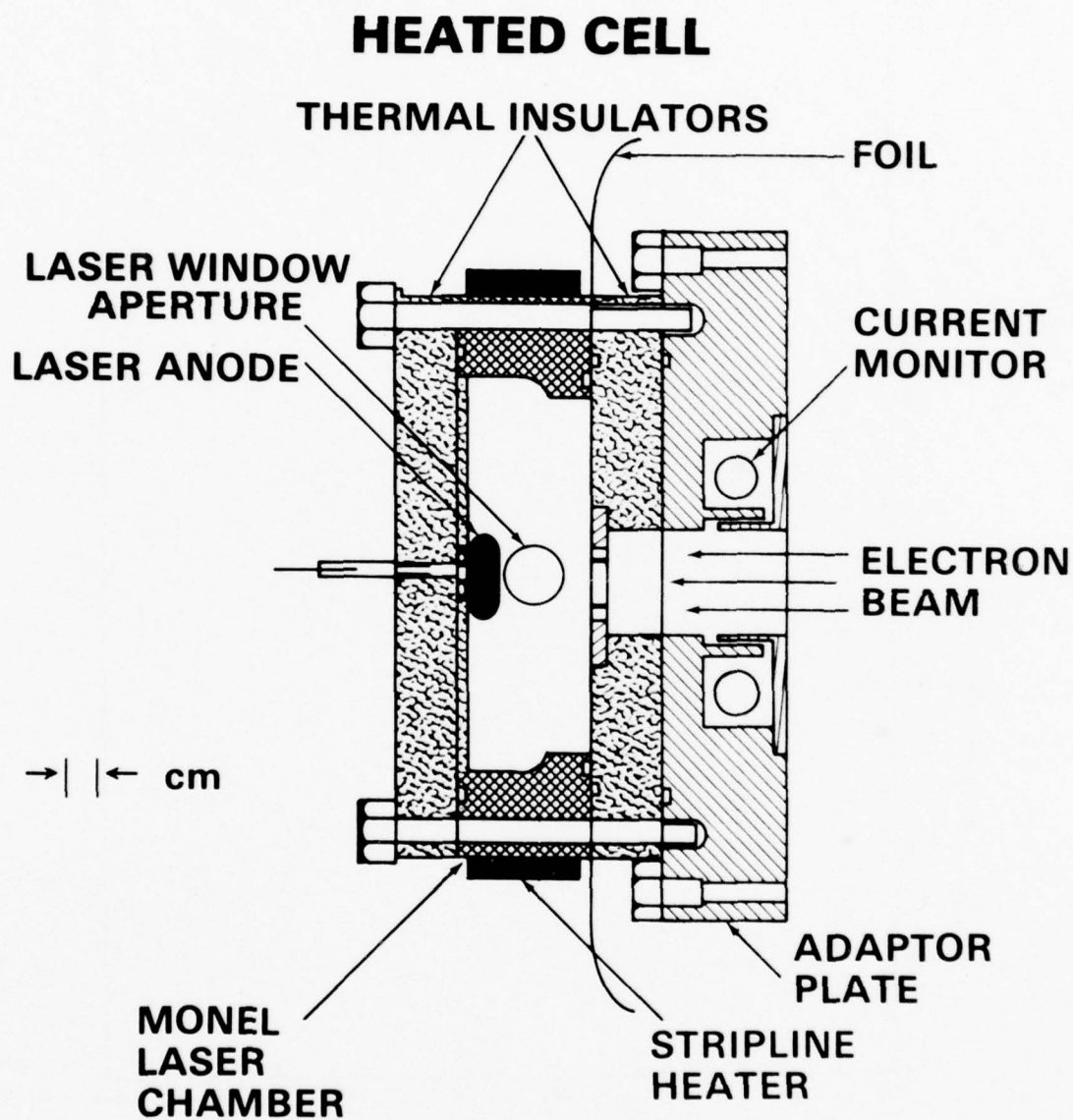


Fig. 1. Cross sectional view of the laser cell

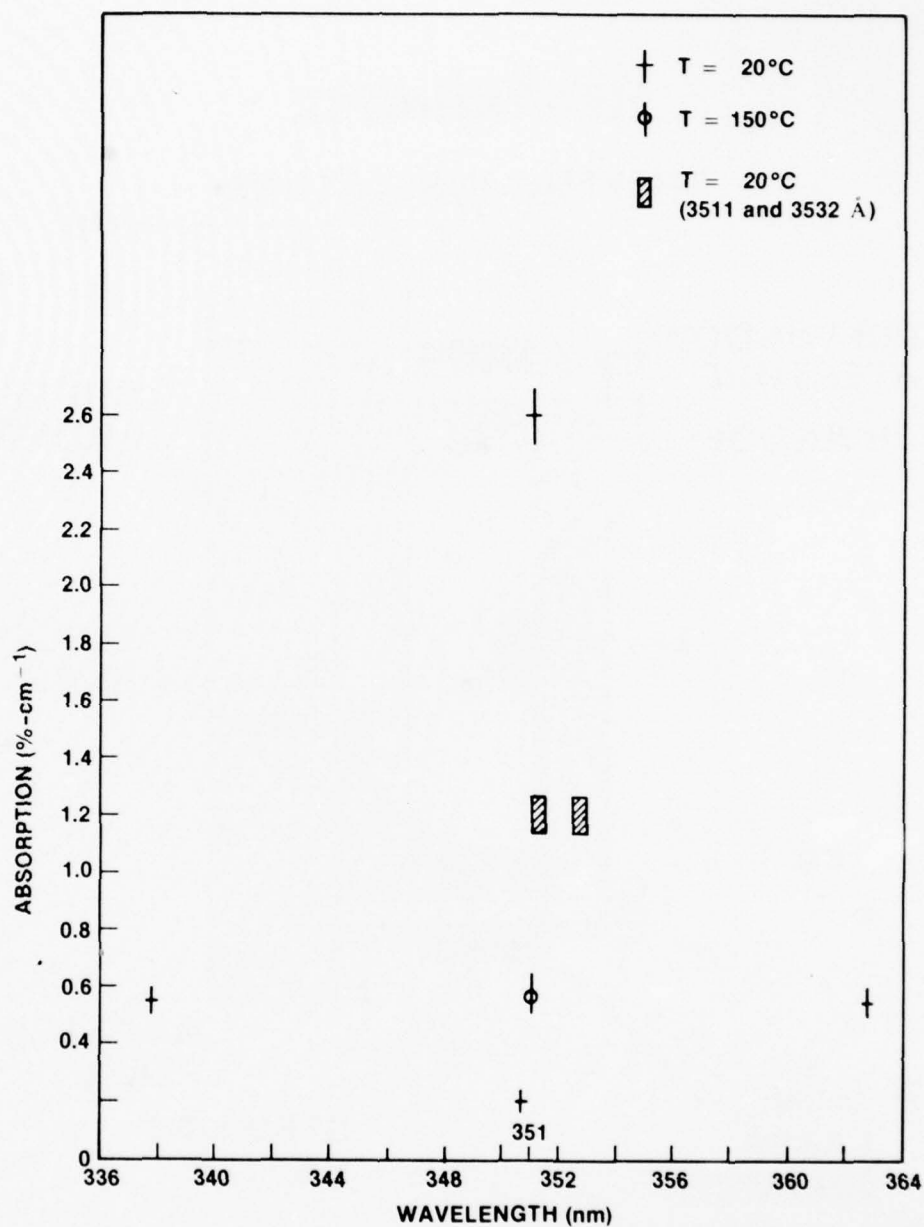


Fig. 2. Absorption in pure Neon at $7\text{A}/\text{cm}^2$

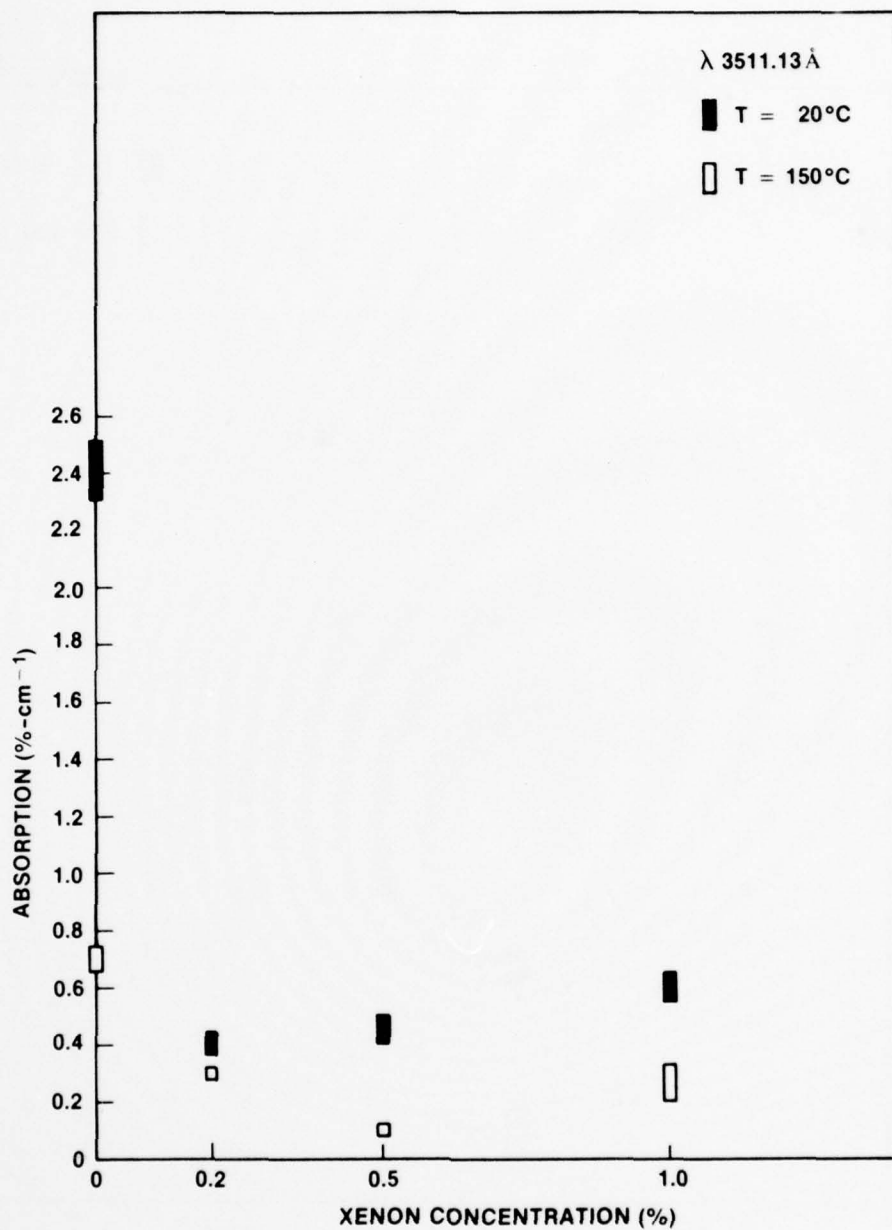


Fig. 3. Absorption as a function of Xe at 3511.1 Å⁰

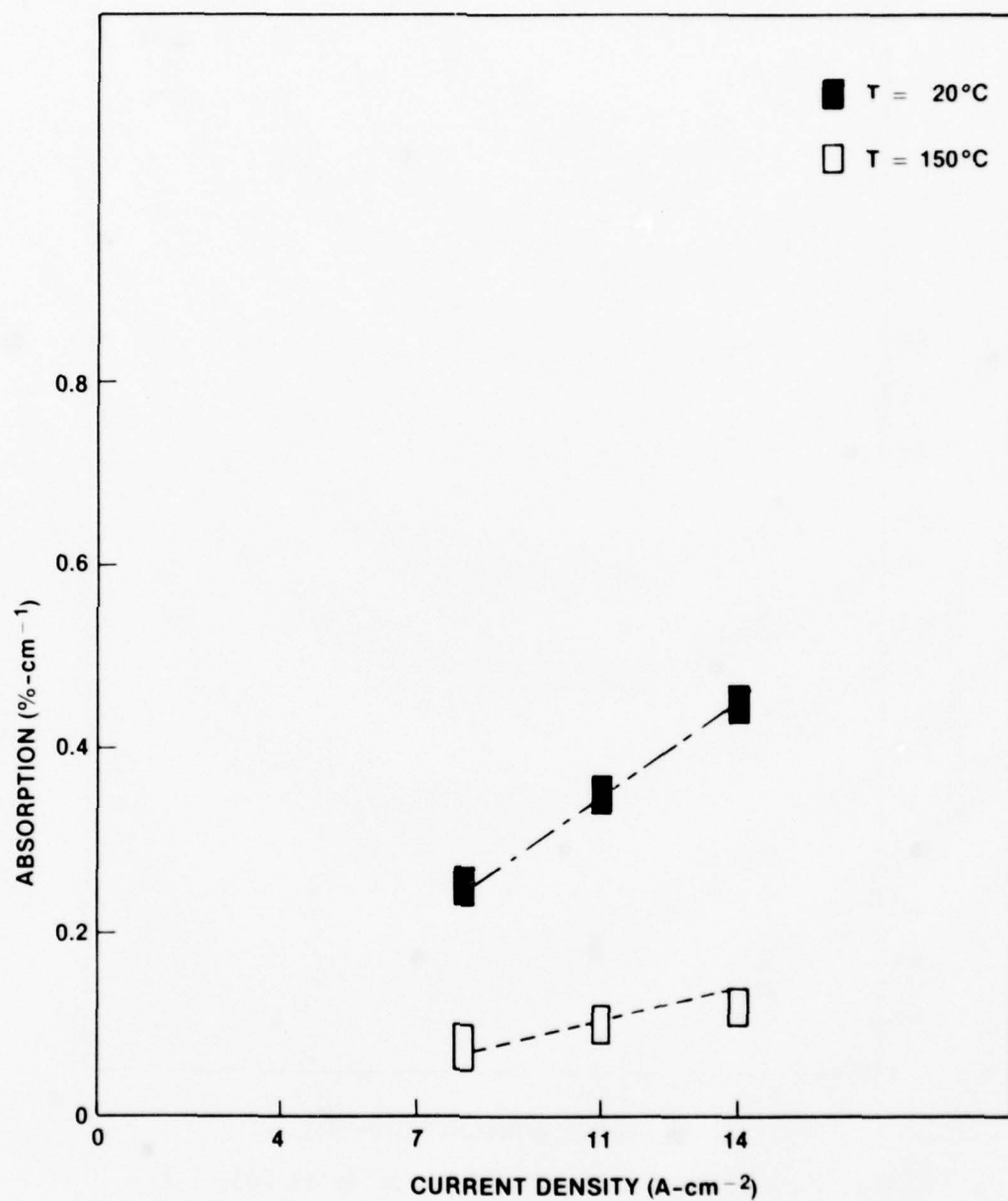


Fig. 4. Absorption in 99.5 Ne/0.5 Xe as a function of e-beam current density incident to the foil at 3511.1 Å

E-BEAM SUSTAINED MERCURY-HALIDE LASERS

Despite similarities in molecular configurations, mercury-halide lasers have not matched the rare gas-halides in efficiency. In order to further explore the experimental possibilities with the goal of improving the operation of the mercury-halide lasers, the following two experiments were undertaken. The first experiment investigated the use of HgBr_2 in an e-beam sustained discharge. Of course, the use of HgBr_2 avoids the problem of possible prereaction of Hg with the halogen donor. The second experiment was designed to assess the importance of the prereaction problem when using metallic Hg.

1. E-Beam Sustained Discharge Studies Using HgBr_2

A few grams of HgBr_2 crystals in two ceramic boats were placed inside the discharge chamber of the 40-cm-long e-beam device.⁽¹⁾ The chamber was operated at a temperature of $\sim 150^\circ\text{C}$ to produce a HgBr_2 vapor pressure of ~ 3 torr. The blue-green fluorescence output was optimized while the discharge excitation conditions and Ar/N_2 concentrations were varied. For a given mixture, it was found that the fluorescence efficiency increased with discharge E/N in the range of 2 to $4 \times 10^{-16} \text{ V cm}^2$. The highest E/N ratios were obtained at the lowest values of e-beam current density ($< 0.1 \text{ A/cm}^2$) consistent with maintaining discharge stability. Although use of N_2 concentrations higher than 10% allowed higher E/N ratios to be obtainable without arcing, the

fluorescence efficiency was found to decrease.

Various sustainer configurations were used including pulse forming networks (pfm) approximately matched to the discharge impedance ($\sim 1 \Omega$). However, the use of a pfm did not prevent the occurrence of discharge arcs but only served to limit the peak current in the event that an arc occurred.

The maximum fluorescence efficiency measured using Ar/N₂/HgBr₂ mixtures was $\sim 0.16\%$. Addition of a few torr of Hg vapor to this mixture caused the fluorescence efficiency to decrease.

The maximum laser output was ~ 3 mJ using a 16% transmission output mirror. The active volume was $\sim 30 \text{ cm}^3$ giving a specific laser output of ~ 0.1 J/liter. The discharge energy input was ~ 225 J/liter giving a conversion efficiency of $\sim 0.04\%$. The energy input from the e-beam was negligible.

For comparison, the fluorescence efficiency of a XeCl laser mixture was measured using the same setup. The fluorescence efficiency using only e-beam excitation was $\sim 10\%$ and the discharge efficiency was $\sim 0.8\%$.

2. Mercury-halogen Ground-state Reaction Study

An important question to be answered concerning the operation of HgX (X = Cl, Br, I) lasers starting with metallic mercury and the molecular halogens is: "How fast do the constituents react with each other in the ground state?" The specific question to be answered here is: "Is the halogen concentration severely depleted by prereaction with mercury vapor (or with the chamber walls) before the excitation can be applied?" To answer this question, an optical absorption technique was used to monitor the concentrations of Cl₂ and Br₂ in the

presence of metallic Hg both at room temperature and at a laser operating temperature of 150°C. To assure a saturated Hg vapor pressure, a ceramic crucible containing several cm³ of Hg was placed within the laser discharge chamber. At 150°C, the Hg equilibrium concentration is $\sim 6.4 \times 10^{16} \text{ cm}^{-3}$. A halogen concentration of $1.74 \times 10^{17} \text{ cm}^{-3}$ in an argon diluent was used. These concentrations were found to be near optimum for HgCl laser operation. All tests were conducted at 1 atm total pressure in order to obviate effects of possible leaks.

A chopped white light source was monitored through the 65 cm long optical path of the laser chamber with a monochromator-photomultiplier (PM) combination. The PM output was fed into a lock-in amplifier and then into a strip chart recorder.

The Cl₂ concentrations were monitored using a narrow wavelength region centered at 350 nm, and for Br₂, a narrow region centered at 420 nm was used. After passivations, the measured room temperature optical absorptions agreed well with published data (cf. Photochemistry, Calvert & Pitts, pp. 184 and 226). As shown in Figs. 1 and 2, the disappearance of the halogen was a very slow process at room temperature. It had also been determined, in preliminary tests without mercury in the chamber, that both halogen half-lives were ≥ 3 min at 150°C. So thus, although reactions with the chamber walls are important, they are not a limiting factor.

However, as seen in Fig. 1, at a chamber temperature of 150°C and in the presence of Hg vapor, Cl₂ had a half-life of only ≥ 1 minute. More important is the initial rapid reaction of Br₂ with the available

Hg vapor as seen in Fig. 2. The dashed curve portions correspond to the few seconds it takes to open a valve to admit the halogen-argon mixture to the chamber. The missing Br_2 concentration corresponds closely to the initially present Hg concentration. After the initial cleanup, the Br_2 concentration continues to fall with a half-life of ≥ 2 min after the first half-minute. This latter rate probably corresponds with that of additional Hg vapor becoming available out of the reservoir. In summary, the ground state reaction of metallic Hg with molecular Cl_2 is relatively slow, but with molecular Br_2 is extremely fast.

The rapid cleanup of molecular Br_2 explains the low fluorescence output obtained from the e-beam sustained discharge. This information also serves to explain the quite different results obtained in the uv pre-ionized discharge system. To review these results: the best halogen donors were found to be the dihalides of mercury. However, it was found that molecular bromine also worked quite well, but molecular chlorine did not. It is apparent now that the molecular bromine reacted with the available mercury vapor to form the dihalide which was then dissociated in the discharge to form the HgBr B-state.

To further test this theory, molecular Br_2 was used in the e-beam sustained system with the same excitation conditions as were used for HgBr_2 mixtures, i.e., with e-beam current densities of $< 0.1 \text{ A/cm}^2$. Indeed, it was found that the fluorescence output starting with molecular Br_2 and metallic Hg was then comparable with the results starting with crystalline HgBr_2 .

Since the reaction of Cl_2 with Hg is not as rapid, the question

still remains as to why our efficiency results are not as high as those reported by Maxwell and AVCO. We intend, however, to restudy the Hg + Cl₂ system under flowing conditions and also to try lower e-beam currents. We will also try Kr as a diluent gas because its use will avoid the Penning reaction between metastable Ar and Hg which may be responsible for premature discharge instabilities.

Incidentally, the detrimental effect of N₂ on the Hg* + Cl₂ system can be understood now with the recent measurements by Wodarczyk and Harker at Rockwell on the reactive quenching of metastable Hg (6 ³P₀) atoms by molecular chlorine. They determined the quenching cross-section to be 28 Å² and that the HgCl (B²Σ_{1/2}⁺) state is formed in only 1% of the reactive collisions. Thus, the Hg (³P₀) state is much less effective than either the (³P₂) or (³P₁) states in forming the HgCl(B) state, even though the reaction is also exothermic. Since Hg (6 ³P₁) atoms (and probably (6 ³P₂) atoms as well) are rapidly quenched by nitrogen to form the (6 ³P₀) state, less of the HgCl(B) state is formed.

Reference

1. W. T. Whitney, "Sustained Discharge Excitation of HgCl and HgBr B ²Σ_{1/2}⁺ → X ²Σ_{1/2}⁺ Lasers," Appl. Phys. Lett. 32, 239 (1978).

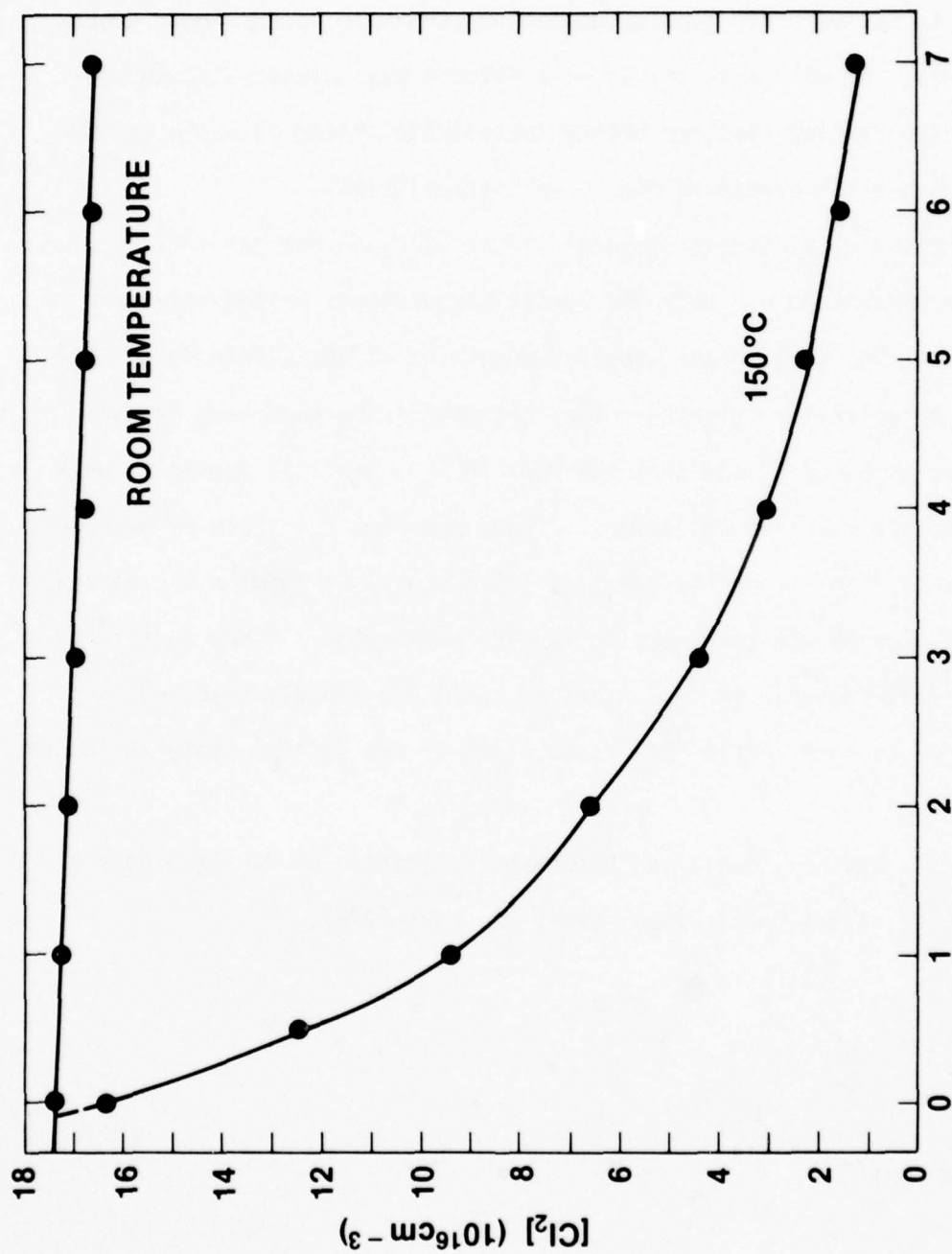


Fig. 1. Prereaction of Cl_2 with Hg vapor

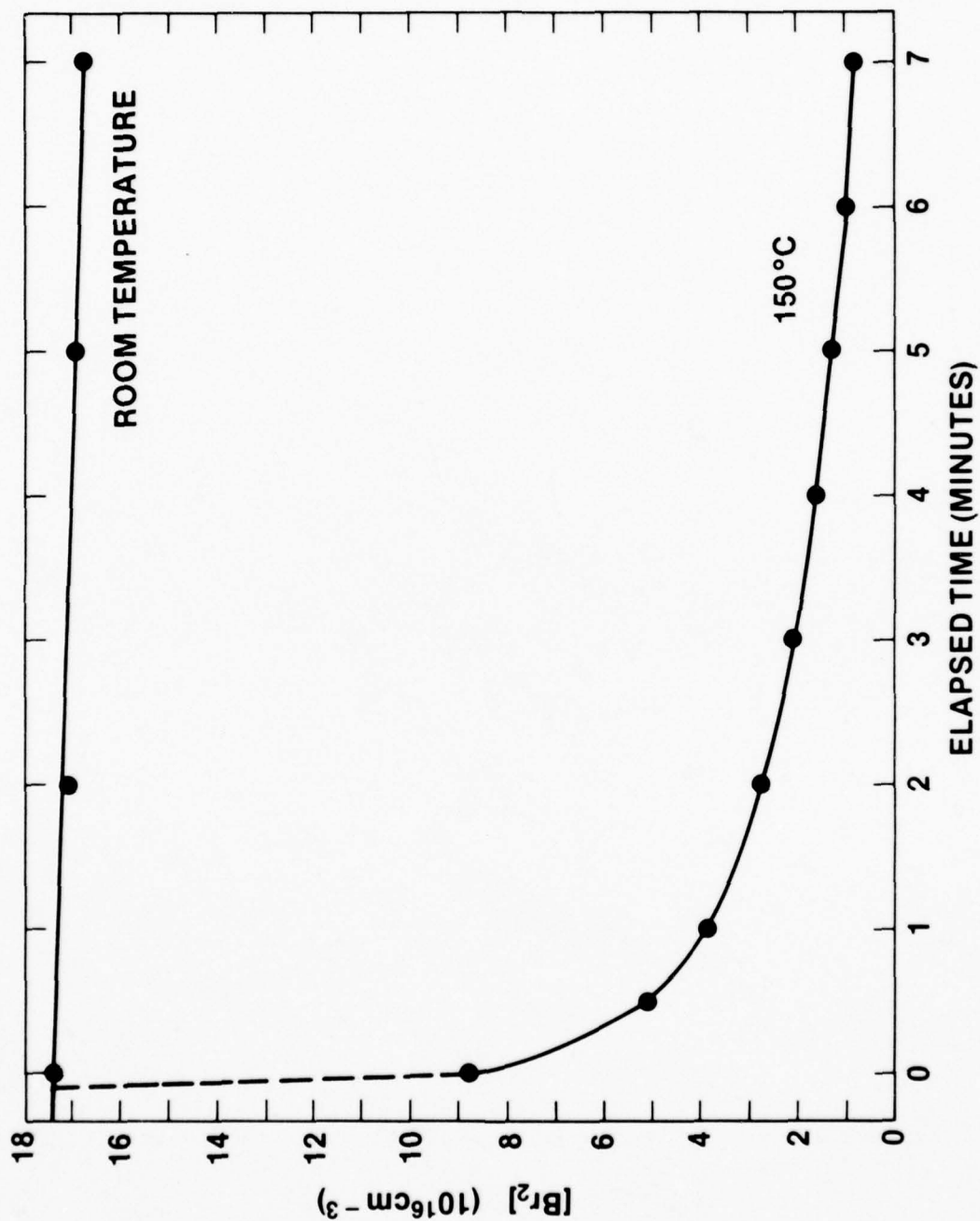


Fig. 2. Prereaction of Br_2 with Hg vapor

PHOTOLYTIC PUMPING OF RARE GAS-AND MERCURY HALIDE LASERS

Several diatomic molecules which radiate in the ultraviolet (UV) or vacuum ultraviolet (VUV) have excellent fluorescence efficiencies (>10%) but operate poorly as lasers. For some time now it has been recognized that these radiators are potentially efficient optical pump sources for UV and visible lasers. In fact, one of the prime candidates for the laser driver for a thermonuclear fusion reactor has been the $\text{Se}(^1\text{S} \rightarrow ^1\text{D})$ laser which is pumped by photodissociation of OCSe by Xe_2^* fluorescence.¹ The Xe_2^* excimer was chosen as the optical source due to the large fluorescence efficiencies (~50%) projected both experimentally² and theoretically³ for this molecule. During the last eight months, NRL has been investigating the possibility of using rare gas excimer fluorescence to photolytically pump rare gas- and mercury-halide molecular lasers. There are several attractive aspects of this pumping technique, particularly for DARPA applications:

- 1) The pumping quantum efficiency is high due to the large RG_2^* fluorescence efficiencies and the selectivity of the excitation mechanism;
- 2) The high pressure pump region is physically separated from the relatively low pressure active medium. Therefore, the operating parameters for both the pump and active medium can be optimized separately;
- 3) The low pressure of the active medium (≤ 1 atm) may ease

the acoustic problems (shock waves) that are normally encountered in high power, high pressure gas lasers;

4) The active medium is electron free and so upper laser level population losses due to collisions with electrons will be eliminated, and

5) Photodissociative pumping may reduce the optical absorption of the active medium due to the small number of fragments produced by the excitation process.

Figure 1 is a schematic diagram of the pumping process used to create $\text{XeF}^*(\text{B})$ molecules by photodissociation of XeF_2 . Upon absorbing a VUV photon, an XeF_2 molecule is electronically excited to an unstable XeF_2^* state which rapidly (< 1 ns) dissociates, forming an $\text{XeF}(\text{B})$ molecule and an F atom fragment. Due to the strength of the XeF-F bond and the 7.2 eV energy of a 172 nm photon, the $\text{XeF}(\text{D}) + \text{F}$ exit channel is inaccessible to the photodissociation process. For this reason, the quantum efficiency for producing $\text{XeF}(\text{B})$ molecules by VUV photodissociation of XeF_2 has been estimated by Brashears and co-workers⁴ to be unity.

Figure 2 shows the experimental apparatus used to study photodissociative rare gas- and mercury-halide lasers. A 450 keV, $\sim 1 \text{ kA-cm}^{-2}$ beam of electrons is used to transversely excite 5000 Torr ($\sim 6.5 \text{ atm}$) of xenon gas which is contained in a cylindrical steel cell. A Suprasil quartz tube, which has a transmission of $\sim 85\%$ at 172 nm, is positioned along the axis of the xenon steel cell. Therefore, the Xe_2^* VUV radiation produced in the outer jacket enters the quartz tube, photolyzing 0.5-3 Torr of XeF_2 . Several hundred Torr of He are also admitted to the quartz tube to equilibrate the XeF^* vibrational manifold.

The XeF (B \rightarrow X) spontaneous and laser emission spectra obtained from this device are shown in Fig. 3. Dominant fluorescence originates from the low-lying $v' = 0$ and 1 levels although some emission out to 330 nm is observed. When high reflectivity dielectric mirrors are positioned around the quartz tube, laser oscillation is achieved as shown in the lower two traces of Fig. 3. It is also evident that by varying the He background pressure, one has control over the dominant laser line and so a small amount of line-tunability is available.

The quantum efficiency of the XeF photodissociation laser is

$$N_{\text{max}} \approx \frac{1}{2} \left[h\nu(351\text{nm})/h\nu(172\text{nm}) \right] \approx 24\%$$

where the fluorescence efficiency of e-beam excited Xe_2^* molecules is taken to be 50%. In the future it is planned to investigate the efficiency obtainable in this device, possibly using cylindrical e-beam excitation to more uniformly irradiate the xenon gas. By varying the output coupling of the laser resonator and using N_2O calorimetry to accurately measure the Xe_2^* radiative energy incident on the XeF_2 , the efficiency and absorption processes affecting the performance of this laser may be ascertained. Studies of the relaxation of various XeF(B) vibrational levels could also be conducted by photolyzing XeF_2 at low pressure.

A similar approach has been used to obtain lasing in the green from the HgCl molecule. The laser spectrum (shown in Fig. 4) differs from the high pressure e-beam pumped Ar/Xe/Hg/ CCl_4 experiments in that the 558.4 nm line (corresponding to the $v' = 1 \rightarrow v'' = 23$ transition of the B \rightarrow X band) dominates over the usual 557.6 nm transition.

The same experimental apparatus was used to determine the HgCl ($B \rightarrow X$) radiative transition probability. To do this, HgCl_2 was irradiated by ArCl^* 175 nm spontaneous emission and the radiative decay of the HgCl^* fluorescence was recorded. As shown in Fig. 5, the HgCl^* population decayed exponentially over several time constants. By plotting the exponential decay constant (for a given $[\text{HgCl}_2]$) versus the HgCl_2 concentration (cf. Fig. 6), the $\text{HgCl}^*(B)$ radiative lifetime was determined to be 22.2 ± 1.5 ns.

The results achieved with the HgCl laser suggest that a photo-dissociative HgBr^* laser pumped by Xe_2^* radiation may be possible. Such a laser may be line-tunable over a limited wavelength range in the blue-green.

E-Beam Pumped IIB Metal-Halide Gas Mixtures

In our report of April, 1978, we described the completion of the first stage of a program to determine the feasibility of obtaining lasing on the $B \rightarrow X$ band of the cadmium and zinc-halide molecules. Intense Cd^* and Zn^* emission had been obtained from e-beam pumped Ar/Xe/Cd (or Zn) mixtures where the metal vapor comprised ~ 0.1 - 0.5% of the total mixture pressure. These results were in agreement with the close coincidence between various energy levels of Xe^* and Xe_2^* and excited states of Zn and Cd . It was suggested that this energy transfer mechanism could lead to ZnX or CdX lasers more efficient than the already demonstrated HgCl and HgBr systems.

Since that time, a wide range of experiments in Ar/Xe/Cd (or Zn)/halogen donor gas mixtures have been conducted. A new oven and laser cell, which are shown schematically in Fig. 7, were constructed to

enable metal vapor pressures up to several hundred Torr to be obtained. The oven enabled operation up to 700°C to be readily achieved and the main feature of the heated cell is that the windows were re-entrant and the lab air on the exterior face of the window could be evacuated to eliminate metal condensation on the window.

The result of these experiments is that although large concentrations ($10^{14} - 10^{15} \text{ cm}^{-3}$) of $\text{Zn}^*(^3\text{P})$ or $\text{Cd}^*(^3\text{P})$ could be created by rare gas-metal energy transfer, formation of the desired metal halide molecule was not demonstrated. Apparently, the pre-reaction problems that have been encountered at ~ 200°C in HgCl laser mixtures are much more severe (as would be expected) at the 400 - 700°C operating temperatures encountered here. Pre-reaction is so fast that even with flowing the gas mixture, no molecular emission was observable. Upon removing the halogen donor (such as CCl_4) from the gas stream, the metal atomic emission again became strong. A wide variety of halogen donors were tested in an unsuccessful attempt to find one with a halogen bond strong enough to withstand the high temperatures.

For this reason, we have begun to look at several diatomic metal vapor molecules where mercury is one of the atoms composing the molecule. In particular, the purpose of the project is to determine the feasibility of populating (in e-beam excited gas mixtures) a low-lying metal vapor excited state that is connected to ground by a strong optical transition. In the presence of a large ($10^{19} - 10^{20} \text{ cm}^{-3}$) background Hg concentration, this fast atomic transition should be perturbed strongly by the formation of a bound diatomic molecule. The reason for investigating such systems is to find a bound-free (dissociative) laser system with a

relatively large stimulated emission cross-section. The dissociative molecules under study by DOE, for instance, such as CdHg have stimulated emission cross-sections on the order of 10^{-19} cm^2 .

One of the prime candidates to be studied is the magnesium-mercury molecule. Although not shown in Fig. 8, the 1P level of Mg is connected to ground by a resonant transition at 285 nm. Perturbation of this level by Hg could result in bound-free emission for $\lambda > 320 \text{ nm}$ in the UV. The emission profile of this molecule would be homogeneously broadened and thus an ideal candidate for a tunable laser. To pump the MgHg^* excited state, it is obvious that the $\text{N}_2(\text{A})$ state vibrational manifold overlaps various Mg^* excited states. Therefore, Ar/ N_2 /Mg gas mixtures may be effective in efficiently populating these levels which are, in turn, optically connected to the 1P_1 state.

In conclusion, photolytic pumping of the XeF and HgCl lasers has been demonstrated. Studies of the potential efficiencies and limitations of these lasers are ongoing. Also, although spontaneous emission from the ZnX^* and CdX^* molecules in e-beam excited Ar/Xe/Zn (or Cd)/halogen donor gas mixtures has not been observed, an oven-laser cell combination that is ideal for the study of several metal molecules has been constructed and tested.

References

1. J. R. Murray and C. K. Rhodes, J. Appl. Phys. 45, 5041 (1978).
2. E. E. Huber, Jr., D. A. Emmons, and R. M. Lerner, Opt. Comm. 11, 155 (1974).
3. D. C. Lorents, Physica 82C, 19 (1976).

4. H. C. Brashears, Jr., D. W. Setser and D. DesMarteau, Chem. Phys. Lett. 48, 84 (1977).

PUMPING SCHEME

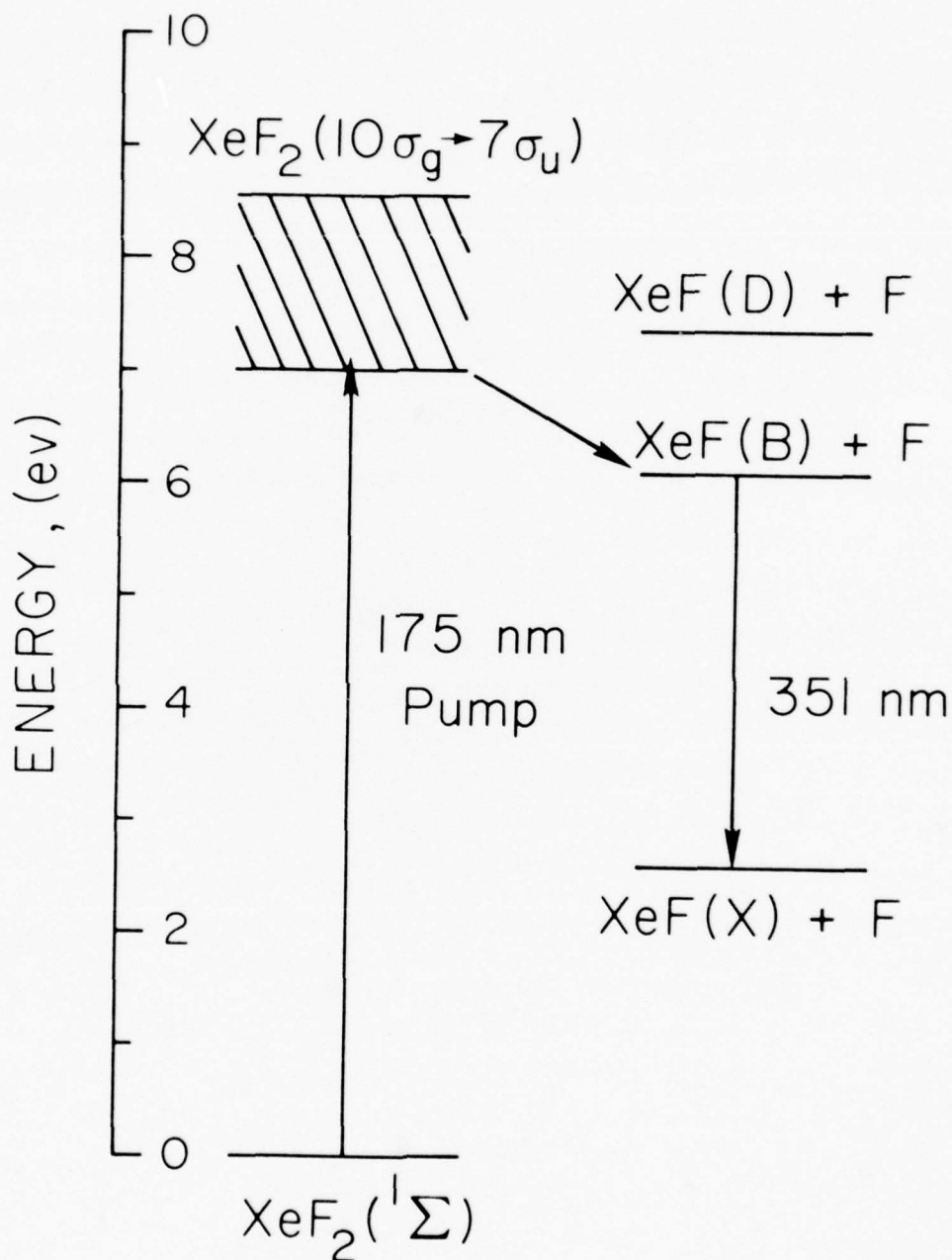
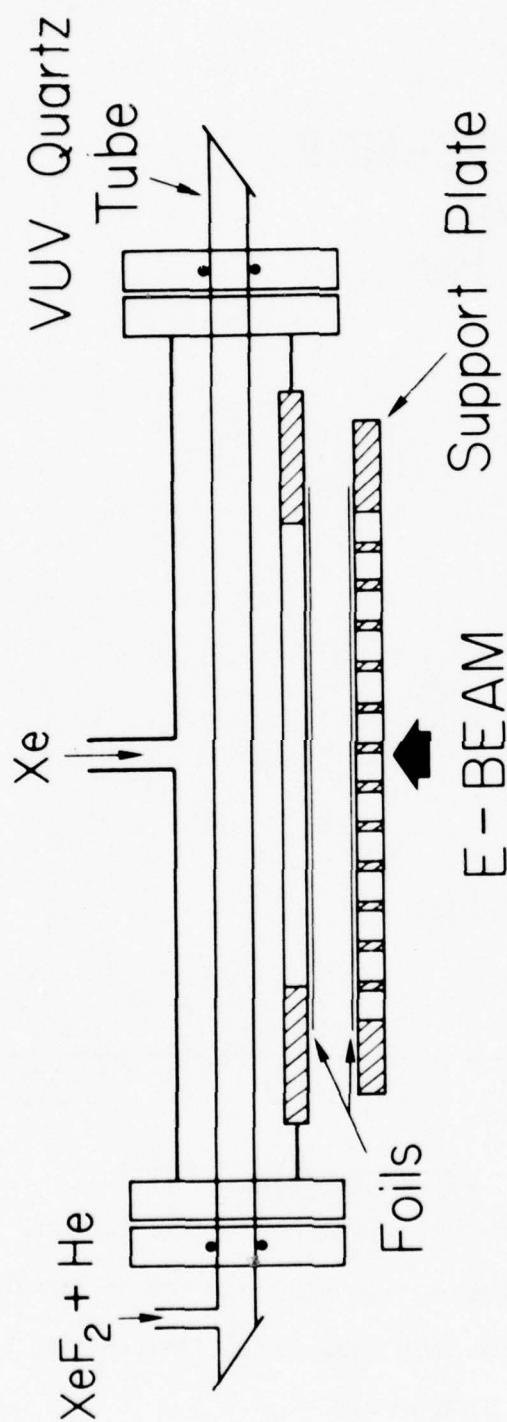


Fig. 1. Partial energy level diagram for XeF₂ and XeF showing the VUV photodissociation of XeF₂ into XeF(B) + F.

EXPERIMENTAL APPARATUS



1 cm

Fig. 2. Schematic diagram of the photolytic laser apparatus. The gap between the support plate, foils and laser cell have been expanded for clarity.

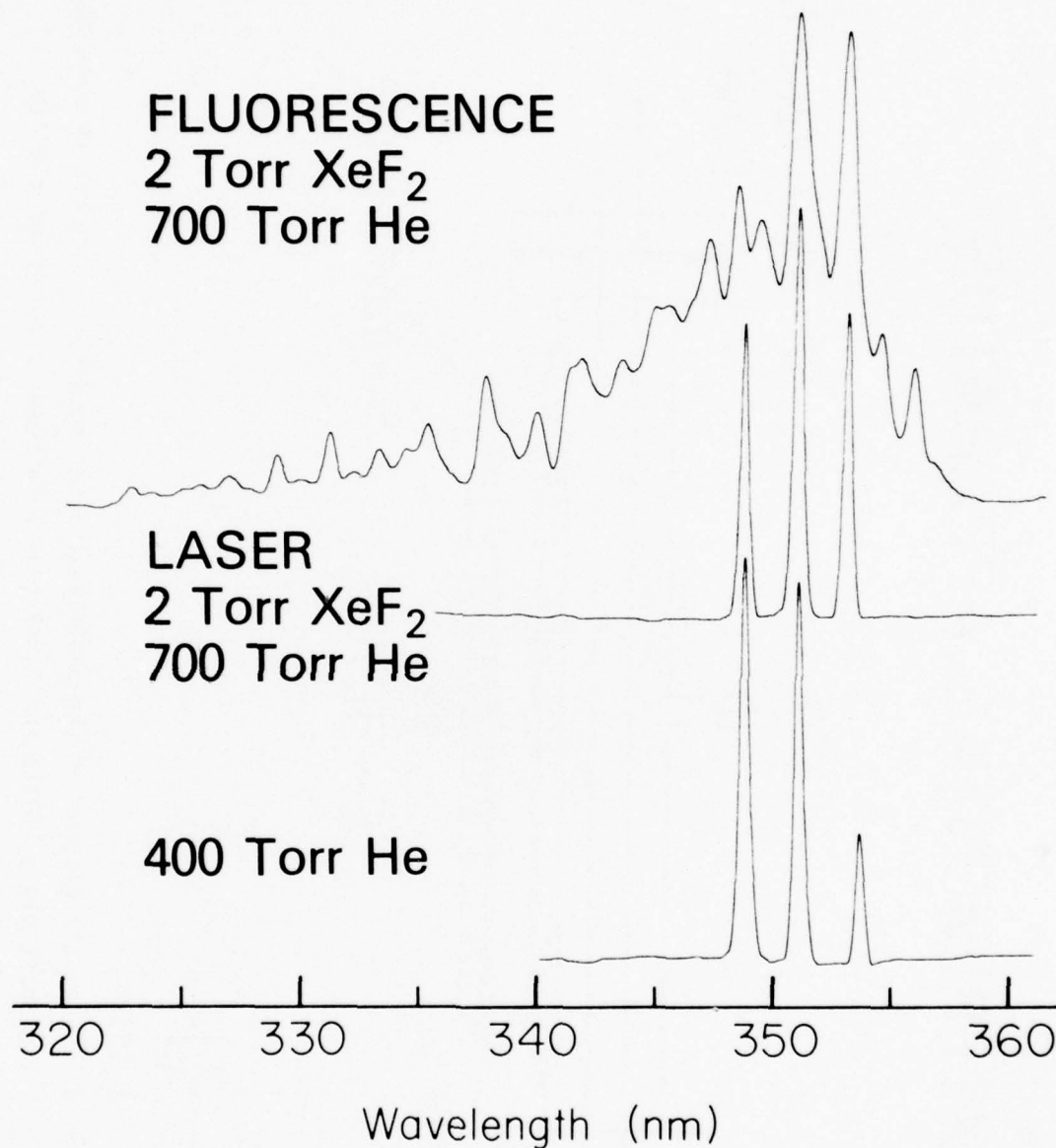


Fig. 3. Spontaneous emission and laser spectra for XeF₂ photodissociated by Xe₂^{*} fluorescence. By adjusting the He background pressure (from 400 to 700 Torr shown here) limited line tunability of the laser can be achieved.

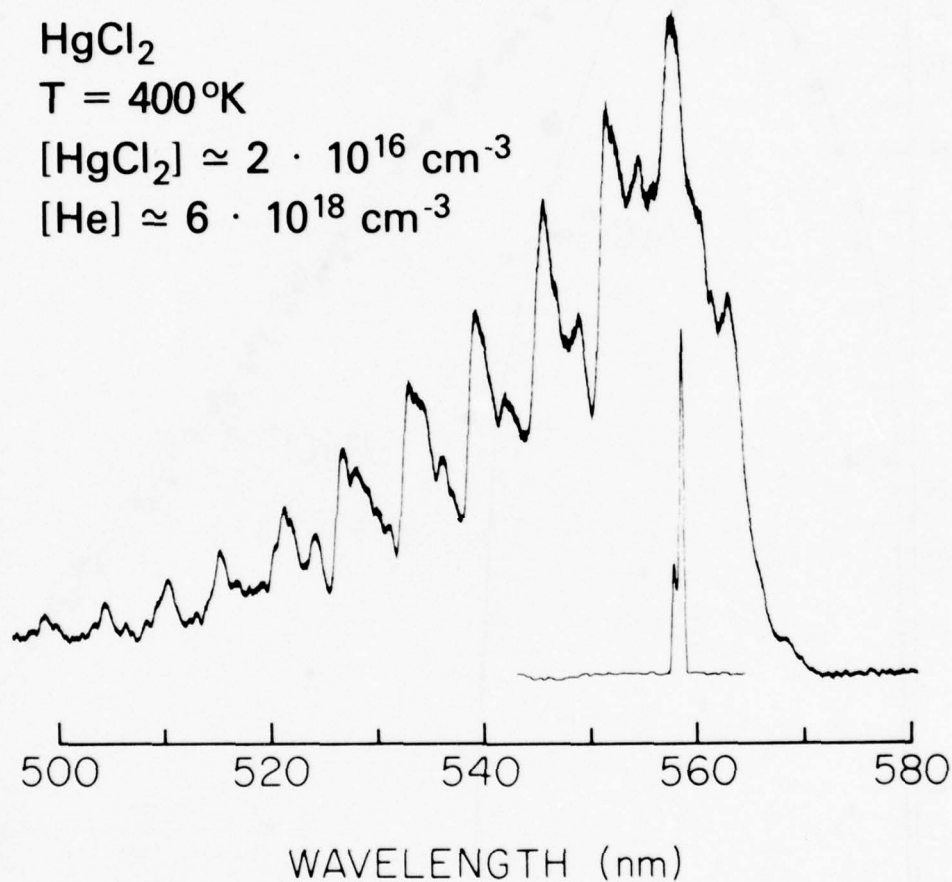


Fig. 4. Spontaneous and laser emission spectra for the HgCl^* molecule again photolyzed by Xe_2^* emission. The dominant laser line is the $v' = 1 \rightarrow v'' = 23$ transition of the $B \rightarrow X$ band at 558.4 nm.

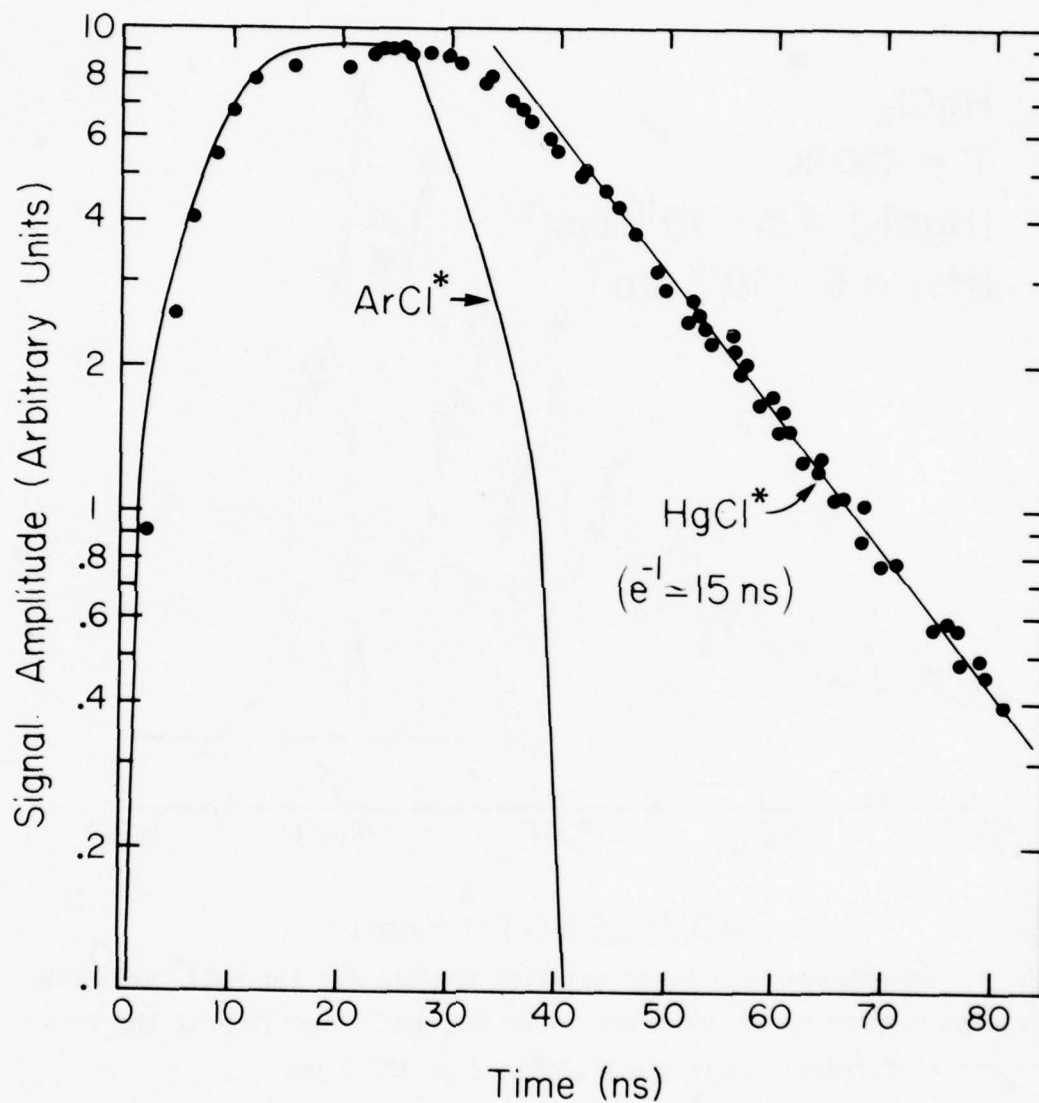


Fig. 5. Temporal dependence of ArCl^* (175 nm) and HgCl^* (558 nm) fluorescence waveforms. The exponential decay of the HgCl^* trace can be used to determine the HgCl^* radiative lifetime.

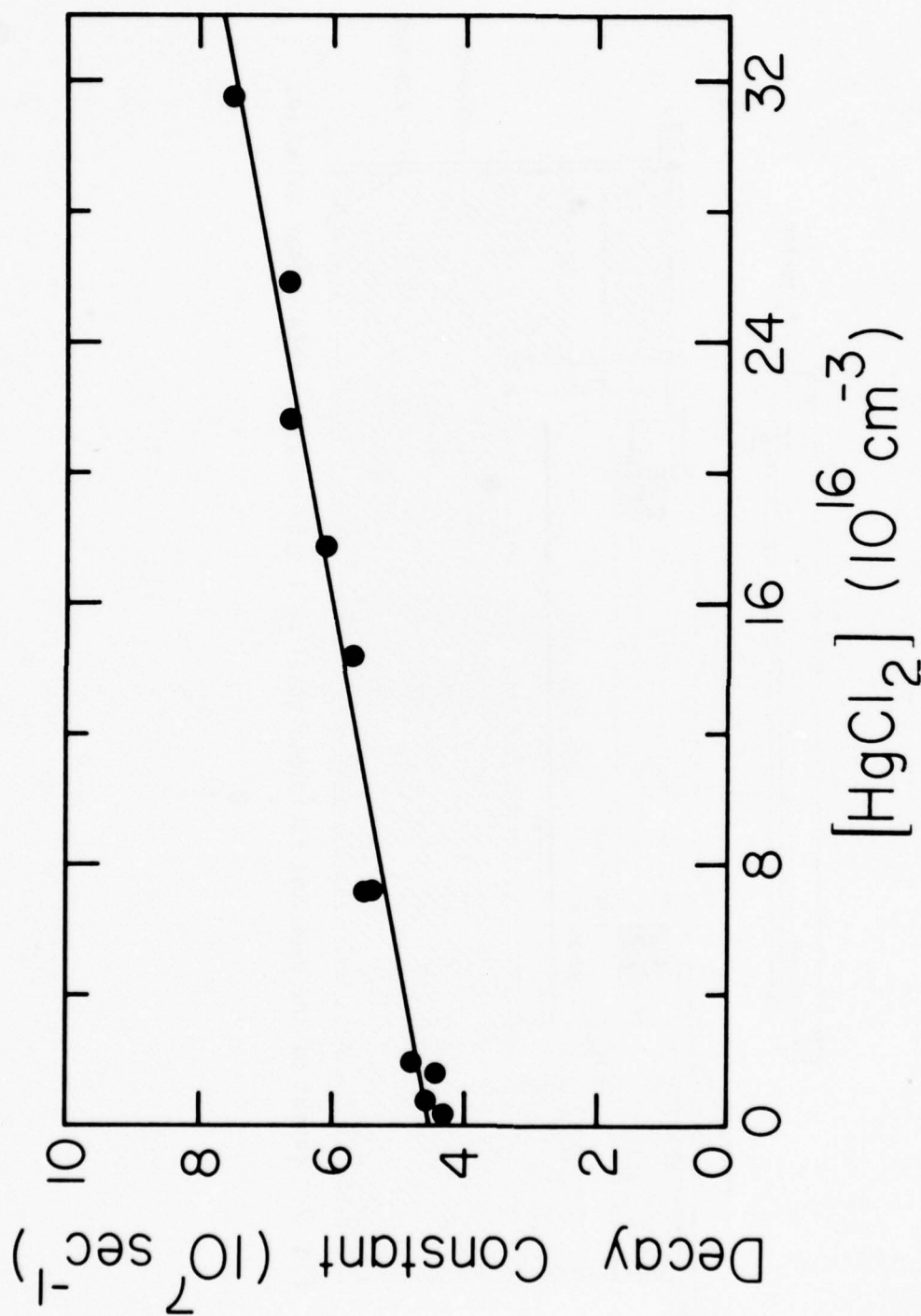


Fig. 6. Dependence of the exponential decay constant (for the HgCl^* fluorescence) on HgCl_2 concentration. The zero density intercept gives the HgCl^* radiative lifetime as 22.2 ns.

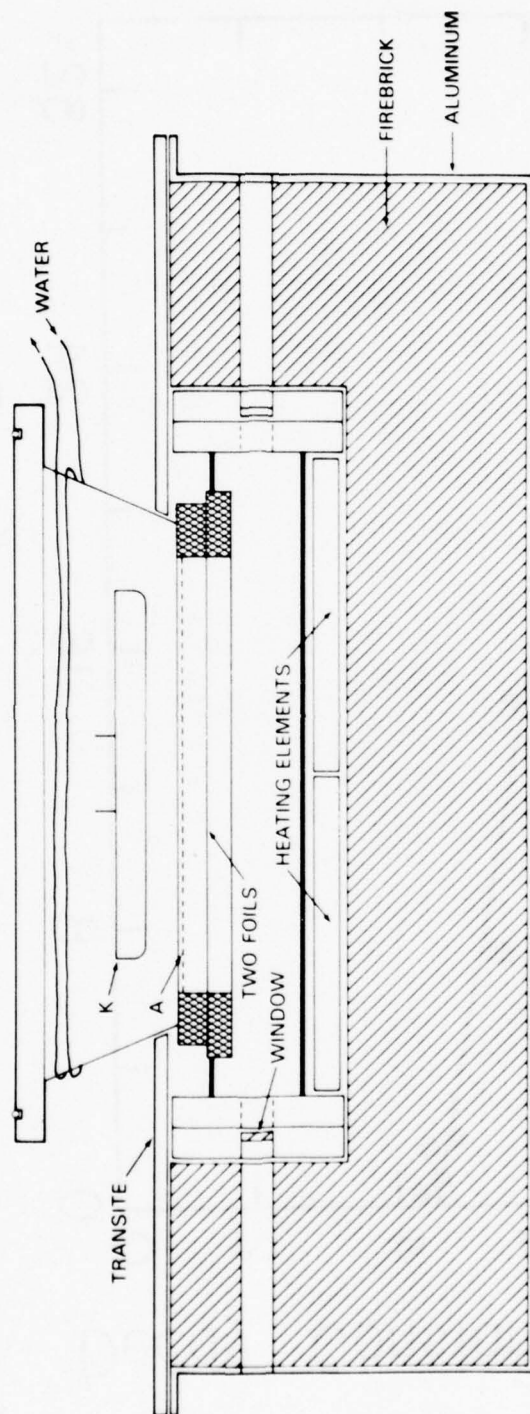


Fig. 7. Layout of the oven and stainless-steel cell used to study metal vapor molecules

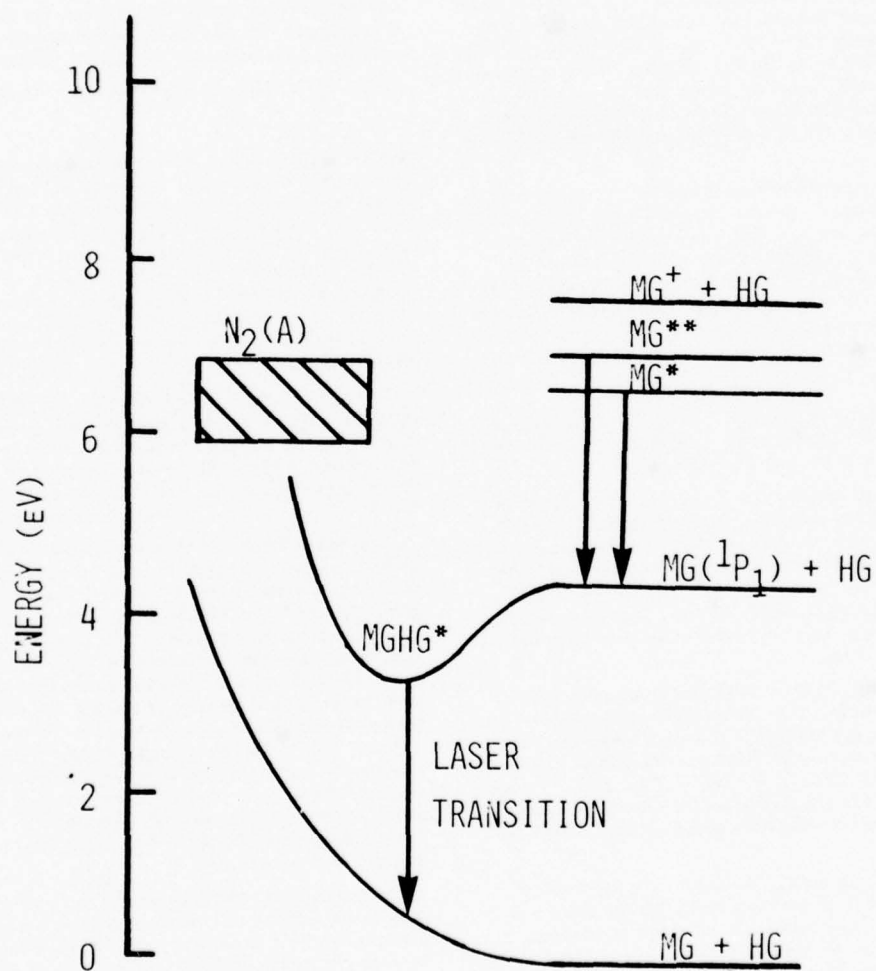


Fig. 8. Partial energy level diagram for magnesium showing the possibility of $\text{N}_2(\text{A}) \rightarrow \text{Mg}^*$ energy transfer and formation of the dissociative MgHg^* molecule.

vuv-pumped HgCl laser^{a)}

J. Gary Eden

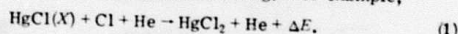
Naval Research Laboratory, Washington, D.C. 20375
(Received 9 June 1978; accepted for publication 5 July 1978)

Photolytic pumping of the $\text{HgCl}^{15}(B \rightarrow X)$ laser has been demonstrated. Oscillation at 557.6 and 558.4 nm was obtained by irradiating HgCl_2 vapor and helium with incoherent Xe^* , emission at 172 nm from an e-beam-excited xenon plasma. Also, by photodissociating HgCl_2 with ArCl^* (175 nm) fluorescence, the $\text{HgCl}(B)$ state radiative lifetime was determined to be 22.2 ± 1.5 ns.

PACS numbers: 42.55.Hg, 31.50.+w

Since the initial demonstration of lasing from HgCl and HgBr utilizing electron-beam pumping,^{1,2} a surge of activity on the mercury-halide laser family has produced stimulated emission from HgCl and HgBr with e-beam-sustained^{3,4} and uv preionized discharge excitation⁵ of rare-gas/ Hg/Cl_2 , CCl_2Br , or Br_2 mixtures. Unfortunately, chemical reaction of the mercury and halogen donor in these systems has forced the use of flowing gas mixtures⁴ or fresh gas fills for each laser pulse.³

Recently, several investigators^{6,7} have successfully induced lasing on the $B \rightarrow X$ band of HgX ($X = \text{Cl}, \text{Br}, \text{or I}$) by dissociating the salt HgX_2 by electron impact. One of the attractive features of these dissociation lasers over the $\text{Hg}/\text{halogen}$ donor chemical laser has been pointed out by Schimitschek and Celto⁶ who noted that the salt molecules appear to be recycled following dissociation and subsequent lasing. For example,



This process has presumably enabled these devices to operate for long periods of time without any noticeable degradation of the output power/pulse.

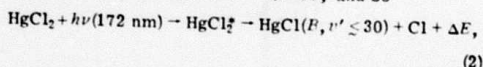
Stimulated emission on the (0, 22) and (1, 23) lines of the $B \rightarrow X$ band of HgCl^{15} , by photodissociating HgCl_2 with the vacuum ultraviolet (vuv) spontaneous emission from the Xe^* excimer, has been observed and is described in this paper. Also, from pulsed photolysis experiments using ArCl^* (175 nm) fluorescence, the $\text{HgCl}(F)$ state radiative lifetime has been measured to be 22.2 ± 1.5 ns.

Previously, HgBr and HgI photodissociative lasers have been reported⁸ where an ArF discharge laser was used for the optical pump. However, since the wavelength threshold for photolytic production of $\text{HgCl}(B)$ molecules from HgCl_2 is ~ 188 nm,⁹ an optically pumped HgCl laser has not been previously developed due partially to experimental difficulties associated with the vuv.

Wieland¹⁰ has studied the absorption spectrum of HgCl_2 in the ultraviolet and found it to be dominated by two continua with maxima lying at 181 and 185 nm. Subsequent to absorbing a photon at one of these wavelengths, a HgCl_2 molecule is dissociatively excited and the products are a Cl atom and a HgCl molecule in a low-lying vibrational level of its lowest excited electronic state B .

^{a)}Work supported in part by DARPA and ONR.

For the laser experiments described below, vacuum ultraviolet fluorescence from the Xe^* excimer was used to photolyze HgCl_2 . In this case, the excess energy above that required to photolytically produce a $\text{HgCl}(B)$ state molecule is ~ 0.6 eV, and so



where (1) the F state vibrational constants given by Wieland¹⁰ have been used to compute the highest vibrational level accessible by Xe^* photolysis and (2) $0 \leq \Delta E \leq 0.6$ eV. Although the HgCl^*_2 triatomic species is a precursor to $\text{HgCl}(F)$ formation, comparisons between the Xe^* pump and $\text{HgCl}(F \rightarrow X)$ fluorescence waveforms lead to the conclusion that the HgCl^*_2 lifetime is ≤ 1 ns. This is, as noted by Maya,¹¹ significantly shorter than the ~ 10 -ns lifetime for HgBr^*_2 calculated from uv absorption data.

The high fluorescence efficiencies projected for the rare-gas dimers¹² ($\sim 50\%$) make these excimers attractive sources of intense vuv radiation for optical pumping of a variety of molecular lasers. Recently,¹³ Xe^* was shown to be suitable for inverting various transitions of the $\text{XeF}(B \rightarrow X)$ band by photodissociating XeF_2 .

To produce the xenon excimer fluorescence used in these experiments, ~ 5000 Torr of Xe was transversely excited by a high-current ($\sim 1 \text{ kA cm}^{-2}$) beam of 450-keV electrons in a 50-ns FWHM pulse. A Suprasil quartz tube (transmission $> 85\%$ at 172 nm for a 1-mm wall thickness) containing HgCl_2 and 200 Torr He was positioned along the axis of the cylindrical xenon cell to provide for coaxial coupling of the Xe^* vuv radiation to the HgCl_2 vapor. The excitation length of the cell was ~ 15 cm. Two metal foils, one 37.5- μm -thick titanium and the other 37.5- μm -thick Inconel, were used to separate the electron-beam gun from the high-pressure xenon region. A more detailed description of the electron-beam generator and the xenon photolytic cell can be found in a recent paper.¹³

The quartz laser cell (which included Suprasil windows fused onto the cell ends at Brewster's angle) was baked out under a vacuum of $\sim 10^{-5}$ Torr and sealed after several milligrams of HgCl_2 and 200 Torr of He were admitted to the cell. For the laser experiments, the optical cavity consisted of two dielectric-coated spherical mirrors of 5-m radius of curvature separated by ~ 30 cm. One was a high reflector ($\sim 99.5\%$ at 557 nm) and the transmission of the output coupler was measured to be 4% . Laser and fluorescence spectra were

recorded by a 1.0-m Czerny-Turner spectrograph and positive-negative film. A photodiode with a S-5 photocathode response and a green bandpass filter ($T_{\text{max}} = 75\%$ at $\lambda_0 = 535$ nm; $\Delta\lambda = 90$ nm) monitored the $\text{HgCl}(B \rightarrow X)$ emission propagating along the axis of the laser cell. In addition, the temporal dependence of the Xe_2^+ vuv fluorescence was studied by mounting a sapphire window on the xenon cell and viewing the spontaneous emission with a bandpass filter ($T_{\text{max}} = 18\%$ at $\lambda_0 = 172$ nm; $\Delta\lambda = 20$ nm) and a solar blind photodiode. The temperature of the laser cell was measured by Chromel-Alumel thermocouples and the HgCl_2 particle density was determined from the vapor-pressure equation.¹⁴

Investigations of the spectrum emitted by 172-nm photolyzed HgCl_2 reveal that only the $\text{HgCl}(B \rightarrow X)$ band (shown in Fig. 1) is produced. Although peak fluorescence occurs around 557 nm, significant emission can be seen out to 500 nm which is consistent with the exothermicity of Eq. (2). Stimulated emission occurs on both the (1,23) and (0,22) lines of the $B \rightarrow X$ band of HgCl^{35} at 558.4 and 557.6 nm, respectively. Strongest lasing is observed on the $v' = 1 \rightarrow v'' = 23$ transition which contrasts with the e-beam-pumped HgCl laser.^{1,2} The inset of Fig. 1 shows the laser spectrum under higher resolution (0.1 nm). Although the resolution is insufficient to resolve individual rotational lines, some structure due to groups of high rotational levels ($J \sim 50$) of the HgCl^{35} ($B, v' = 0$ and 1) states¹⁵ is evident.

The spontaneous and laser emission waveforms are given in Fig. 2 where the arrows denote the "on" and "off" points for the e-beam current pulse. Both the fluorescence and laser signals closely follow the Xe_2^+ emission waveform (not shown). Therefore, the fact that these signals peak ~ 10 ns after termination of the e-beam current is due to cooling of the electrons in the Xe plasma, enhancing dissociative recombination (of Xe_2^+ ions) which ultimately leads to Xe_2^+ formation.

With the 4% output coupler mentioned earlier, a laser output of several μJ in a ~ 50 -ns FWHM pulse was ob-

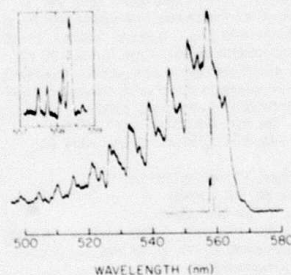


FIG. 1. Densitometer tracings of the $\text{HgCl}(B \rightarrow X)$ fluorescence (top trace) and laser emission spectra produced by the photodissociation of HgCl_2 by Xe_2^+ (172 nm) emission. The spectrograph resolution of ~ 0.4 nm is insufficient to clearly resolve the two laser lines at 557.6 and 558.4 nm. The inset shows the laser spectrum obtained with spectrograph resolution of 0.1 nm. For these spectra, $T \sim 400^\circ\text{K}$, $[\text{HgCl}_2] \sim 1.6 \times 10^{16} \text{ cm}^{-3}$ and $[\text{He}] \sim 6 \times 10^{18} \text{ cm}^{-3}$; xenon pressure in the photolytic cell was 5000 Torr.

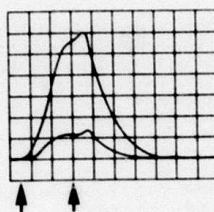


FIG. 2. Typical spontaneous (top) and laser emission waveforms. The two arrows denote the beginning and termination of the electron-beam current pulse. The cell temperature and, hence, $[\text{HgCl}_2]$ are the same as for Fig. 1 and $P_{\text{Xe}} = 5000$ Torr. The fluorescence trace closely follows the Xe_2^+ pump pulse (not shown). Horizontal scale: 20 ns/division; vertical units arbitrary.

tained. Although the resonator was probably over-coupled for the experiments, other mirrors were not available. More uniform pumping of the xenon by utilizing a coaxial e-beam diode would likely increase the system's efficiency. Also, although HgBr_2 and HgI_2 absorption spectra in the uv are known,¹¹ few data appear to be available for HgCl_2 but would, along with $\text{HgCl}(E)$ quantum yields versus wavelength, be valuable in designing a HgCl laser cell of the proper diameter. Scaling of the laser cell's diameter is especially important since it was found that the HgCl photolytic laser produced maximum output power at cell temperatures of $T \approx 400^\circ\text{K}$ ($[\text{HgCl}_2] \approx 1.6 \times 10^{16} \text{ cm}^{-3}$) and sharply diminished for elevated temperatures. Since this observation indicates that HgCl_2 strongly quenches the $\text{HgCl}(B)$ state, increasing the diameter of the laser tube is the simplest way of absorbing more pump radiation. Extraction of the power stored in the various $\text{HgCl}(F)$ state vibrational levels would be improved by using higher He pressures in the laser cell. Presumably, the helium pressure could also be used to control the dominant laser line as was possible with the XeF photodissociation laser.¹³ Finally, repetitive pulsing of the laser showed no observable decrease in the output power and no unusual deposits on the laser tube walls. These observations are consistent with Eq. (1) and the results reported by Schimitschek and Celto⁶ and Burnham.⁷

To determine the radiative lifetime of the $\text{HgCl}(B)$ state, several fluorescence measurements using ArCl^* (175 nm) spontaneous emission to photoexcite the HgCl_2 were made. Knowledge of the radiative lifetime

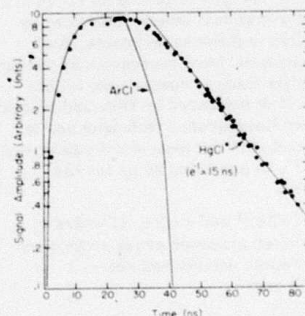


FIG. 3. ArCl^* (—) and $\text{HgCl}(B \rightarrow X)$ (●) fluorescence waveforms for 2000 Torr Ar/10 Torr Cl_2 in the photolytic cell, $[\text{HgCl}_2] = 2.7 \times 10^{17} \text{ cm}^{-3}$ and $[\text{He}] = 6 \times 10^{18} \text{ cm}^{-3}$.

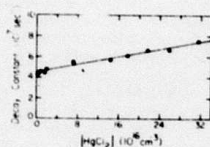


FIG. 4. Dependence of the exponential decay constant τ^{-1} on the HgCl_2 particle density. The He density was fixed at $\sim 6 \times 10^{18} \text{ cm}^{-3}$. The zero-density asymptote of the least-squares fit to the data (solid line) gives the $\text{HgCl}(B \rightarrow X)$ radiative lifetime of 22.2 ns and the slope of the line yields $k_0 = 9.2 \times 10^{-11} \text{ cm}^3 \text{ sec}^{-1}$.

is particularly useful for laser modeling studies and yet its accurate measurement depends on a pump pulse with a short decay time. For this reason, ArCl^* emission and the same experimental apparatus were used. Fluorescence from the ArCl^* excimer was obtained by e-beam excitation of 2000 Torr $\text{Ar}/10 \text{ Torr } \text{Cl}_2$ gas mixtures and has been employed previously to measure quenching rates for the $\text{XeF}(B)$ molecule.¹⁶ Typical ArCl^* and $\text{HgCl}(B \rightarrow X)$ waveforms observed for these experiments are shown in Fig. 3 for $[\text{HgCl}_2] \geq 2.6 \times 10^{17} \text{ cm}^{-3}$ and $[\text{He}] \geq 6 \times 10^{18} \text{ cm}^{-3}$. After the termination of the ArCl^* emission, the $\text{HgCl}^*(B \rightarrow X)$ signal decreased exponentially over two orders of magnitude and several time constants. Due to the rapid decay of the ArCl^* pump pulse, the destruction of $\text{HgCl}(B)$ molecules by radiation and collisions is described by the relation

$$[\text{HgCl}(B)] = [\text{HgCl}(B)]_{t=0} \exp(-t/\tau), \quad (3)$$

where $\tau^{-1} = \tau_r^{-1} + k_0[\text{HgCl}_2]$, $[\]$ indicate particle densities, τ_r is the B state lifetime, and k_0 is the rate constant for quenching of HgCl^* by HgCl_2 . Equation (3) assumes that loss of $\text{HgCl}(B)$ state molecules by two-body collisions with the He background gas is negligible.

Data analysis, then, consisted of recording $\text{HgCl}(B \rightarrow X)$ spontaneous emission waveforms on an oscilloscope for various values of $[\text{HgCl}_2]$. These traces were then digitized by computer and the falling portion of each waveform was fit to a single exponential τ .

Figure 4 shows the dependence of τ^{-1} on $[\text{HgCl}_2]$ and the least-squares fitting of the data points is represented by the solid line. The zero-density intercept of this line yields the $\text{HgCl}(B)$ radiative lifetime as 22.2 ± 1.5 ns. Since a group of vibrational levels, extending up to $v' = 22$, were excited in these experiments, the radiative lifetime measured here represents an average over those levels. This value is comparable to the HgBr lifetime of 23.2 ns measured by Djeu and Mazza¹⁷ using a laser-induced fluorescence technique and is also in good agreement with the theoretical calculations of Duzy and Hyman¹⁸ who predicted 20 ns for the $\text{HgCl}(B)$ state lifetime.

Taking $\sigma_s \tau_r$ to be $1 \times 10^{-23} \text{ cm}^2 \text{ s}$ (Ref. 1) where σ_s is the $\text{HgCl}(B)$ stimulated emission cross section and τ_r is the radiative lifetime determined above, σ_s is found to be $4.5 \times 10^{-16} \text{ cm}^2$.

The slope of the solid line gives the rate constant for quenching of HgCl_2 as $k_0 = (9.2 \pm 1.1) \times 10^{-11} \text{ cm}^3 \text{ s}^{-1}$. This rate constant and the radiative lifetime are important for improved design of HgCl electric discharge dissociation and photodissociation lasers and for determination of the $\text{HgCl}(B)$ fluorescence efficiency under various excitation conditions.

In summary, by photodissociating HgCl_2 vapor with incoherent vuv radiation, stimulated emission on the (0,22) and (1,23) lines of the $B \rightarrow X$ band of HgCl has been observed. The selectivity of the photolytic pumping mechanism and low total pressure of the laser medium suggest the desirability and feasibility of developing a closed-cycle HgCl laser with an efficiency approaching the quantum limit of 15%. In addition, the measurement of the $\text{HgCl}(B)$ radiative lifetime (22.2 ± 1.5 ns) and the rate constant for quenching of the B state by HgCl_2 will be valuable for future studies of the HgCl laser system.

The author wishes to thank D. Epp for technical assistance and R. W. Waynant for helpful discussions.

- ¹J. H. Parks, Appl. Phys. Lett. 31, 192 (1977); 31, 297 (1977).
- ²J. G. Eden, Appl. Phys. Lett. 31, 448 (1977).
- ³W. T. Whitney, Appl. Phys. Lett. 32, 239 (1978).
- ⁴K. Y. Tang, R. O. Hunter, Jr., J. Oldenettel, C. Howton, D. Huestis, D. Eckstrom, B. Perry and M. McCusker, Appl. Phys. Lett. 32, 226 (1978).
- ⁵R. Burnham (unpublished).
- ⁶E. J. Schimitschek and J. E. Celto, Opt. Lett. 2, 64 (1978).
- ⁷R. Burnham, Appl. Phys. Lett. 33, 156 (1978).
- ⁸E. J. Schimitschek, J. E. Celto, and J. A. Trias, Appl. Phys. Lett. 31, 608 (1977); *ibid* (unpublished).
- ⁹The wavelength threshold was calculated using (1) the $\text{HgCl}-\text{Cl}$ bond strength of 3.63 eV [V. I. Vedenev, L. V. Gurvich, V. N. Kondrat'yev, V. A. Medvedev, and Ye. L. Frankevich, *Bond Energies, Ionization Potentials and Electron Affinities* (Edward Arnold Ltd., London, 1966)], (2) the $\text{HgCl}(B \rightarrow X)$ photon wavelength of 557.6 nm for the (0,22) transition, and (3) the spectroscopic constants for the $\text{HgCl}(X)$ state given by G. Herzberg in *Spectra of Diatomic Molecules* (Van Nostrand Reinhold, New York, 1950).
- ¹⁰K. Wieland, Z. Phys. 76, 801 (1932); 77, 157 (1932); *Helv. Phys. Acta* 14, 420 (1941); *Helv. Chim. Acta* 24, 1285 (1941).
- ¹¹J. Maya, J. Chem. Phys. 67, 4976 (1977).
- ¹²D. C. Lorents, Physica 82, 19 (1976).
- ¹³J. G. Eden, Opt. Lett. (to be published).
- ¹⁴*Handbook of Chemistry and Physics*, edited by R. C. Weast, (Chemical Rubber, Cleveland, 1973), p. D-185.
- ¹⁵W. T. Whitney (private communication).
- ¹⁶J. G. Eden and R. W. Waynant, J. Chem. Phys. 68, 2850 (1978).
- ¹⁷N. Djeu and C. Mazza, Chem. Phys. Lett. 46, 172 (1977).
- ¹⁸C. A. Duzy and H. A. Hyman, Chem. Phys. Lett. 52, 345 (1977).

XeF($B \rightarrow X$) laser optically excited by incoherent Xe $_2^*$ (172-nm) radiation

J. Gary Eden

Laser Physics Branch, Naval Research Laboratory, Washington, D.C. 20375
Received April 4, 1978

Incoherent optical pumping of the XeF laser has been demonstrated. Stimulated emission on the $B \rightarrow X$ band of XeF at 349, 351, and 353 nm has been obtained by photolyzing XeF $_2$ with Xe $_2^*$ spontaneous emission (172 nm). Peak power of ~ 1.3 kW in a ~ 30 -nsec FWHM pulse has been observed from a high- Q resonator ($\sim 0.1\%$ transmission/mirror).

Laser oscillation on the $B \rightarrow X$ band of XeF at 350 nm has previously been demonstrated for electron beam,^{1,2} e-beam sustained,³ and discharge pumping^{4,5} of rare-gas-NF $_3$ (or F $_2$) gas mixtures. Efficiencies for this laser have been limited to $\leq 3\%$ for e-beam operation using Ne as the diluent⁶ and to 1% for excitation by a fast electric discharge.⁵ However, the ability of optical pumping to populate an electronic state of interest selectively has not previously been applied to the excitation of the rare-gas-halide lasers.

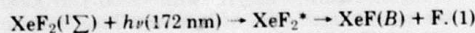
Both rare-gas-halide and rare-gas-excimer radiation have been successfully utilized as optical pumps for lasers in the near-infrared to ultraviolet region of the spectrum. Rare-gas-halide fluorescence⁷ and laser radiation^{8,9} have been used to excite the I (1.3- μ m) and In (0.451- μ m) atomic lasers and the HgBr photodissociation laser. The attractive features of the rare-gas excimers as sources of incoherent pump radiation for electronic-state lasers have been pointed out by Murray and Rhodes,¹⁰ who investigated the use of Xe $_2^*$ or Kr $_2^*$ vacuum-ultraviolet (VUV) fluorescence as excitation sources for amplifiers (operating on the auroral and transauroral lines of selenium and sulfur) for eventual use in thermonuclear fusion studies. In particular, the high fluorescence efficiencies ($\sim 50\%$) projected for the rare-gas excimers both experimentally¹¹ and theoretically¹² point to electron-beam-excited rare-gas plasmas as potentially efficient optical pumps for visible and ultraviolet lasers.

Recently, strong XeF($B \rightarrow X$) fluorescence from the pulsed photolysis of XeF $_2$ by VUV radiation was reported.¹³ In this Letter, incoherent optical pumping of the XeF laser by photodissociating XeF $_2$ with Xe $_2^*$ vacuum-ultraviolet spontaneous emission is described. Oscillation at 349, 351, and 353 nm has been observed with peak powers of ~ 1.3 kW in a 30-nsec FWHM pulse from a low-loss optical cavity.

A partial schematic diagram of the photolytic laser cell is shown in Fig. 1. An electron beam generator, consisting of an 8- Ω water-filled, coaxial Blumlein driven by a LC generator, was used to deliver a 50-nsec FWHM, 450-kV voltage pulse to a diode composed of a carbon cathode and stainless-steel-mesh anode. For a diode gap of ~ 1.5 cm, the beam current was ~ 110 kA.

After leaving the diode, the e beam penetrated two 25- μ m-thick titanium foils situated ~ 1 cm from the anode and entered a cylindrical stainless-steel cell containing high-pressure (~ 3 -7-atm) Xe gas. The two metal foils were supported by a 4-mm-thick slotted plate with 42-cm 2 of open area and a transmission of $\sim 60\%$. Roughly 50% of the electron current emerging from the diode reached the Ti foils, giving an e-beam flux of ~ 1 kA cm $^{-2}$ over the excited area. Aluminum and gold gaskets used in the past¹⁴ to seal foils to the laser cell have been discarded in favor of welding the two foils, one to the laser cell and the other to the foil support plate. In this way, vacuum integrity of the laser photolytic cell and e-beam diode could be maintained separately.

Electron-beam excitation of the xenon gas (2500-4500 Torr) produced intense Xe $_2^*$ ($O_u^+ \rightarrow$ ground) emission at 172 nm,^{15,16} which was transmitted by a 12-mm-o.d. Suprasil quartz¹⁷ laser tube containing a mixture of XeF $_2$ vapor and helium. The absorption spectrum of XeF $_2$ in the vacuum ultraviolet, which is dominated by the $10\sigma_g \rightarrow 7\sigma_u$ continuum peaked at ~ 158 nm, has been investigated by Jortner *et al.*¹⁸ Irradiation of XeF $_2$ by 172-nm emission results in the rapid, photodissociative production of XeF(B) molecules:¹³



The subsequent XeF($B \rightarrow X$) emission at 350 nm was

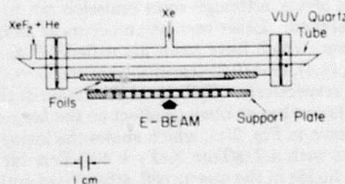


Fig. 1. Schematic diagram of the photolytic cell and quartz laser tube. The gap between the support plate and the laser cell has been expanded for clarity.

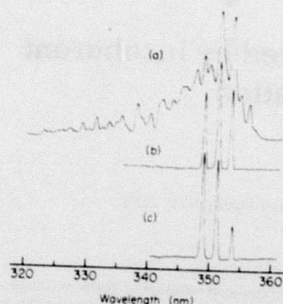


Fig. 2. Densitometer tracings of (a) $\text{XeF}(B \rightarrow X)$ fluorescence spectrum obtained with photolysis of 2.0-Torr XeF_2 -700-Torr He mixtures, (b) laser spectrum using high-reflectivity mirrors and same gas mixture as (a), (c) laser emission observed with 2.0-Torr XeF_2 and 400-Torr He mix. The Xe pressure in the outer cell for all three traces was 2500 Torr, and the spectrograph resolution was ~ 0.3 nm.

monitored along the laser cell axis by a S-5 surface photodiode or by a 1-m Czerny-Turner spectrograph (in first order) and positive-negative film. Laser and spontaneous emission spectra were obtained by scanning the film negatives with a microdensitometer. For laser-power measurements, the photodiode and neutral-density filters were calibrated against a carbon calorimeter using a 1.5-mJ-output XeF discharge laser. Two dielectric mirrors of 5-m radius of curvature, separated by ~ 30 cm, formed the stable laser resonator. The reflectivity and transmission of each mirror at 350 nm was $R > 99\%$ and $T \sim 0.1\%$, respectively.

After installation in the photolytic apparatus, the quartz laser tube (with Brewster-angle Suprasil windows at both ends) was evacuated to $< 10^{-5}$ Torr. Approximately 1 g of xenon difluoride was placed in a quartz sidearm and degassed, using dry-ice cooling and continuous pumping. The rare gases used in these experiments were of research-grade purity, and all gas handling lines were made of Teflon to prevent loss of XeF_2 through reaction with the walls.

Typical operation of the photolytic laser involved filling the stainless-steel cell with ~ 2500 -Torr Xe and the quartz laser tube with 0.5–3.0-Torr XeF_2 and 100–700-Torr He. The spontaneous and laser emission spectra of the XeF laser for 2.0-Torr XeF_2 and 700-Torr He are shown in Figs. 2(a) and 2(b). Dominant XeF^* fluorescence originates from low-lying $\text{XeF}(B)$ vibrational levels, although some emission out to ~ 330 nm is observed. Laser oscillation occurs at 349, 351, and 353 nm, which have been identified^{19,20} as $(v', v'') = (2, 5)$, $(1, 4)$, and $(0, 3)$ transitions of the $B \rightarrow X$ band of XeF , respectively. Collisional relaxation of the B -state population has an obvious effect on the laser spectrum, as shown in Fig. 2(c), which shows the lasing lines obtained with a 2.0-Torr XeF_2 + 400-Torr He mixture. With no He in the quartz cell, stimulated emission was obtained on the 349-nm line only; the other transitions appeared above ~ 50 -Torr He. Relaxation of the upper-state vibrational manifold presumably explains why the 349 transition has not been seen in e-beam-

excited XeF lasers^{2,3} and is weak in discharge-pumped systems.^{4,5}

Laser and spontaneous-emission waveforms are presented in Fig. 3. With the outer excitation cell evacuated, a small amount of $\text{XeF}(B \rightarrow X)$ emission is observed as shown in Fig. 3 (trace a). Since this fluorescence was observed only with the excitation cell evacuated, then the waveform of Fig. 3 (trace a) is likely due to XeF pumping from radiation emitted by the e beam striking the quartz cell. Also, laser emission could not be obtained under these conditions. However, with the addition of 2500-Torr Xe to the outer cell, the 350-nm fluorescence increases greatly [cf. Fig. 3 (trace b)], and, though delayed in time with respect to the start of the e-beam current, the XeF emission closely follows the Xe_2^+ pump pulse (not shown).

As shown in Fig. 3 (trace c), the laser emission follows the fluorescence after a delay of ~ 25 nsec. Measurements of the peak laser power as a function of XeF_2 and He partial pressures in the gas mixture are shown in Figs. 4 and 5. The steep rise of laser power in Fig. 4 is due to the increasing optical thickness of the photolytic medium, and the inflection in the curve at 2-Torr XeF_2 reflects the large rate constant for quenching of $\text{XeF}(B)$ by XeF_2 , recently measured¹³ as $2.6 \times 10^{-10} \text{ cm}^3 \text{ sec}^{-1}$. In contrast, helium is known to quench the exciplex at

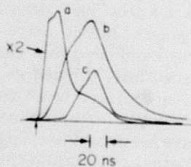


Fig. 3. Fluorescence and laser emission waveforms: (a) fluorescence obtained from 2.0-Torr XeF_2 -700-Torr He mixtures in the laser tube, outer cell evacuated; (b) spontaneous emission from the same gas mixture as (a) but 2500-Torr Xe in the outer cell, and (c) laser waveform using 2.0-Torr XeF_2 -700-Torr He gas mixture, and 2500-Torr Xe in the photolytic cell. Signal (a) is shown doubled for comparison with (b); vertical scale: arbitrary units. The arrow on the baseline denotes the start of the e-beam current.

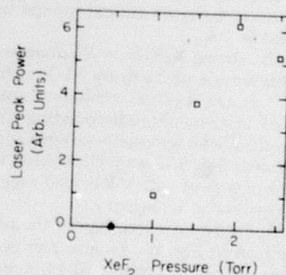


Fig. 4. Variation of photolytic laser peak power with XeF_2 partial pressure. The He pressure in the laser tube and the Xe pressure in the outer cell are both fixed at 700 and 2500 Torr, respectively.

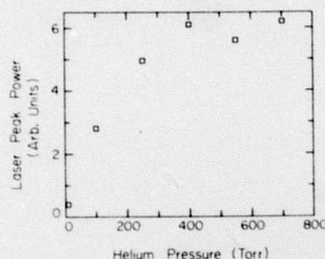


Fig. 5. Dependence of peak power on He pressure for a fixed XeF_2 partial pressure of 2.0 Torr. The Xe pressure in the photolytic cell is again 2500 Torr.

a relatively slow rate ($4 \times 10^{-13} \text{ cm}^3 \text{ sec}^{-1}$) (Ref. 13); thus the rare gas serves only to equilibrate the XeF^* vibrational manifold, which occurs around 400 Torr (Fig. 5).

The maximum laser power realized in these experiments from a high- Q optical cavity (mirror transmission $\sim 0.1\%$) is $\sim 1.3 \text{ kW}$ in a $\sim 30\text{-nsec}$ FWHM pulse, for an integrated energy of $\sim 0.04 \text{ mJ}$. Axial spectra of the lasing medium confirm that power extraction in these experiments is poor since significant fluorescence from high-lying XeF vibrational levels is observed during lasing (i.e., manifold relaxation time is long compared with the laser pulse). Therefore, higher He buffer pressures and greater output-mirror coupling will be required to exploit the efficiency of this laser fully.

Further improvement in the performance of this device could also be expected if the pumping of the xenon photolytic medium were more uniform. Transverse pumping as used in the experiments described here is certainly not optimal. Using a MgF_2 -overcoated aluminum reflector in the photolytic cell or pumping the rare gas with a coaxial e beam would likely improve the system's efficiency considerably. Finally, for 2 Torr of XeF_2 , the $1/e$ absorption depth at 172 nm is $\sim 5 \text{ cm}$.¹⁸ Therefore, laser cells of $\sim 10\text{-cm}$ diameter could be constructed to realize high output power.

The quantum efficiency of the XeF photodissociation laser using the experimental approach described above is:

$$\eta_{\text{max}} \approx 1/2 [h\nu(351 \text{ nm})/h\nu(172 \text{ nm})] \approx 24\%, \quad (2)$$

where the fluorescence efficiency of e-beam-excited xenon is taken to be 50% and the quantum yield for production of the $\text{XeF}(B)$ state (when XeF_2 absorbs a 172-nm photon) is assumed to be unity.²¹ Of course, the efficiency of coupling of the vacuum-ultraviolet radiation to the XeF_2 vapor will limit the maximum efficiency attainable for this system.

The photolytic XeF laser has several advantages over conventional-discharge or e-beam-pumped systems. The low-pressure ($\leq 1\text{-atm}$) laser medium avoids the index-of-refraction gradients in the lasing volume [experienced in high-pressure (2–5-atm) XeF lasers] that deteriorate beam quality. Also, pumping is selective and clean—the pumping process does not create opti-

cally absorbing fragments, as is the case with NF_3 in e-beam-pumped rare-gas-fluoride lasers.²² Since the laser fuel is a solid, the design of a more-compact laser becomes feasible. In fact, at the time of this writing, it was learned that Basov and co-workers have recently and independently pumped XeF using vacuum-ultraviolet radiation from an open discharge in XeF_2 , N_2 , and Ar gas mixtures.²³

In conclusion, incoherent optical pumping of the XeF laser has been demonstrated. Stimulated emission at 349, 351, and 353 nm was obtained by photolyzing XeF_2 with Xe_2^* 172-nm spontaneous emission.

The author is indebted to D. Epp and C. Mullins for constructing the laser cell and R. W. Waynant for many helpful discussions. This research was supported in part by the Defense Advanced Research Projects Agency.

References

1. C. A. Brau and J. J. Ewing, *Appl. Phys. Lett.* **27**, 435 (1975).
2. E. R. Ault, R. S. Bradford, Jr., and M. L. Bhaumik, *Appl. Phys. Lett.* **27**, 413 (1975).
3. J. A. Mangano, J. H. Jacob, and J. B. Dodge, *Appl. Phys. Lett.* **29**, 426 (1976).
4. R. Burnham, N. W. Harris, and N. Djeu, *Appl. Phys. Lett.* **28**, 86 (1976).
5. R. Burnham, F. X. Powell, and N. Djeu, *Appl. Phys. Lett.* **29**, 30 (1976).
6. L. F. Champagne and N. W. Harris, *Appl. Phys. Lett.* **31**, 513 (1977).
7. J. C. Swingle, C. E. Turner, Jr., J. R. Murray, E. V. George, and W. F. Krupke, *Appl. Phys. Lett.* **28**, 387 (1976).
8. R. Burnham, *Appl. Phys. Lett.* **30**, 132 (1977).
9. E. J. Schimitschek, J. E. Celto, and J. A. Trias, *Appl. Phys. Lett.* **31**, 608 (1977).
10. J. R. Murray and C. K. Rhodes, *J. Appl. Phys.* **45**, 5041 (1976).
11. E. E. Huber, Jr., D. A. Emmons, and R. M. Lerner, *Opt. Commun.* **11**, 155 (1974).
12. D. C. Lorents, *Physica* **82C**, 19 (1976).
13. J. G. Eden and R. W. Waynant, *Opt. Lett.* **2**, 13 (1978); *J. Chem. Phys.* **68**, 2850 (1978), and references therein.
14. J. G. Eden, *Appl. Phys. Lett.* **31**, 448 (1977).
15. J. W. Keto, R. E. Gleason, Jr., and G. K. Walters, *Phys. Rev. Lett.* **33**, 1365 (1974).
16. J. B. Gerardo and A. W. Johnson, *IEEE J. Quantum Electron.* **QE-9**, 748 (1973).
17. Heraeus-Amersil, Inc., Sayreville, N.J. 08872; the wall thickness of the laser cell tube was $\sim 1 \text{ mm}$.
18. J. Jortner, E. G. Wilson, and S. A. Rice, in *Noble Gas Compounds*, H. H. Hyman, ed. (U. of Chicago Press, Chicago, 1963), p. 358.
19. J. Tellinghuisen, G. C. Tisone, J. M. Hoffman, and A. K. Hays, *J. Chem. Phys.* **64**, 4796 (1976).
20. A. L. Smith and P. C. Koblinsky, *J. Mol. Spectrosc.* **69**, 1 (1978).
21. H. C. Brashears, Jr., D. W. Setser, and D. DesMarteau, *Chem. Phys. Lett.* **48**, 84 (1977).
22. G. N. Makeev, V. F. Sinyanskii, and B. M. Smirnov, *Dokl. Akad. Nauk SSSR* **222**, 151 (1975).
23. N. G. Basov, V. S. Zuev, L. D. Mikheev, D. B. Stavrovsky, and V. I. Yalovoy, *Kvantovaya Elektron.* **4**, 2453 (1977).

THE POSSIBILITY OF A RgOH^* LASER

Introduction

Unstable chemical species have often been observed for the first time in matrices at cryogenic temperatures. An example is XeF which was detected by means of electron spin resonance in a single crystal of XeF_4 irradiated at 77°K .⁽¹⁾ More than one decade later the fluorescence of excited XeF and similar compounds was reported in the gas phase.⁽²⁻³⁾ Shortly after the fluorescence data was reported, laser emission on excited XeF and similar compounds was published.⁽⁴⁻⁵⁾ Recently, excited rare gas hydroxides (RgOH^*) were reported for the first time.⁽⁶⁾ These species were observed in emission at 4.2°K in a matrix. In this paper we report an attempt to observe RgOH^* in fluorescence in the gas phase. We have also examined the possibility of a RgOH^* laser. A RgOH^* laser is of interest because the laser transition is bound-free and in the visible region of the spectrum.

Approach

Goodman and Brus⁽¹⁾ presented data on ArOH^* , KrOH^* , and XeOH^* . We selected XeOH^* for study because it emits over the range 380-500 nm where absorption by excited states is relatively unimportant.⁽⁷⁾ Two complete mechanisms for the production and decay of XeOH^* are given in Table 1. The basic idea of the two mechanisms is the efficient vuv photolysis of H_2O to yield OH(A) which combines with Xe to form XeOH^* .

This idea contrasts with recent work where xenon excited states were allowed to react with H_2O to form a more highly excited $XeOH$ species.⁽⁸⁾

In the photolysis mechanism, vuv radiation is generated by the electron beam excitation of Ar, steps 1 and 4 (see Table 1) followed by collision processes 2, 3, 5 leading to Ar_2^* . Ar_2^* emits vuv radiation, step (6), which is absorbed by H_2O , step (7), or which escapes the cell, step (8). Steps 7-8 were evaluated assuming an optical path length of 1.0 cm which is representative of the shortest dimension of our laser excitation cell. In order to obtain reasonable yields of Ar_2^* it is necessary to consider only mixtures with low concentrations of Xe and H_2O . Consequently, the $OH(A)$ from the H_2O photolysis is expected to react with Ar, step (8), as an intermediate to forming $XeOH^*$ via step 10. The $XeOH^*$ decays by step 11. Steps 12-18 represent unwanted side reactions which are to be avoided by the choice of the gas mixture.

The mechanism was evaluated by means of a computer code⁽⁹⁾ in which the initial concentrations were chosen to favor the photolysis mechanism and avoid quenching reactions. The electron beam current was chosen to be representative of the NRL gun - $500 A/cm^2$ of 500 KV electrons. Sample computer-drawn plots are given in Figs. 1 and 2. Both figures show that high concentrations ($10^{15} - 10^{16}$) of $XeOH^*$ are possible under the given experimental conditions.

We also evaluated a second experimental arrangement. In this arrangement the e-beam gun is used to pump a compartment filled with the high pressure Ar gas. The 128nm fluorescence from the excited Ar

radiates into an adjacent compartment filled with a low pressure mixture of Xe and H₂O. This arrangement eliminates some unwanted side reactions but does not utilize the fluorescent emission as efficiently. Our computer analysis of this arrangement showed no clear cut advantage between the two arrangements. The steps modelled by the computer are given in Table 1, part 2. The steps are similar to those in Table 1, part 1, except for the steps involving the radiation and absorption of the 128nm light. It was assumed that only 5.2% of the emission passed through the Xe-H₂O compartment.

Experimental

A limited number of experiments were carried out. (The results are presented in a qualitative manner. (Because measurements were not extensive.) The first set of experiments involved e-beam pumping⁽⁵⁾ of Ar-Xe-H₂O mixtures similar to those indicated in Figs. 1 and 2. Moderate levels of OH(A-X) emission were observed showing that high concentrations of OH(A) were present in the gas. Moderate OH(A-X) emission shows the presence of high OH(A) concentration because the radiative lifetime is ~1μs(10). Other researchers have reported high OH(A) concentrations resulting from e-beam excitation of Ar-H₂O mixtures.^(11,12) Emission from XeOH* at wavelengths longer than the OH(A-X) wavelength was sought but not found. Additional experiments were done with Ar-Kr-H₂O mixtures but once again OH(A-X) emission was observed without observation of KrOH* emission.

There are a number of possibilities for the non-observation of RgOH* emission. Two of these possibilities are rapid quenching of ArOH* or XeOH* by Ar or a slow formation rate of XeOH*. These

possibilities were eliminated in a second set of experiments patterned after the mechanism in Table 1, Part 2. The experiments used a cell with two adjacent compartments optically coupled by three L:F windows 1 cm wide by 4.5 cm long by 0.1 cm thick. The e-beam pumped compartment was filled with 2500-3500 torr Ar while the coaxial cell was filled with 2000 torr Xe or Kr plus 3 torr H₂O. Once again, OH(A-X) emission was observed but no RgOH^{*} emission was observed.

Conclusion

In spite of the negative experimental results, we still speculate that a RgOH^{*} laser could be made under the appropriate conditions. These conditions might be lower temperature operation where RgOH^{*} would be more stable or reduced Xe pressure in the two compartment apparatus to avoid quenching.

TABLE 1, Part 1

Mechanism and Rate Constants
for XeOH^* Formation by Direct e-beam Pumping

Step	Rate Constant	Reference
1. $\text{Ar} + \vec{e} \rightarrow \text{Ar}^+ + e + \vec{e}$	1.0E-17	a
2. $\text{Ar}^+ + 2\text{Ar} \rightarrow \text{Ar}_2^+ + \text{Ar}$	2.3E-31	b
3. $\text{Ar}_2^+ + e \rightarrow \text{Ar}^* + \text{Ar}$	1.0E-7	c
4. $\text{Ar} + \vec{e} \rightarrow \text{Ar}^* + \vec{e}$	3.05E-18	a
5. $\text{Ar}^* + 2\text{Ar} \rightarrow \text{Ar}_2^* + \text{Ar}$	6.0E-33	d
6. $\text{Ar}_2^* \rightarrow h\nu(128\text{nm}) + 2\text{Ar}$	2.0E+8	e
7. $h\nu(128\text{nm}) + \text{H}_2\text{O} \rightarrow \text{OH(A)} + \text{H}$	2.43E-7	g
8. $h\nu(128\text{nm}) \rightarrow h\nu(\text{escaped})$		f
9. $\text{OH(A)} + \text{Ar} + \text{Ar} \rightarrow \text{ArOH}^* + \text{Ar}$	1.0E-30	h
10. $\text{ArOH}^* + \text{Xe} \rightarrow \text{XeOH}^* + \text{Ar}$	1.0E-9	i
11. $\text{XeOH}^* \rightarrow h\nu(440\text{nm}) + \text{XeT OH(X)}$	1.0E+7	j
12. $\text{Ar}^* + \text{H}_2\text{O} \rightarrow \text{Ar} + \text{H}_2\text{O}$	5.0E-10	k
13. $\text{Ar}^* + \text{Xe} \rightarrow \text{Ar} + \text{Xe}^*$	1.8E-10	l
14. $\text{Ar}_2^* + \text{Xe} \rightarrow \text{Xe}^* + \text{Ar} + \text{Ar}$	3.0E-10	m
15. $\text{Ar}_2^* + \text{H}_2\text{O} \rightarrow \text{OH(A)} + \text{H} + 2\text{Ar}$	5.0E-10	n
16. $\text{OH(A)} + \text{H}_2\text{O} \rightarrow \text{OH(X)} + \text{H}_2\text{O}$	2.0E-10	o
17. $\text{ArOH}^* + \text{H}_2\text{O} \rightarrow \text{OH(X)} + \text{H}_2\text{O} + \text{Ar}$	5.0E-10	p
18. $\text{XeOH}^* + \text{H}_2\text{O} \rightarrow \text{OH(X)} + \text{H}_2\text{O} + \text{Xe}$	5.0E-10	q

TABLE 1, Part 2
 Mechanism and Rate Constants
 for XeOH^{*} Formation by Indirect e-beam Pumping

Step	Rate Constant	Reference
19. $\text{Ar} + \vec{e} \rightarrow \text{Ar}^+ + e + \vec{e}$	1.0E-17	a
20. $\text{Ar}^+ + 2\text{Ar} \rightarrow \text{Ar}_2^+ + \text{Ar}$	1.0E-31	b
21. $\text{Ar}_2^+ + e \rightarrow \text{Ar}^* + \text{Ar}$	1.0E-7	c
22. $\text{Ar} + \vec{e} \rightarrow \text{Ar}^* + e$	3.05E-18	a
23. $\text{Ar}^* + 2\text{Ar} \rightarrow \text{Ar}_2^* + \text{Ar}$	6.0E-33	d
24. $\text{Ar}_2^* \rightarrow h\nu(128\text{nm}) + 2\text{Ar}$	3.18E7	r
25. $\text{Ar}_2^* \rightarrow h(128\text{nm}, \text{Nc}) + 2\text{Ar}$	1.68E8	r
26. $h\nu(128\text{nm}) + \text{H}_2\text{O} \rightarrow \text{OH}(\text{A}) + \text{H}$	2.43E-7	f
27. $h\nu(128\text{nm}) \rightarrow h\nu(\text{escaped})$		g
28. $\text{OH}(\text{A}) + 2\text{Xe} \rightarrow \text{XeOH}^* + \text{Xe}$	1.0E-30	h
29. $\text{XeOH}^* \rightarrow h\nu(440\text{nm}) + \text{Xe} + \text{OH}(\text{X})$	1.0E7	j
30. $\text{OH}(\text{A}) + \text{H}_2\text{O} \rightarrow \text{OH}(\text{X}) + \text{H}_2\text{O}$	2.0E-10	o
31. $\text{XeOH}^* + \text{H}_2\text{O} \rightarrow \text{OH}(\text{X}) + \text{H}_2\text{O} + \text{Xe}$	5.0E-10	q

References for Table 1

- a. Effective rate constants derived from the product of the NRL current density times the energy loss rate of 400 keV electrons in Ar. Further information can be found in S. K. Searles and G. A. Hart, Appl. Phys. Lett. 25, 79 (1974).
- b. W. F. Liu and D. C. Conway, J. Chem. Phys. 62, 3070 (1975).
- c. Estimated value.
- d. J. LeCalvé and M. Bourene, J. Chem. Phys. 58, 1446 (1973).
- e. Estimated value for the transition probability. Emission spectrum available from O. Chesnovsky, B. Raz, and J. Jortner, Chem. Phys. Lett. 15, 475 (1972).
- f. Value calculated from the H₂O absorption coefficient, J. G. Calvert and J. N. Pitts, Jr., Photochemistry, Wiley & Sons, Inc., (1966) p. 200 and an assumption that the reaction products are OH(A) and H. The assumption is supported by work reported in L. J. Stief, W. A. Payne, and R. Bruce Klemm, J. Chem. Phys. 62, 4000 (1975).
- g. Computer code assumes that $h\nu(128\text{nm})$ escapes the cell if $h\nu(128\text{nm})$ is not absorbed in one centimeter.
- h. Estimated value. True value is almost certainly lower than this value.
- i. Estimated value.
- j. J. Goodman and L. E. Brus, J. Chem. Phys. 4858 (1977).
- k. Estimated value from inspection of Table II, Ref. 1.
- l. L. G. Piper, J. E. Velazco, and D. W. Setser, J. Chem Phys. 59, 3323 (1973).

- m. A. Gedanken, J. Jortner, B. Raz, and A. Szoke, J. Chem. Phys. 57, 3456 (1972).
- n. Estimated value.
- o. D. Kley and K. W. Welge, J. Chem. Phys. 49, 2870 (1968).
- p. Estimated value.
- q. Estimated value.
- r. The emission from Ar_2^* with its transition probability of 2×10^8 was divided into radiation which enters the Xe-H₂O compartment and radiation which misses the Xe-H₂O compartment.

References

1. J. R. Monton and W. E. Falconer, J. Chem. Phys. 39, 427 (1963).
2. M. F. Golde and B. H. Thrush, Chem. Phys. Lett. 29, 486 (1974).
3. J. E. Velazco and D. W. Setser, J. Chem. Phys. 62, 1990 (1975).
4. J. J. Ewing and C. H. Brau, Appl. Phys. Lett. 27, 350 (1975).
5. S. K. Searles and G. A. Hart, Appl. Phys. Lett. 27, 243 (1975).
6. J. Goodman and L. E. Brus, J. Chem. Phys. 67, 4858 (1977).
7. DARPA-NRL Laser Program Report, NRL Memorandum Report 3753 (April, 1978).
8. MHR Hutchinson, Tenth International Quantum Electronics Conference, May 29, 1978.
9. T. H. Johnson, L. J. Palumbo, and A. M. Hunter, IEEE, J. Quantum Electron. To be published Feb, 1979.
10. K. H. Becker and D. Haaks, Z Naturforsch 28a, 249 (1973).
11. R. A. Gutcheck, R. M. Hill, D. C. Lorents, D. L. Huestis, M. V. McCusker, and H. H. Nakano, J. Appl. Phys. 46, 3106 (1975).

12. C. H. Chen and M. G. Payne, Optics Commun. 18, 476 (1976).

AR/XE/H₂O = 2600/5.2/2.6 (TORR)

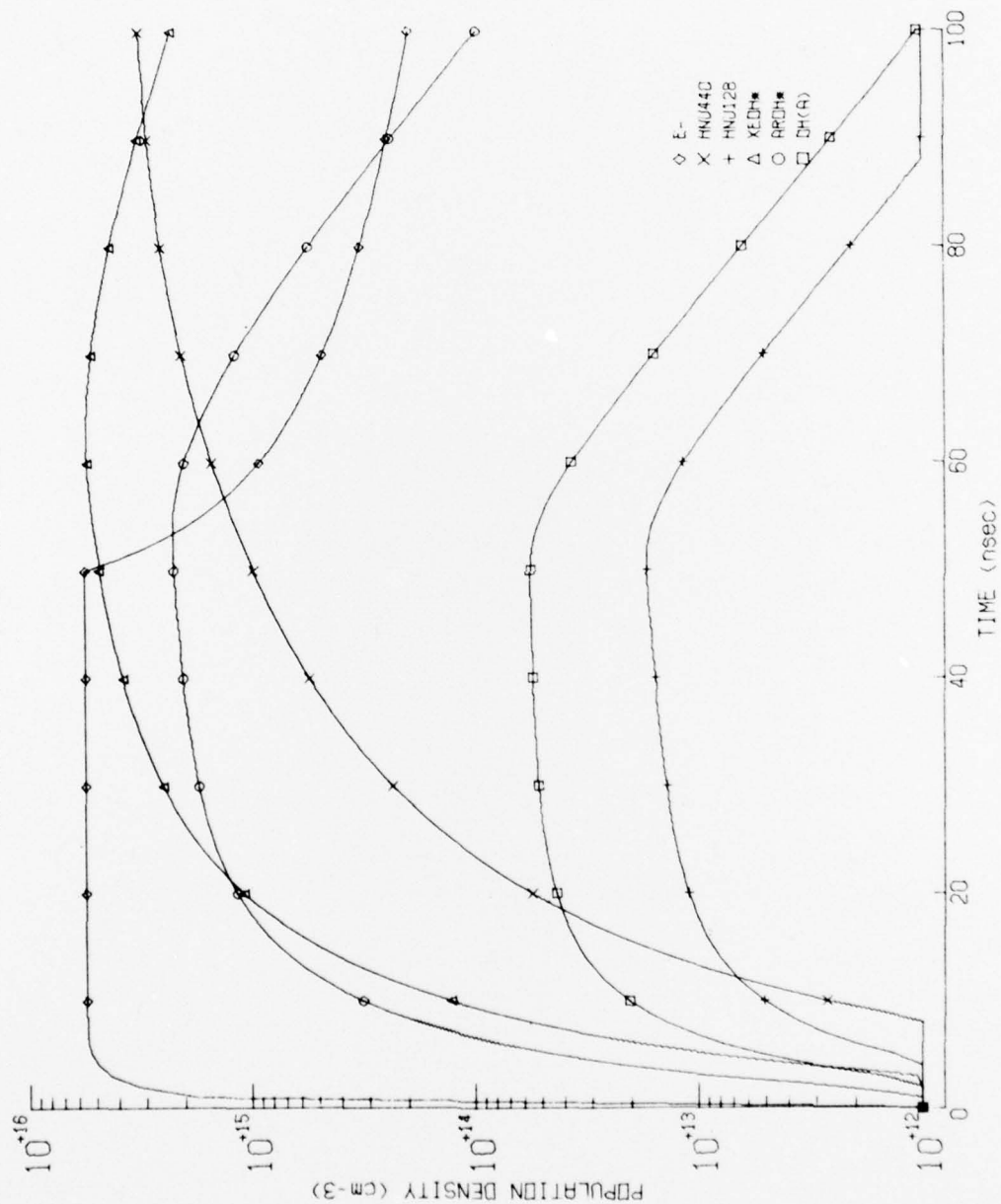


Fig. 1. Calculation of XeOH* population density in a cell with a total pressure of 2608 torr

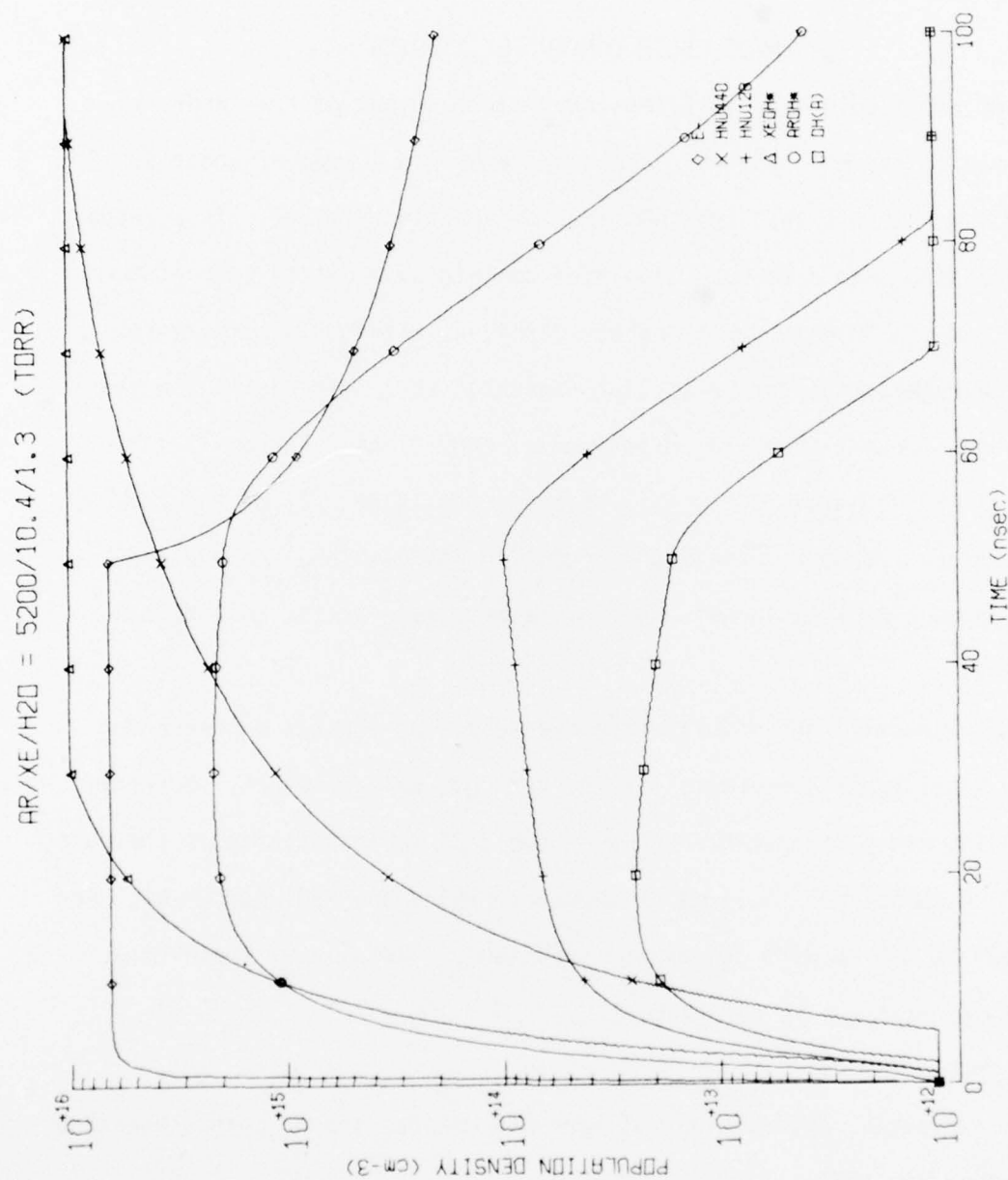


Fig. 2. Calculation of $XeOH^*$ population density in a cell with a total pressure of 5211 torr

WAVELENGTH CONVERSION STUDIES

Attempts were made to Raman convert the output of KrF laser in Ca vapor to 545 nm. The KrF laser used produced a beam of about 50 mJ in 20 nsec and was less than 10 times diffraction limited. This output was focussed into a Ca heat pipe oven containing about 10 torr of the metal vapor. No Raman emission was observed, although a three-level gain calculation performed earlier indicated that sufficient gain should have been present under the experimental conditions. The failure to observe the Raman signal is attributed to the inadequacy of the three-level model. Indeed, detailed calculations by Rescigno¹ showed that interference among a large number of intermediate states must be considered.

As a result, our efforts have been directed towards a search for other metal vapor converters for the rare gas halide lasers. Several promising media have been found when the XeCl laser was used as the pump. The most notable of these is Pb vapor, in which the XeCl output has been shifted to 485 nm with 50% energy efficiency. Details of these experiments can be found in reference 2

Reference

1. T. Rescigno, Applications of Rare Gas Halides and HF Lasers Workshop, September 19, 1978.
2. R. Burnham and N. Djeu, Optics Letters 3, 215 (1978).